UNIVERSITY OF CALIFORNIA
IRVINE

Inelastic Neutron Scattering Study of the Intermediate Valence Compounds $CePd_3$ and $YbAl_3$

DISSERTATION

submitted in partial satisfaction of the requirements for the degree of

DOCTOR OF PHILOSOPHY

in Physics

by

Victor Roberto Fanelli

Dissertation Committee:
Professor Jon M. Lawrence, Chair
Professor Alexander Chernyshev
Professor Peter Taborek

2009

The dissertation of Victor Roberto Fanelli is approved,
and is acceptable in quality and form
for publication on microfilm and in digital formats:

_____

_____

_____

Committee Chair

University of California, Irvine

2009

To Rosi,

Guadi and Agustina

Table of Contents

List of Figures

List of Tables

Acknowledgements

I would like to thank my advisor Professor Jon M. Lawrence for all his help and continuous guidance through graduate school. I really admire his enthusiasm (and accuracy) spread when discussing Physics. Thank you Jon! My very warm thanks also go to my main supervisor in Los Alamos, Marcelo Jaime, who, by the way, helped me in starting this endeavour so far away from home. He is a great mentor indeed, who introduced me to the experimental world of low temperatures and high magnetic fields.

I am proud to have been working with Andy Christianson and CuiHuan Wang. Using your words, Andy, you were my "big brother" in neutron scattering; thanks for your patience, your guidance during the experiments, and all your support in my career. CuiHuan, I learned a lot from your insight, and ability to identify the right questions. Both of you made the beam time hours a wonderful experience. I would like to acknowledge the great number of people who has also contributed scientifically to the work presented in this dissertation. Among them, my special gratitude goes to Eric Bauer, Joe D. Thompson and Ken McClellan. I am also grateful for a fruitful collaboration in the neutron scattering experiments with Eugene A. Goremychkin, Mark Lumsden, Ray Osborn and Jerel Zarestky.

Being stationed at the National High Magnetic Field Laboratory in Los Alamos, was an invaluable learning experience. I had the great opportunity to learn from virtually all the people at the lab. I am grateful for all the support given by Alex Lacerda, and for the myriad of times Julie Gallegos and Mike Pacheco gave me the right assistance. My time at the "magnet lab" could not have been better, with such cheerful "magnet partners" as Frederik Fabris Wolf, and Sonia Francoual. Sonia, thanks for the infinitely useful discussions while preparing my dissertation. Of course, this list is not complete without mentioning Izabela Stroe, Peter Sharma, Alejandro Silhanek, Oscar Ayala Valenzuela and the rest of the "gang". I would also like to thank Pinaki Sengupta and Cristian Batista for the useful theoretical discussions. In countless opportunities, Cristian made the hardest topics unbelievably clear and enjoyable. Finally, life in Los Alamos would not

have been the same without such friends as Victor Correa, Boris Maiorov, and Leo Civale, always ready to give a hand in trying times.

Very special thanks for my wife, Rosi, whose care, unconditional support and encouragement were essential in this quest. To my dear daughters Guadi and Agustina, who bring light and laughter to every one of my days. I am grateful for the enormous support from my family in Argentina, in particular from Juan, Aldo and Finita Pistono. As always in my life, I cannot forget my parents, Pina and Nino who have encouraged me in all possible ways to pursue my dreams. Among my dearest friends, Roberto Masucci helped me in facing the challenge of departing from home. I am very grateful to my country, Argentina, where I was able to study with great teachers, and classmates, a privilege only possible thanks to a free public education system.

At the University of California, Irvine, I had enjoyed the support and company of a great group of talented companions: Ben Ziemer, Eli Van Cleve and Feng Xiao, as well as great teachers as Arnoldo Guerra, and faculty as Sasha Chernyshev and David Kirkby. During my time in California, excellent friends such as Ines and Tim Collison, Wendy Collison, John and Elena Freeman who have been so close to me, Rosi, Guadi and Agustina, and made us feel “in family” from the very first day in the US.

The scientific work has been supported as follows: work at UC Irvine, by US DOE Grant No. DE-FG03-03ER46036, work at Los Alamos National Laboratory, by the Department of Energy, the State of Florida and the National Science Foundation.

Los Alamos, New Mexico Victor R. Fanelli

January 10, 2009

Curriculum Vitae

Victor Roberto Fanelli

1993	B.Sc. in Physics, Universidad Nacional de Tucumán, Argentina
1991-1996	Teaching Assistant, Department of Physics, Universidad Nacional de Tucumán, Argentina
1997	Licenciado en Física, Universidad Nacional de Tucumán, Argentina
1998-1999	Research Assistant, Centro de Investigación Industrial CINI, Techint Org., Buenos Aires, Argentina
1999	M.Sc.in Materials Science, Universidad Nacional de Gral. San Martín, Argentina
1999-2003	Teaching Assistant, Department of Physics, Universidad Nacional de Tucumán, Argentina
2004	Teaching Assistant, Department of Physics and Astronomy, University of California, Irvine
2005-2009	Graduate Student Researcher, Department of Physics and Astronomy, University of California, Irvine
2009	Ph.D. in Physics, University of California, Irvine Dissertation: Inelastic Neutron Scattering Study of the Intermediate Valence Compounds $CePd_3$ and $YbAl_3$. Professor Jon M. Lawrence, Chair

Publications

E. D. Bauer, C. Wang, V. R. Fanelli, J. M. Lawrence, E. A. Goremychkin, N. R. de Souza, F. Ronning, J. D. Thompson, A. Silhanek, V. Vildosola, A. M. Lobos, A. A. Aligia, S. Bobev, D. Garcia, and J. L. Sarrao, "*Simplifying Strong Electronic Correlations in Uranium: Localized Uranium Heavy-fermion UM_2Zn_{20} (M=Co, Rh) Compounds*". Phys. Rev. B, **78**, 115120 (2008).

V.R. Fanelli, A.D. Christianson, M. Jaime, J.D. Thompson, H.S. Suzuki, J.M. Lawrence, **"***Magnetic Order in the Induced Magnetic Moment System Pr_3In"*, Phyica B, **403**, 1368 (2008).

J.M. Lawrence, V.R. Fanelli, E.A. Goremychkin, R. Osborn, E.D. Bauer, K.J. McClellan, A.D. Christianson, *"Inelastic Neutron Scattering in $CePd_3$"*, Physica B, **403**, 783 (2008).

A.V. Silhanek, Takao Ebihara, N. Harrison, M. Jaime, Koji Tezuka, V. Fanelli, and C.D. Batista, *"Nonlocal Magnetic Field-Tuned Quantum Criticality in Cubic $CeIn_{3-x}Sn_x$ (x=0.25)"*, Phys. Rev. Lett. **96**, 206401 (2006).

A.V. Silhanek, M. Jaime, N. Harrison, V.R. Fanelli, C.D. Batista, H. Amitsuka, S. Nakatsuji, L. Balicas, K.H. Kim, Z. Fisk, J.L. Sarrao, L. Civale, and J.A. Mydosh, "*Irreversible Dynamics of the Phase Boundary in $U(Ru_{0.96}Rh_{0.04})_2Si_2$ and Implications for Ordering"*, Phys. Rev. Lett. **96**, 136403 (2006).

A.D. Christianson, V.R. Fanelli, J.M. Lawrence, E.A. Goremychkin, R. Osborn, E.D. Bauer, J.L. Sarrao, J.D. Thompson, C.D. Frost, and J.L. Zarestky, *"Localized Excitation in the Hybridization Gap in $YbAl_3$"*, Phys. Rev. Lett. **96**, 117206 (2006).

G.R. Murtagian, V.Fanelli, J.A. Villasante, D.H. Johnson, and H.A. Ernst, "*Sealability of Stationary Metal-to-Metal Seals"*, Journal of Tribology (American Society of Mechanical Engineers) **126**, 521 (2004).

Abstract of the Dissertation

Inelastic Neutron Scattering Study of the Intermediate Valence Compounds $CePd_3$ and $YbAl_3$

By

Victor Roberto Fanelli

Doctor of Philosophy in Physics

University of California, Irvine, 2009

Professor Jon M. Lawrence, Chair

$CePd_3$ and $YbAl_3$ are intermediate valence metals. These systems exhibit a renormalized Fermi liquid ground state that evolves towards a high temperature local moment regime. Much of the physics of these compounds is believed to be captured by the Anderson impurity model, however, the Periodic Anderson model is essential for understanding the coherent ground state.

The objective of this dissertation is to explore in further detail the spin dynamics of intermediate valence compounds and discuss the agreement with the predictions of these models. We have performed inelastic neutron scattering measurements on single crystals of $CePd_3$ and $YbAl_3$, in order to study the energy spectrum of the spin fluctuations and its variation over reciprocal space in both regimes. The momentum transfer (Q) dependence should reveal the coherent character of the ground state as well as the spatially localized

spin fluctuations of the high temperature limit. Since most previous neutron scattering experiments on intermediate valence compounds were done in polycrystalline samples, determination of the Q-dependence has remained open.

Our results show that the high-temperature response is Q-independent, with a Lorentzian quasielastic energy spectrum with a half width Γ = 26.6 meV for $CePd_3$ and Γ = 35 meV for $YbAl_3$. This is in agreement with the Anderson impurity model, that predicts local moment behavior in this regime.

The low temperature magnetic response has the basic Kondo-like behavior expected by the impurity model. It shows an inelastic Lorentzian spectrum, with characteristic energy E_0 = 44 meV and Γ = 32 meV for $YbAl_3$, and E_0 = 45 meV and Γ = 43.5 meV for $CePd_3$, but unlike the impurity model, it reveals some variation with momentum transfer, including intensity maxima at zone boundary Q. However, this Q-dependence is only 15 to 20 percent, much smaller than that predicted by the Anderson Lattice model. We will discuss possible reasons to explain this discrepancy.

In addition, in the case of $YbAl_3$, we confirmed the existence of a new excitation beyond the usual Kondo-like scattering in the low temperature regime at 33 meV, which appears to represent a local excitation in the hybridization gap.

Chapter 1

Introduction

The purpose of this dissertation is to contribute to the understanding of the properties of intermediate valence compounds. We have chosen to focus on the spin dynamics of these compounds and to explore this dynamics using neutron scattering techniques.

Rare earth intermediate valence compounds constitute a classic correlated-electron problem of a degree of complexity lower than that of the Heavy Fermion or high temperature superconductor compounds. It is believed that much of the physics of these compounds can be derived from the Anderson Impurity Model, however key features require going beyond this model. In general, it is accepted that the Anderson Lattice Model is the natural candidate to extend the understanding of the physics in these systems. We will analyze our results and test these models.

Properties like the magnetic susceptibility, specific heat, valence and spin dynamics are dominated by spin fluctuations, for which inelastic neutron scattering is the appropriate experimental probe. An acceptable amount of research has been done on polycrystalline samples but few experiments have been done on single crystalline samples. A complete study should involve the exploration of the spin dynamics as a function of both energy and momentum transfer over the reciprocal space, requiring

single crystalline samples of proper quality and size. Since these have been available only during the last few years, we have taken advantage of this opportunity to perform a systematic study of the spin dynamics of these compounds.

In the introductory section we briefly review relevant aspects in the field of intermediate valence compounds, in the following section we describe the basic phenomenological results. Next, we introduce an overview of the theoretical models and their results for the quantities of interest. The final section outlines the objectives and the organization of this dissertation.

1.1 General Overview

Rare earth elements have the electronic configuration of a filled xenon core, plus z bonding or valence electrons in 5d and 6s states and n electrons in the 4f orbitals, that can be represented as $(5d6s)^z\ 4f^n$. The number z of valence electrons can be 2, 3 or 4, and the number of 4f electrons ranges between 0 and 14.

When embedded in a solid environment, rare earth (RE) atoms donate bonding electrons to wide bands enhancing the binding energy of the solid, while the remaining electrons outside the xenon core are in localized 4f states. The valence state of the RE ion is usually an integer value, however, some intermetallic compounds of RE show a valence with a non-integral value.

Usually, the energy separation between two integral valence states, that is, between one with a configuration consisting of a number n of 4f electrons and z valence electrons and another with (z+1) and (n -1) respectively, is of the order of 5 to 10 eV. However, for

compounds of elements Ce, Sm, Eu, Tm and Yb, this value can be as small as 0 to 2 eV. In this case of nearly degenerate bonding states, an interaction that hybridizes the highly localized 4f electrons with the conduction bands, can make the RE ions fluctuate between the $4f^n$ and $4f^{n-1}$ configurations, where the conduction electrons are hopping on and off the rare earth sites.

The Coulomb interaction between the 4f electrons within these orbitals of relatively small radius is large, with values ranging from 5 to 10 eV. The resulting Coulomb correlation reduces the effective hybridization or hopping rate, that is, the motion in and out of the f orbital is slowed down. This rate is related via the Uncertainty Principle to a characteristic energy scale for valence/spin fluctuations (hybridization). The scattering of the conduction electrons from these slow valence fluctuations leads to a large value of effective mass. As discussed further below in section 1.3, this basic scenario – hybridization of local 4f states with conduction states in presence of strong on-site Coulomb interaction– means that the Kondo/Anderson physics is applicable, and the characteristic energy scale is then the Kondo scale $k_B T_K$.

In these compounds, the ground state is therefore a quantum mechanical admixture of the $4f^n$ and $4f^{n-1}$ configurations, giving rise to a non-integral occupation of the 4f orbitals with the same non-integral value for the valence over the different RE sites. This case is referred as a homogeneous intermediate valence (IV) system. (In inhomogeneous mixed valence compounds, RE atoms on inequivalent sites have different integral valences).

The IV compounds are part of a larger class of compounds, known as valence fluctuation compounds that include the Heavy Fermion compounds. Nevertheless, we

will restrict our study to those RE compounds that exhibit a distinctly non integral valence. These IV compounds typically have moderately enhanced effective masses and characteristic Kondo energies that are large enough that crystal field effects can be ignored. These systems display a renormalized Fermi liquid behavior and its crossover to local moment behavior, and they will give the opportunity to test the applicability of both the Anderson Impurity Model (AIM) and the orbitally degenerate isotropic Anderson Lattice Model (ALM), two of the most important ones to explore the electron correlations in solids.

1.2 Basic Phenomenological Description

Among the measured properties of IV compounds, two limiting behaviors are observed. In the high temperature limit, the RE approaches integral valence (trivalent configuration for Ce and Yb IV intermetallic compounds) with a local magnetic moment behavior. At a characteristic temperature, there is a crossover to the low temperature limit where the experimental features correspond to those of a renormalized Fermi Liquid (FL).

1.2.a Magnetic Susceptibility, Specific Heat and Valence

In this section we will explore the temperature dependence of the susceptibility, specific heat and 4f occupation number, all quantities dependent on the spin fluctuations. As examples, the experimental results for $CePd_3$ and $YbAl_3$ are presented. It is interesting to show both of these intermetallic compounds since the trivalent Yb ion with $4f^{13}$

electronic structure is the hole counterpart of the trivalent Ce ion with $4f^1$ electronic structure.

The static magnetic susceptibility χ shows a broad maximum at a temperature T_{max} between 120 K and 150 K for $YbAl_3$[1] and $CePd_3$[2], as illustrated in figure 1.1(a) and (d). At temperatures higher than T_{max}, χ shows a Curie-Weiss behavior $\chi(T)=C_J/(T+\theta_{CW})$, where θ_{CW} denotes the Curie-Weiss temperature and the Curie constant C_J is given by

$$C_J = N_{AV}\, g_J^{\,2} \mu_B^{\,2}\, J(J+1)/3k_B \qquad (1.1)$$

where N_{AV} is the Avogadro's number, g_J is the Landé g-factor, μ_B is the Bohr magneton, J is the total quantum angular momentum and k_B is the Boltzmann constant. This is the local magnetic moment regime. As the temperature is decreased below T_{max}, there is a crossover to a Pauli paramagnet behavior. This corresponds to the low temperature regime.

In the high temperature limit, the RE ion valence z is close to an integral value. For instance, in this local moment limit, Ce and Yb ions tend to a trivalent valence state with an average 4f occupation number n_f tending to unity. For Ce ions, the valence z satisfies $z = (4-n_f)$, whereas for Yb ions, where the occupation number is defined as the number of holes in the otherwise full $4f^{14}$ shell, this is $z = (2 + n_f)$. As temperature decreases, the valence fluctuation increases, leading to a non integral value z, with $n_f < 1$ ($n_f = 0.8$ for $CePd_3$ and 0.75 for $YbAl_3$). Figure 1.1 (b) and (e) illustrates the occupation number n_f, determined from the near-edge structure in Yb [1] and in Ce [3] by L_3 X-ray absorption measurements.

In a similar way to the magnetic susceptibility, the electronic contribution to the specific heat $C_m(T)$, resulting after subtraction of a lattice contribution, shows a broad

peak around a temperature of the order of T_{max}. This contribution to the specific heat is shown in figure 1.1(c), plotted as C_m/T for $YbAl_3$[1]. The value T_{max} can therefore be associated with the crossover temperature between the two regimes. In addition, a large value for the linear coefficient of specific heat γ is observed (approximately 40 mJ/mol-K^2 for $YbAl_3$ and 30 mJ/mol-K^2 for $CePd_3$[4] as shown in figure 1.1(f)), evidencing quasiparticles of enhanced effective mass m*. The integrated entropy S_m under the $C_m(T)/T$ curve (Fig. 1.1(c)) is on the order of the value for the entropy associated with spin fluctuation R ln (2J+1), where R is the universal gas constant and 2J+1 is the degeneracy (N) of a total quantum angular moment J. In the case of $YbAl_3$ (J=7/2), the value for the entropy at room temperature reaches 60% of the expected value (R ln 8) at high temperatures, as illustrated in Figure 1.1(c). From this perspective, this "may be called the spin-fluctuation contribution to the entropy by the f electrons" in words of C. M. Varma [5]. These general features shown in figure 1.1 are observed in almost all metallic IV compounds [6].

These measured properties support the picture of a Fermi Liquid ground state. Both the Pauli susceptibility and the linear coefficient of specific heat, being proportional to the density of energy states at the Fermi level, are therefore exposing a moderate enhancement of the effective mass m* that results from the correlated hybridization of the local 4f states with the conduction band. For example, the value for m* for $YbAl_3$ obtained from other experimental techniques[2,7,8], such as de Haas Van Alphen and optical conductivity measurements (section 1.2.c), is between 20 to 30 times relative to the bare band mass.

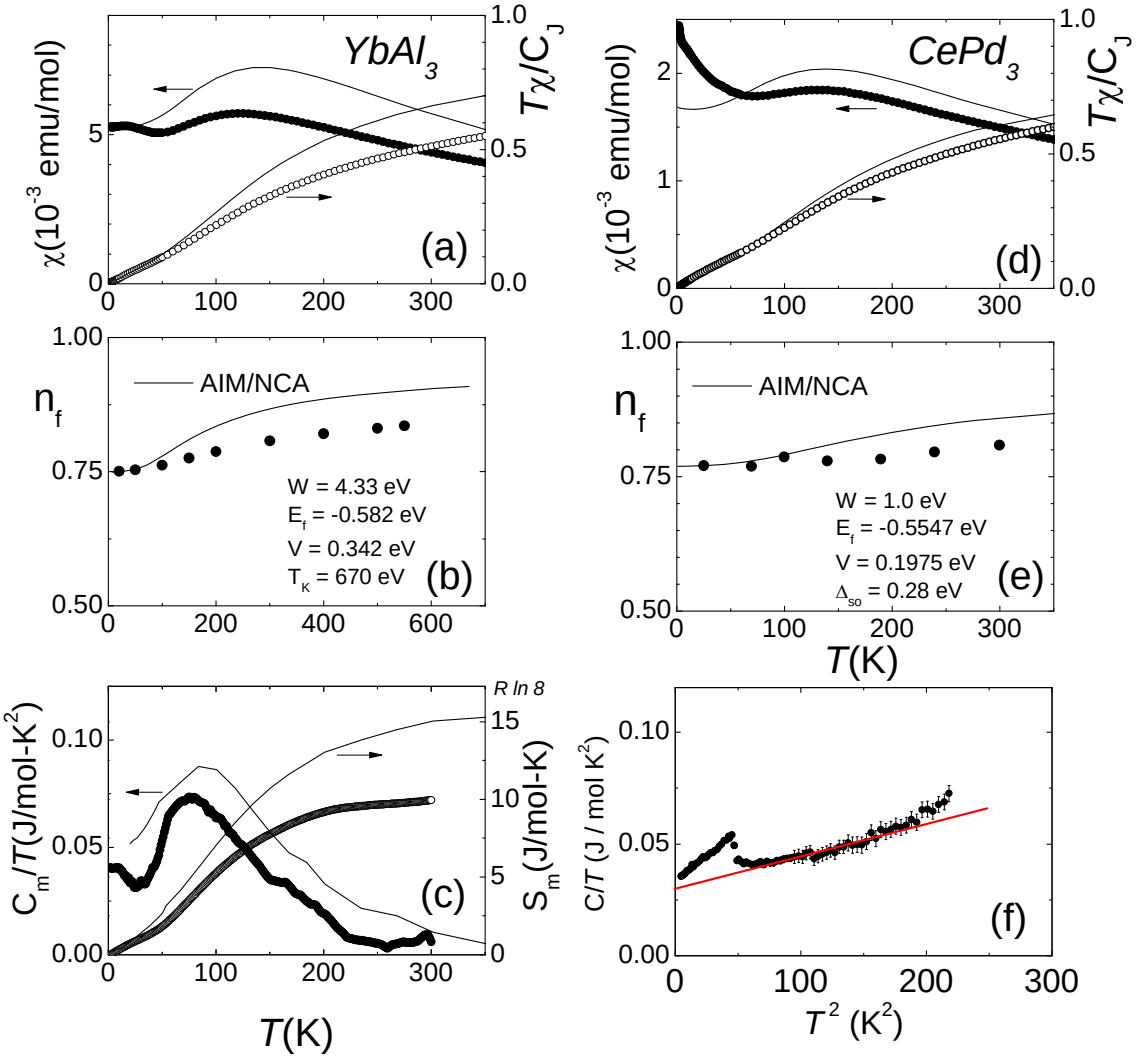

Figure 1.1: (a), (d) Magnetic susceptibility and the effective moment $T\chi$ /C_J for $YbAl_3$[1] and $CePd_3$[2], respectively; (b), (e) 4f occupation number, measured by L_3 X-ray absorption for $YbAl_3$[1] and $CePd_3$[3], respectively. (c) Magnetic contribution to the specific heat plotted as C_m/T and the corresponding entropy for $YbAl_3$[1]; (f) C/T vs. T^2 for $CePd_3$[4]. A value for γ of 30 J/mol-K^2 is obtained by extrapolation (red line). The lattice contribution was not subtracted in this case. We have included the results of NCA calculations (black lines) for the prediction of the Anderson impurity model (section 1.3.a), with parameters given in panels (b) and (e). NCA calculations for $YbAl_3$ are from reference [1] and those for $CePd_3$ were performed by C. H. Booth[9].

1.2.b Neutron Scattering

Inelastic neutron scattering (INS) has proven to be one of the most useful experimental methods for characterizing intermediate valence compounds. INS probes the excitations of solids, like the lattice excitations (phonons), the crystal electric field excitations and the spin-orbit interaction, the excitations of a magnetically ordered state (magnons), and the spin fluctuations of a paramagnetic state. In particular, the magnetic moment of the neutron interacts with the moments of the 4f electrons. After subtracting the contributions coming from nuclear scattering, phonons and multiple scattering events, the magnetic component of the scattering is obtained. It will be shown later that this part of the scattering contains the dissipative (imaginary) component of the dynamic susceptibility $\chi''\left(\vec{Q}, E\right)$ which depends on both the energy transfer E and the momentum transfer $\vec{Q}$ between the incident neutrons and the sample.

Few INS studies have been done on single crystals of IV compounds [10-14] with the consequence that we have an incomplete knowledge of the spin dynamics evolution over the reciprocal space. On the other hand, the numerous neutron experiments on polycrystalline IV compounds [15-17] show a crossover between two different regimes. In the high-temperature regime, the energy spectrum of χ"(E) reveals a quasielastic scattering with a Lorentzian power function representative of a relaxational spin dynamics. The half width Γ of the Lorentzian peak has the same energy scale $\Gamma \sim k_B T_{max}$ as the temperature for the maximum observed in both magnetic susceptibility and specific heat. On the other hand, in the low-temperature regime, the energy spectrum changes towards a damped inelastic Lorentzian. Figure 1.2 shows the magnetic contribution to the

intensity for $CePd_3$ at room temperature and at 7 K. These data are in agreement with a Lorentzian-like power spectrum, as it will be explained in chapters 2 and 3. At room temperature, this spectrum is quasielastic with a half width Γ of value 26.6 meV, whereas at 7 K the spectrum is inelastic [1], centered at 53 meV with Γ about 27 meV.

However, some discrepancies and controversies exist, mainly due to the disagreement in the methods used to subtract the non-magnetic contribution to the scattering [13, 14, 18].

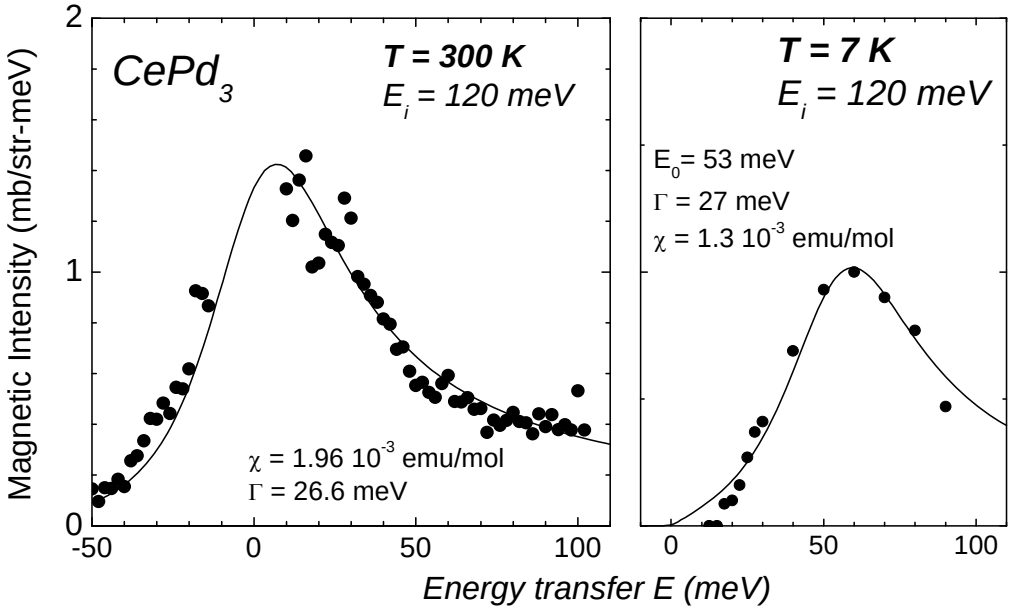

Figure 1.2: Magnetic contribution to the inelastic neutron scattering spectra from measurements on $CePd_3$ using the MAPS spectrometer at ISIS, Rutherford Appleton Laboratory, (a) at 300 K (section 3.1.b) and (b) at 7 K (section 2.3.a). Black lines are Lorentzian fits to quasi-elastic power spectrum at 300 K and to inelastic spectrum at 7 K, with parameters given in the panels.

[1] These results at 7 K are obtained after averaging over a region in the reciprocal space as explained in section 2.3.a.

1.2.c Scaling in Intermediate Valence Compounds

A very important property of the IV compounds is that the thermodynamic behavior is a universal function of a scaled temperature. That is, the zero-temperature magnetic susceptibility χ_0, the linear coefficient of the specific heat γ, and the energies Γ and E_0 from the spin dynamics spectrum scale as follows:

$$1/\chi_0,\ 1/\gamma,\ \Gamma,\ E_0 \propto\ k_B T_{max} \tag{1.2}$$

Given this scaling, it follows that also the effective quasiparticle mass m* scales as $1/T_{max}$. The Curie-Weiss temperature θ_{CW} scales with T_{max}.

The mass enhancement is also seen in the coefficient A of the quadratic temperature dependence of the resistivity $\rho \sim A\ T^2$, *i.e.,* there is also a scaling between A and the linear coefficient of the electronic specific heat γ known as Kadowaki-Woods (KW) relation, which holds for a number of IV compounds[5,6].

1.2.d Coherence in Intermediate Valence Compounds

In the low temperature regime of IV metals, there is an onset of coherence over the whole lattice as temperature decreases, which is remarkably evident in DC transport measurements. This can be illustrated by the electrical resistivity ρ of $CePd_3$ as a function of temperature, as shown in Figure 1.3.

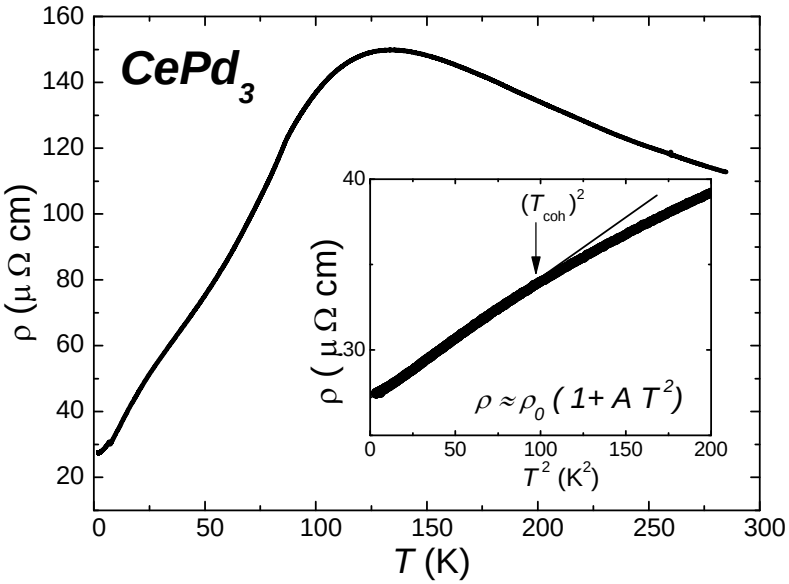

Figure 1.3. Evolution of resistivity of $CePd_3$ with temperature[4]. Inset: quadratic T-dependence of resistivity below T_{coh}.

Starting from the high-temperature local moment limit, ρ increases as the temperature decreases, arriving to a maximum, again around a temperature value T_{max}. This Kondo-like behavior can be associated to the increase of the scattering from the 4f magnetic moments, as we will discuss further in section 1.3.a below. These scattering centers sit on a periodic lattice, therefore, as the temperature keeps decreasing (with the consequent demagnetization and diminishing n_f) the resistivity starts decreasing, showing a coherent character. That is to say, the cooperative character of the scattering from the 4f moments is revealed through a Bloch-like resistivity that decreases to zero as the temperature goes to zero. In addition, a T^2 power law, characteristic of electron-electron scattering in a coherent FL, sets in around 10 K and 30 K for the case of $CePd_3$[4] and $YbAl_3$[1] respectively. This temperature scale, called T_{coh}, can be associated with the appearance of a coherent Fermi Liquid ground state. In fact, we will see that in IV compounds, this

coherence is strongly associated with the onset of renormalized quasiparticles bands in the low temperature FL regime.

Optical conductivity measurements [7] on $YbAl_3$ below 40 K show a Drude-like response corresponding to a heavy quasiparticle effective mass and another peak associated to the formation of the hybridization bands (Fig. 1.7). This structure persists as temperature goes down, supporting the existence of this coherent ground state with a hybridization gap below a scale $T_{coh} = 40$ K.

While optical conductivity gives evidence for the existence of the hybridization gap[7,20], de Haas van Alphen (dHvA) experiments give evidence for the inclusion of the f-electrons (usually localized) in the Fermi Surface as itinerant electrons. These dHvA experiments also directly exhibit the large enhancement of the effective masses[8, 21].

For some IV metals, anomalies are observed in the specific heat and in the magnetic susceptibility[1, 16] in the same temperature range T_{coh}, so they appear to be associated with the onset of coherence. Examples of these features are an upturn in C(T)/T around 30 K, and an increase of χ(T) below 40 K to a peak around 20 K for the case of $YbAl_3$ and an upturn in χ(T) below 50 K for $CePd_3$, as shown in Figure 1.1.

Understanding coherence implies recognizing the effect of including the lattice of 4f moments in the theoretical description. As we will see in section 1.3, the model that would account for this is the Anderson lattice model, but no complete solution exists yet.

An excellent probe for the presence of this coherent behavior among the 4f moments is measurement of the dynamic susceptibility that carries the information of the spin-spin correlations, through inelastic neutron scattering. By means of the study of both the dependence in momentum transfer Q and in the energy transfer E of the magnetic part of

the neutron scattering function, the evolution of the interactions between localized and delocalized electrons can be followed between the low and high-temperature regimes. In particular, the onset of coherence would be manifested as a distinct Q-dependence of χ"(Q, E) and the renormalized band structure in the FL ground state could be inferred from a detailed (Q, E) exploration. The study of the dependence on momentum transfer Q is only possible by using adequate single crystal samples. This is the subject of chapters 3 and 4.

1.3 Theoretical Overview.

In this section, we will present the Anderson impurity model and the Anderson lattice model on a simple basis quoting their calculation results to help us understand the thermodynamic and transport measured properties which have been presented in the previous section on the basis of these models.

1.3.a The Anderson Impurity Model

The Anderson Impurity Model (AIM) has proven to explain qualitatively and in some cases semi-quantitatively most of the phenomenological thermodynamic (but not transport) features exposed for IV metals, which is perhaps surprising, since the RE do sit on a lattice, rather than having the role of mere "impurities" [18, 22]. This model considers the situation of a "magnetic impurity", as for instance a rare earth atom with an

incomplete f-shell, embedded in a metal host. The "Anderson Hamiltonian" [23] is given by the sum of four terms:

$$\mathbf{H} = \sum_{\vec{k},\sigma} \varepsilon_{\vec{k}} C^{+}_{\vec{k},\sigma} C_{\vec{k},\sigma} + \sum_{\sigma} E^{f} f^{+}_{\sigma} f_{\sigma} + U f^{+}_{\uparrow} f_{\uparrow} f^{+}_{\downarrow} f_{\downarrow} + \sum_{\vec{k},\sigma} \left(V_k f^{+}_{\sigma} C_{\vec{k},\sigma} + V^{*}_{k} C^{+}_{\vec{k},\sigma} f_{\sigma} \right) \quad (1.3)$$

The first term in the Hamiltonian describes the uncorrelated itinerant conduction electrons, where $\varepsilon_{\vec{k}}$ is the energy dispersion relation for this conduction band with $C^{+}_{\vec{k},\sigma}$ and $C_{\vec{k},\sigma}$ being the creation and annihilation operators for electronic states of momentum $\vec{k}$ and spin σ. The second term denotes the energy of the impurity orbital for the simple case of a non-degenerate f orbital, with energy E^f, which is the difference between the energy of the states $4f^1$ and $4f^0$. This term includes the creation and annihilation operators f^{+}_{σ} and f_{σ} for an electron at the impurity site, with spin σ. The third term represents the cost in energy of having double occupancy at the impurity site due to the on-site Coulomb repulsion U. Finally, the last term represents the mixing between the conduction band and the impurity orbital, where the matrix element for this process is V_k. The hybridization energy for conduction electrons to hop on and off the 4f orbitals is $\Delta \sim V_k^2 \rho(\varepsilon_F)$, where $\rho(\varepsilon_F)$ is the density of conduction states at Fermi level ε_F.

Typically for the RE, the energy scales involved are: $\Delta \sim 0.1$ eV, $E^f \sim 1$ eV[2], and a large U ~ 10 eV, basically suppressing hopping into $n_f = 2$ state[3]. Consequently, the motion in and out of the f-orbital is slowed down from the bare rate $\Delta/\hbar$ to a renormalized

[2] E^f is measured from the chemical potential μ.
[3] This is usually referred as the $U = \infty$ Anderson model, and the theory is confined in the f^0-f^1 subspace.

rate $k_B T_K/\hbar$, where T_K is the Kondo temperature introduced next. Low-energy spin fluctuations arise from those virtual charge fluctuations: ($n_f = 1,\uparrow$) goes to ($n_f = 0$) and then to ($n_f = 1,\downarrow$), and these create narrow 4f resonance at the Fermi level, the so called "Kondo resonance".

In the Kondo limit of the Anderson Hamiltonian, where not only the repulsion U is much greater than the hybridization energy Δ, but also (ε_F - E^f) >> Δ, the charge fluctuation to f^0 are suppressed, ensuring single occupancy of the impurity site and therefore, the model describes a local spin interacting with a band of itinerant electrons via an exchange interaction J. The physics of the AIM is the same as that of the Kondo model[4], derived from (1.3) by a Schrieffer-Wolff transformation [24] to give:

$$H = \sum_{k,\sigma} \tilde{\varepsilon}_k \; C^+_{k,\sigma} C_{k,\sigma} + 2J \sum_k \vec{S}.\vec{S}_k \qquad (1.4)$$

where $\vec{S}$ and $\vec{S}_k$ are the spin operators for the impurity and for the conduction electron in the state $\vec{k}$ respectively. The physical reason for obtaining a spin dependence of the interaction when taking charge fluctuations into account, is that the Pauli Exclusion Principle forbids intermediate states in which the impurity site is occupied by two electrons of the same spin orientation. Below the so-called Kondo temperature T_K, the conduction electrons form a singlet state with the localized spin, quenching the magnetic moment.

[4] Schrieffer and Wolff carried out a canonical transformation and the subsequent diagonalization that showed the equivalence between both Hamiltonians.

The problem of magnetic impurities is well understood theoretically, with exact solutions via the renormalization group approach and via the Bethe Ansatz[5]. In addition, several approximate techniques proved to be useful in calculating the dynamic response functions that cannot be calculated via the Bethe Ansatz, like the dynamic susceptibility, required for comparison with neutron scattering experimental results. Taking into account the degeneracy factor N = 2J + 1, the so called "1/N approximation" or Non-crossing approximation (NCA) involves summing subsets of diagrams to low order in 1/N, and generates asymptotically exact solutions as N tends to infinity. They work very well even for finite values of N such as 6 or 8, those corresponding to Ce $4f^1$ and Yb $4f^{13}$ respectively[19].

In the high temperature regime, the AIM predicts a local moment behavior, with well localized f-electrons not coupled to the itinerant conduction electrons. The static magnetic susceptibility χ has a Curie-Weiss character, reflecting the magnetic moment of the partially filled f-shell. The dynamic susceptibility is that of the quasielastic dynamics of (free) local moments. The magnetic contribution to the entropy tends to the configuration value R ln(2J+1). In this limit, the valence, and therefore the f-occupation number tends to an integral value.

A crossover to the low temperature regime takes place around a scale of order T_K. In this limit, the hybridization results in a Kondo resonance, that causes an f-contribution to the density of states of order $\sim 1/k_B T_K$ at the Fermi energy ε_F. The specific heat varies linearly with T, and χ approaches a Pauli-like form, becoming almost T-independent. Due to the increase of the density of states at ε_F, the Pauli susceptibility and the specific

[5] Solution based on the Ansatz used by Bethe in 1931 for the one-dimensional Heisenberg model, on the assumption of a linear dispersion for the conduction electrons.

heat linear coefficient γ are also enhanced by a factor T_F/T_K (where T_F is the Fermi temperature), this is around two orders of magnitude larger than those of conventional metals, with $\gamma = \frac{\pi^2}{2} N k_B \frac{1}{T_F}$ in the order of few mJ/mol K^2). The valence has a non-integral value ($n^f < 1$) in this regime. The energy of the system is lowered by $k_B T_K$, and it is possible to describe this behavior as that of a Fermi Liquid of quasiparticles. At these temperatures, the dynamics of the f-spin fluctuations are those of a localized, damped oscillator with characteristic energy $E_0 \sim k_B T_K$ given by

$$\chi'' \propto \frac{\chi(T) E \Gamma}{(E - E_0)^2 + \Gamma^2} \tag{1.5}$$

This model also shows universality, this is, properties as specific heat, magnetic susceptibility $\chi(T)$ and spin dynamics spectrum $\chi''(E)$ scale as $1/T_K$, as well as the effective quasiparticle mass m*. As stated by its name, the AIM treats systems with dilute concentrations of magnetic impurities. However it still gives a good description of the valence, specific heat, static and dynamic susceptibility of IV compounds, where the 4f ions sit on a periodic lattice, a situation that is far from the impurity limit. The quantities mentioned are thermodynamic properties and are dominated by spin fluctuations. Therefore, a possible explanation for this notable agreement may reside on the fact that the spin fluctuations are of local character in these materials[6].

As an illustration of the good agreement between the data and the AIM, a non-crossing approximation NCA calculation[1, 6] is included in figure 1.1. For the IV metal $YbAl_3$ the experimental results for $\chi(T)$, $C(T)/T$ and $n^f(T)$ qualitatively follows the temperature dependence given by the model predictions (Fig. 1.1). The fit requires just three parameters: hybridization amplitude V, excitation energy E^f and background

conduction band width W. The first two parameters are chosen to match the T = 0 K values of 4f occupation number $n^f(0)$ and the susceptibility $\chi(0)$. W is obtained from the linear coefficient of C(T) of the non-magnetic counterparts compound, in this case $LuAl_3$, which is assumed to account for the contribution of the $YbAl_3$ non-magnetic background. For the case of $YbAl_3$, the AIM predicts an inelastic Lorentzian lineshape (equation 1.5) for the power spectrum of the dynamic susceptibility, with parameters $E_0 = 40$ meV and $\Gamma = 22$ meV, reasonably close to the experimental values obtained at T = 6 K: $E_0 = 44$ meV and $\Gamma = 32$ meV (section 4.2). The values for the parameters are shown in figure 1.1(c). A NCA calculation was also performed for $CePd_3$[9], and the results (black line) for the predicted $\chi(T)$, and $n^f(T)$ are also plotted in figure 1.1. The values of the parameters for this calculation are included in figure 1.1(e).

In addition, another IV compound where the AIM predictions describe the experimental results in a remarkably good quantitatively manner is $YbAgCu_4$[16]. Figure 1.4 shows the agreement between the results of the NCA calculations and the measured data for $\chi(T)$, $n^f(T)$ and the spectra of the magnetic contribution to the inelastic neutron scattering.

In contrast, the AIM does not provide a complete explanation for the observed transport properties. This is expected on basic grounds for the DC resistivity at low temperatures. The AIM predicts a non-monotonic temperature dependence as follows: as T goes down, resistivity decreases driven by the decreasing T^5 electron-phonon scattering contribution. As T reaches values around T_K, there is an increase of resistivity due to the onset of the Kondo resonance with its resulting spin-scattering of conduction electrons. Then, as T continues decreasing the magnetic moment is quenched and resistivity reaches

saturation at zero temperature. In fact though, since in IV metals, the 4f ions sit on a periodic lattice, Bloch's law requires that the resistivity must vanish as the temperature goes to T = 0 K. These temperature dependences are shown schematically in Fig 1.5.

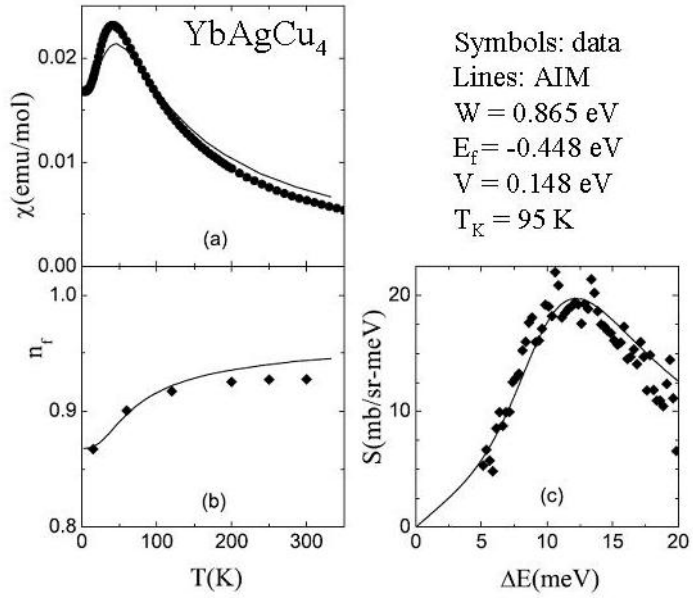

Figure 1.4: From references [16, 3], comparison of experimental measurements on the compound $YbAgCu_4$ to NCA calculations for the Anderson impurity model. (a) Magnetic susceptibility, (b) 4f occupation number and (c) inelastic magnetic neutron scattering results.

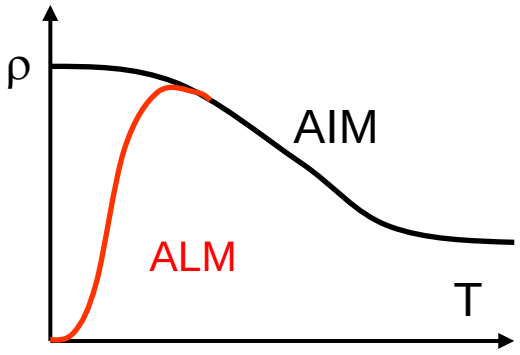

Figure 1.5: Scheme for the low temperature dependence of the resistivity ρ for both the Anderson impurity and Anderson lattice models.

1.3.b The Anderson Lattice Model

In section 1.2.d, it was shown that the low temperature resistivity of IV compounds has a Bloch-like behavior and goes as $\rho \sim AT^2$ indicating a Fermi Liquid "coherence" in the scattering. To account for these features, a lattice of 4f-ions should be included in the theory. One way, is to treat the 4f electrons as itinerant via a band theory, and the other way is by means of the Anderson Lattice Model (ALM). The former includes the hybridization but not the strong local electron correlations and temperature dependence. However it gives ground state properties such as the Fermi surface (FS) geometry. The ALM is complementary to the band theory: it naturally includes correlations and temperature dependence, but cannot include details of the FS that come from band structure calculations. The ALM is an extension of the AIM that assumes a periodic array of local magnetic moments, as shown by the Hamiltonian

$$\mathbf{H} = \sum_{\vec{k},\sigma} \varepsilon_{\vec{k}} C^{+}_{\vec{k},\sigma} C_{\vec{k},\sigma} + \sum_{i} \left[\begin{array}{l} \sum_{\sigma} E^{f} f^{+}_{i,\sigma} f_{i,\sigma} + \sum_{\vec{k},\sigma} \left(V_k f^{+}_{i,\sigma} C_{\vec{k},\sigma} + V^{*}_{k} C^{+}_{\vec{k},\sigma} f_{i,\sigma} \right) \\ + U \; f^{+}_{i,\uparrow} f_{i,\uparrow} f^{+}_{i,\downarrow} f_{i,\downarrow} \end{array} \right] \quad (1.6)$$

This model is also known as Periodic Anderson Model (PAM). Here E^f is the dispersionless energy for the f-states, and the f^+, f operators include a site index i. E^f sits slightly below the Fermi level ε_F of the bare conduction band of width W. As before, the hybridization and the strong on-site Coulomb repulsion U terms are also included. The bare f-band width W_f is smaller than the hybridization amplitude V.

In contrast to the impurity case, there is no exact solution for the Periodic Anderson Model[6]. As a consequence of the strong on-site interaction between f electrons, the Coulomb term cannot be treated as a perturbation U. Several approximations have been performed.

An alternative perturbation theory, called the slave boson approximation, which is suitable for the lattice problem, involves a representation of the operators in terms of conventional boson and fermion creation and annihilation operators. The physical interpretation is to represent the spinless valence state f^0 by a boson that it is created when an f-electron hops out of the RE ion and destroyed when a conduction electron hops into the RE ion, so that the number operator for the total number of f-electron plus bosons is conserved. In the Mean Field approximation, the boson operators are replaced by their expectation values. The mean fields are determined by minimization of the free energy with respect to these variables.

These approaches[25-28] show two energy scales. The specific heat has a two-peak structure, one at T_K for the onset of Kondo resonance and the second at much lower temperature that evidences the FL regime[29].

Among other methods used, we can mention the variational technique [30], dynamic mean field theories, combination of coherent potential approximation and functional integral method [31, 32]. All of these approximations have some basic common features. At high temperatures, they predict a local moment limit, as in the case of the AIM, with a crossover to an enhanced Pauli paramagnetism at low temperatures, this time in a

[6] An exact treatment of the one-dimensional Anderson Lattice using a density-matrix formulation of the numerical renormalization group, is reported by M. Guerrero, and Clare C. Yu, Phys. Rev. B **51**, 10301 (1995).

periodic hybridized band. The ALM predicts a crossover between these regimes which is slower than the one predicted by the impurity model[30, 33].

The ALM calculations agree in the formation of narrow coherent hybridized bands of low-energy excitations. These bands are similar to those that would be obtained by diagonalization of the non-interacting part of the Hamiltonian (given by the first three terms in equation 1.6), that is, by treating the crossing of the wide conduction band with the dispersionless f-band for the U = 0 case. This assumes that the strong Coulomb repulsion U merely renormalizes the parameters without changing the general behavior [34,35]. The renormalized quantities are the effective potential $\widetilde{V}_k$ (to include many-body effects) and the dressed energy $\widetilde{E}^f$. The branches $\omega_{\vec{k}}^{\pm}$ of the quasiparticle spectrum are found by standard methods to be given by

$$\omega_{\vec{k}}^{\pm} = \frac{1}{2}\left(\varepsilon_{\vec{k}} + \widetilde{E}^f \pm \sqrt{\left(\varepsilon_{\vec{k}} - \widetilde{E}^f\right)^2 + 4\left|\widetilde{V}_k\right|^2} \right) \tag{1.7}$$

These branches are displayed in figure 1.6.

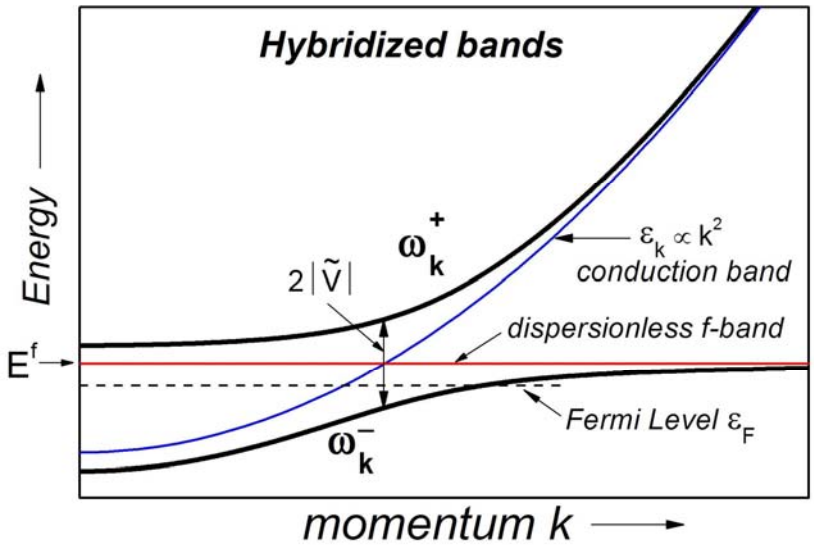

Figure 1.6. Dispersion of the hybridized bands near the Fermi Level. The direct gap has a value $2\tilde{V}$. The Coulomb interaction U is assumed to merely renormalize the parameters V and E^f.

The best evidence for the hybridized gap is given by measuring the optical conductivity σ [20]. The spectra of the $YbAl_3$ compound measured[7] over wide ranges of energy and T exhibits a narrow Drude peak (response of the free carriers), a pronounced mid-infrared peak centered around 250 meV, and the appearance of a strong depletion (pseudogap) around 30 meV, below 120 K (in the order of T_{max} of $YbAl_3$), as shown in figure 1.7. This pseudogap has a shoulder at 60 meV of order k_BT_K. Below the coherence temperature (T_{coh} ~ 40K for $YbAl_3$[1]), the pseudogap is clearly observed, consistent with a well established hybridization gap.

Optical transitions (with zero momentum transfer) across the direct gap, as the one sketched in figure 1.7, explain the 250 meV peak. These transitions should give a sharp threshold at an energy around $2\tilde{V}$. In addition, indirect transition across the gap, can

introduce a tail from $2\tilde{V}$ down to the value of the indirect gap of order $k_B T_K$. Lattice disorder, many-body scattering, and phonon assisted excitations may provide the required momentum transfer for indirect gap transitions. In figure 1.7(b), the dashed line represents the spectrum for σ when only direct transitions are present, and the broadening effect of indirect transitions is illustrated by the solid line. The Drude peak arises from intraband transitions across the Fermi level, which lies in a region of high density of states near the zone boundary of the upper band (figure 1.6). From a generalized Drude analysis of the data at 8 K, an effective mass of 30 m_0, where m_0 is the bare band mass, and a scattering rate with quadratic energy dependence as expected for a Fermi-liquid. These features and their temperature dependences can be qualitatively understood using the ALM.

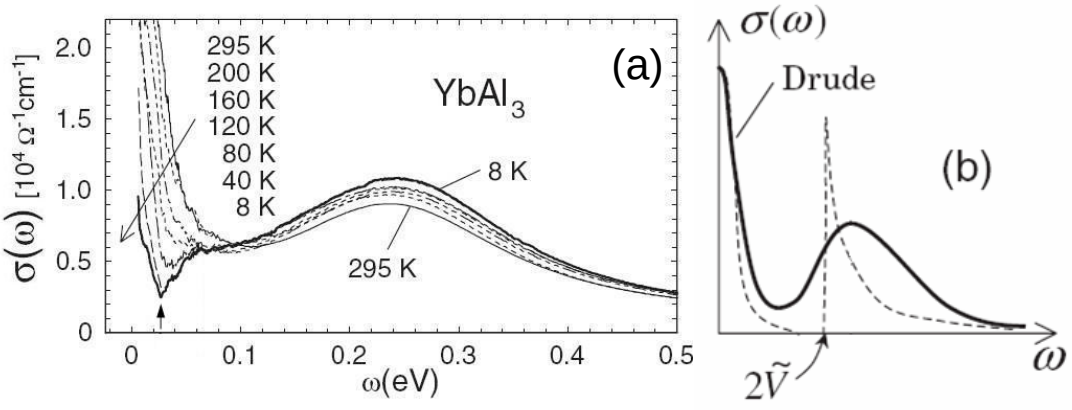

Figure 1.7: From reference [7], (a) optical conductivity spectra σ(ω) of $YbAl_3$. The vertical arrow indicates the pseudogap around 0.03 eV. (b) Sketch of σ(ω) as expected from transitions between the hybridized bands $\omega^{\pm}(k)$. In dashed lines, σ(ω) with only direct transitions.

The ALM naturally predicts coherence as a result of the periodicity of the lattice. Whereas the AIM involves only one scale of energy ($k_B T_K$) for the onset of the local singlet state and the screening of the local moment, the ALM yields two energy scales, one of them being T_K, since magnetic moments can still be screened locally, and the second scale of energy ($k_B T_{coh}$) for the formation of a coherent Fermi liquid over the whole lattice with a large FS including both the conduction electrons and the f-electrons[29]. Coherence effects will appear as T decreases, and the transport properties are going to be very different between AIM and ALM, with Bloch's law arising from the periodic array of impurities, with a temperature dependence of the resistivity as $\rho = \rho_0 + A T^2$.

At low temperatures, calculations for the Anderson lattice show the onset of quasiparticle hybridization bands. The dynamic spin susceptibility and neutron scattering cross sections calculations reveal a highly Q-dependent scattering, consistent with interband excitations across the hybridization gap. An inelastic peak is obtained with a maximum of intensity when the energy transfer equals the threshold for indirect transitions between the regions of large density of states at the zone center and zone boundary of the upper and lower bands (Fig. 1.6) and the momentum transfer is at the zone boundary, such as to connect these regions. As Q goes to zone center, *i.e.,* as Q decreases, the peak intensity decreases. In the case of IV compounds, where the Fermi level does not lie in the gap (*i.e.*, IV metals), an additional contribution to the scattering arises from intraband transitions, with a linear Q-dependence, as expected for Fermi liquids on basic grounds.

A physical simple explanation of the inelastic neutron scattering that includes both interband transitions across the hybridization gap as well as intraband transitions is given in figure 1.8. The sum over all excitations from occupied to unoccupied states with energy transfer E and momentum transfer Q in a simple two-band model will represent the scattering function for intra and interband particle-hole excitations. This is given by

$$S(\vec{Q}, E) \propto \int dE' f(E')\big(1 - f(E')\big) D(E', E'+E; \vec{Q}) \tag{1.8}$$

where D is the joint density of states for both types of transitions between the bands ω^+ and ω^- given by equation 1.7, and f(E') is the Fermi-Dirac distribution. We performed a simple calculation in a 3-dimensional system, with a basic two-band structure sketched in figure 1.8(a). The resulting spectra are shown in figure 1.8(b). The interband spectra (circles) of excitations has an intensity peak that is centered at an energy value close to the indirect gap for a momentum transfer Q of magnitude equal to $\frac{\pi}{a_0}$, *i.e.*, $\vec{Q} = \vec{Q}_{BZ}$ (Brillouin zone boundary). For other values of Q, the peaks move to higher energies as Q goes from zone boundary to zone center. On the other hand, the intraband transitions (lines) have a different Q-dependence: peaks move to smaller energies as Q goes from zone boundary to zone center.

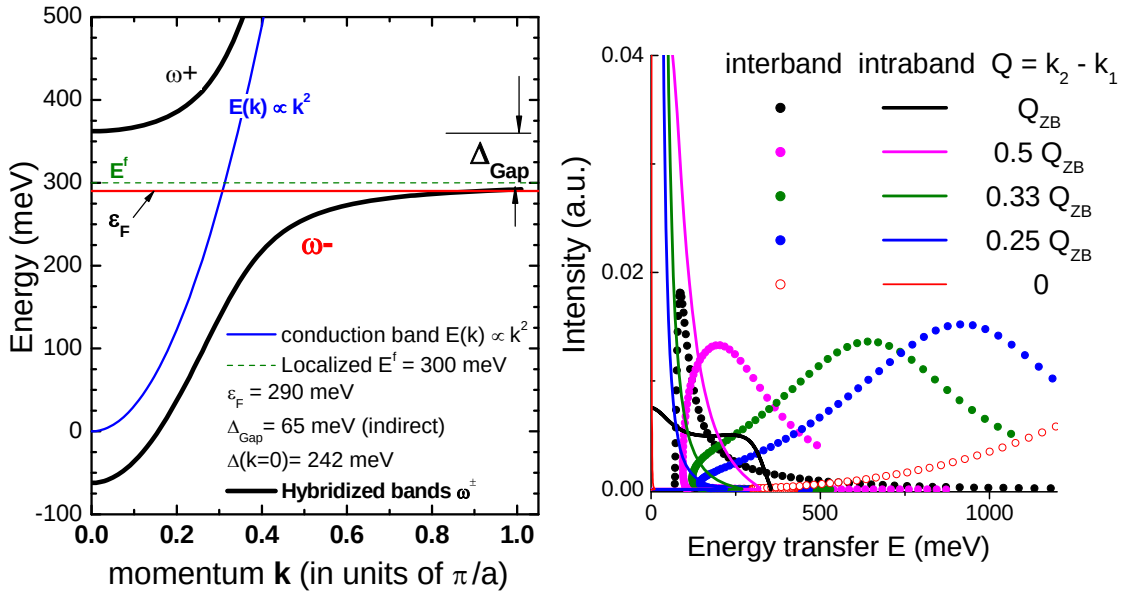

Figure 1.8: A simple estimation for the spectrum of particle-hole excitations for a basic scheme of hybridized bands. Panel (a) displays a dispersionless E^f band (dashed green line), a conduction band (blue line), and hybridized bands ω^+ and ω^- (black line) obtained from equation (1.7). The Fermi energy ε_F and the indirect gap Δ_{GAP} are also shown. The values for the parameters used are also included. (b) Spectra for intraband (lines) and interband (circles) excitations for momentum transfer in the range between 0 and $Q=Q_{ZB}$.

Real, many-body theoretical calculation of the magnetic dynamic susceptibility, within an approximation of the ALM are given in references [30-32,34]. The results are similar to those of our simple calculation from figure 1.8(b), in that a two-peak structure is obtained: a low energy quasielastic peak, and a high energy broad peak coming from intraband and interband excitations, respectively. The results for the scattering function S(Q, E) from some of these calculations [18, 20] are shown in figure 1.9. The spectrum of S(Q,E) calculated for different values of momentum transfer, shows that the peak for

intergap excitations is maximum for momentum transfer Q at zone boundary and moves to high energies as Q decreases. On the other hand, the intraband peak position increases linearly with momentum transfer Q.

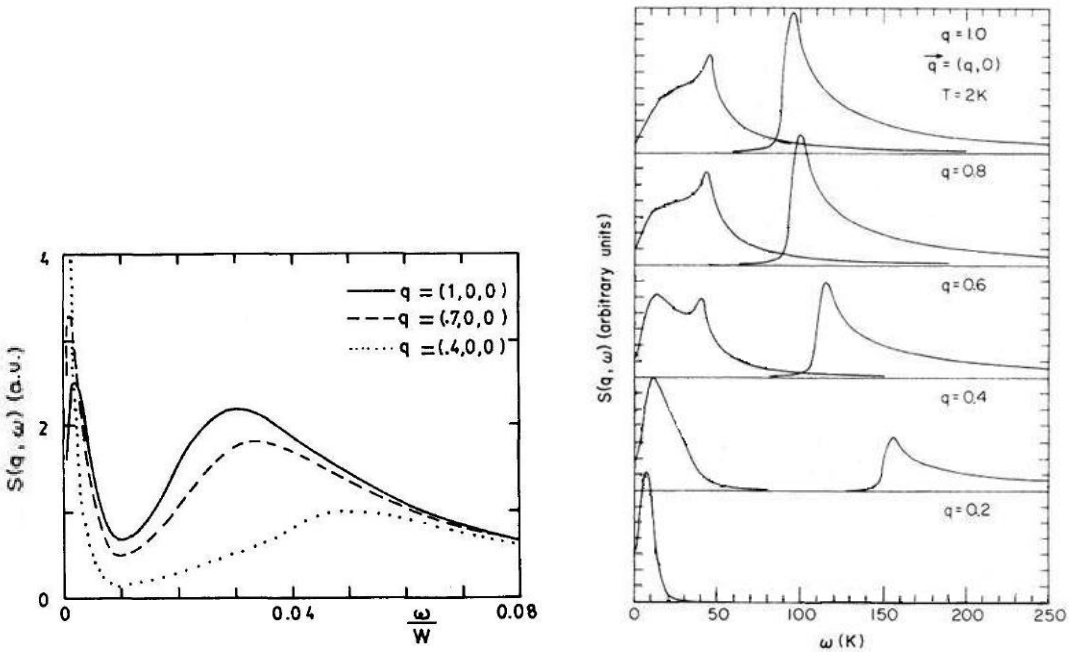

Figure 1.9: Spectra of S(Q, E) for different values of momentum transfer q, (a) from reference [31], and (b) from reference [30]. The high energy peak (interband transitions) is maximum for q at zone boundary. The low energy peak (intraband transitions) moves to high energies as q increases towards zone boundary.

1.4 Objectives and Dissertation Organization

Since most of the neutron scattering experiments on IV compounds were done in polycrystalline samples and since single crystals of excellent quality and proper size had been available during these last few years, we have an opportunity to measure the properties of interest related to spin dynamics.

In particular we will study the momentum transfer dependence of the magnetic part of the neutron scattering to test the predictions of the Anderson Lattice model concerning the hybridization gap in the density of states. We will explore the onset of coherence in the ground state at low temperatures and we will study the local moment behavior at high temperatures to test the prediction from the Anderson Impurity model. We will confirm the existence of new excitations beyond the usual Kondo scattering, in the low temperature regime of IV compounds for $YbAl_3$.

The organization of this dissertation is as follows: Chapter 1 has been devoted to a description of the general experimental properties of intermediate valence compounds and of the basic theoretical background. Calculations from the Anderson impurity model and the Anderson lattice model for some quantities were presented, in particular for those that depend on spin fluctuations, namely magnetic susceptibility, specific heat and dynamic susceptibility. In Chapter 2, the samples growth methods are mentioned, the inelastic neutron scattering technique is introduced and the instruments employed are described. A method to separate the magnetic from the non-magnetic contribution in the scattering intensity is discussed. Chapter 3 and 4 present the inelastic neutron scattering results for $CePd_3$ and $YbAl_3$ respectively, with an analysis of the observed features at the

low and high temperature regimes of these intermediate valence compounds. Finally, the results of this thesis will be given in Chapter 5. These conclusions will stress that the magnetic response of these compounds is basically that of the Anderson impurity model, with only a moderate momentum transfer dependence resembling the coherent character of the ground state predicted by the Anderson Lattice model.

Chapter 2

Experimental Techniques

In this chapter we describe the sample characteristics, and we introduce the experimental technique of neutron scattering, with a brief description of the instruments used on the measurements and the instrumental configurations. In addition, one of the sections is devoted to a method for obtaining the magnetic contribution to the scattering in $CePd_3$ by subtraction of the non-magnetic component, obtained from measurements on the non-magnetic compound $LaPd_3$. Finally, a note on the multiple scattering and a correction due to “spurions” are included at the end of this chapter.

2.1 Sample Preparation

The $YbAl_3$ samples used were single crystals grown by the self-flux method[37], by precipitation from excess aluminum. Four crystals were used of total mass of 5 grams approximately, prepared by Andy Christianson and Eric Bauer at Los Alamos National Laboratory.

As will be explained latter, to obtain the magnetic response of $CePd_3$, the non-magnetic analog compound $LaPd_3$ was also prepared, under the assumption that the latter has the same lattice dynamics of $CePd_3$. The single crystalline $CePd_3$ and $LaPd_3$ samples were prepared by the Czochralski method by Kenneth McClellan and Eric Bauer at Los Alamos National Laboratory**.** In this method, a polycrystalline "charge" is melted in a tri-arc furnace in an argon atmosphere. A seed crystal mounted on a rod is dipped into the molten compound and pulled upwards and rotated simultaneously. By controlling the temperature, the rate of pulling and the speed of rotation, a single-crystalline cylindrical ingot will grow from the seed. Figure 2.1 shows the samples obtained: a $CePd_3$ crystal of 0.5 cm of diameter and 5 cm long, with a mass of 17.72 g and a $LaPd_3$ crystal of 0.6 cm of diameter and 3 cm long, with a mass of 10.55 g. The $LaPd_3$ sample received a thermal treatment (annealing at 950^oC for 6 days) to improve the quality of the crystal. Both neutron and X-ray diffraction confirmed that the samples were single phase.

$YbAl_3$, $CePd_3$, and $LaPd_3$ have the cubic $CuAu_3$ crystal structure. The values for the lattice parameters a_0 (at room temperature) are 0.42 nm for $YbAl_3$, 0.4126 nm for $CePd_3$, and 0.4226 nm for $LaPd_3$.

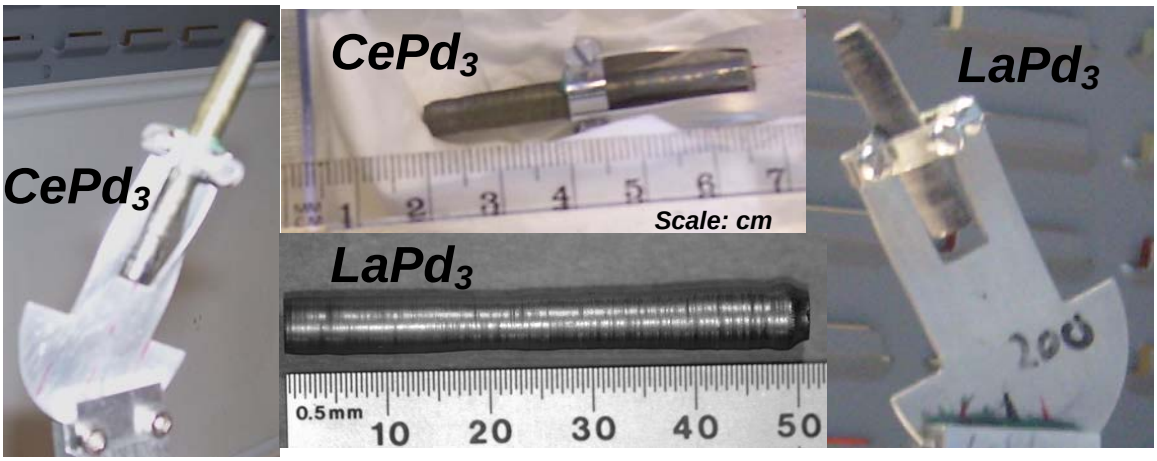

Figure 2.1: Single crystals of $CePd_3$ (18 g) and $LaPd_3$ (11 g) grown by the Czochralski method. The aluminum sample holders used in both cases for neutron scattering are also shown.

2.2 Inelastic Neutron Scattering

A neutron scattering experiment involves measuring the intensity of neutrons scattered from a beam incident on a sample. The scattering process changes the wave vector of the neutron and may change its energy. From the laws of momentum and energy conservation, the momentum transfer $\vec{Q}$ and the energy transfer E are given by

$$\vec{Q} = \vec{k}_f - \vec{k}_i$$

$$E = E_i - E_f = \frac{\hbar^2}{2m}\left(k_i^2 - k_f^2\right) \tag{2.1}$$

where $\vec{k}_i$ ($\vec{k}_f$) is the incident (final or outgoing) neutron wavevector, E_i (E_f) is the incident (final) neutron energy, $\hbar$ is the Plank's constant and m is the neutron mass. In the case of $k_i > k_f$, energy is transferred from the incident neutron to the sample and an

excitation is created in the solid. In the opposite case, an excitation is annihilated and the scattered neutron gains a quantum of energy.

The fraction of neutrons from an incident flux onto a scattering system scattered into a given solid angle $d\Omega$ in the direction $\vec{k}_f$, with a final energy between E^f and $E^f + dE$ is given by the double differential cross section $\frac{d^2\sigma}{d\Omega\, dE}$. The neutron acts as a very weak perturbation of the scattering system and using the Fermi's Golden Rule, together with the Born approximation for the interaction, the differential cross section[38] is given by

$$\frac{d^2\sigma}{d\Omega\, dE} = N \frac{k_f}{k_i} \; S(\vec{Q}, E) \tag{2.2}$$

where N is the number of scattering centers in the sample, and $S(\vec{Q}, E)$ is the scattering function. The latter quantity depends on the nature of the particular scattering process. The momentum and energy transfer dependent scattering function contains information on the time-dependent pair correlation function of the scattering system.

The purpose of most neutron scattering experiments is to measure $S(\vec{Q}, E)$ to determine the microscopic properties of the system under study. For instance, in nuclear elastic scattering from a crystal, the scattering function $S(\vec{Q}, E)$ will contain the potential for the interaction between the neutron and the atomic nuclei at the lattice sites. Alternatively, for inelastic phonon scattering, when a neutron creates (or destroys) a single phonon, the scattering function $S_{ph}(\vec{Q}, E)$ involves the response (frequencies and damping) of harmonic oscillator-like modes in the scattering system. The scattering function is proportional to the squared dynamic structure factor as expressed by

$$S_{phon,S}(\vec{Q},E) \propto \left| \sum_i b_i \, (\vec{Q}.\vec{\varepsilon}_{i,S}) \, e^{i\vec{Q}.\vec{R}_i} \, e^{-W_i} \right|^2 \tag{2.3}$$

where i is the site index within the unit cell, b_i and $\vec{R}_i$ are the scattering length and the atomic position of the i^{th} element, and $\vec{\varepsilon}_{i,S}$ is the polarization vector of the vibration mode S. The Debye-Waller factor e^{-W_i} originates from the thermal average of the atomic displacements. For polycrystalline scattering, after averaging over all the possible directions of $\vec{Q}$, the resulting scattering is proportional to the total scattering cross section, that is, coherent plus incoherent scattering, and, in the case of a cubic crystal, is proportional to the squared modulus of the momentum transfer[38]:

$$S_{phon}(Q,E) \propto \left(\frac{1}{1-e^{-E/k_BT}} \right) e^{-2W} \frac{\left\langle \left(\vec{Q} \, . \, \vec{\varepsilon}\right)^2 \right\rangle}{E} G(E) \propto Q^2 \tag{2.4}$$

The factor in brackets is related to the thermal population of excitations, and is also known as the thermal factor $(n(E)+1)$ or Bose factor, G(E) is the phonon density of states, and the average of $(\vec{Q}.\vec{\varepsilon})^2$ is taken over all modes with energy E.

Another example of scattering function $S(\vec{Q},E)$, is the magnetic scattering cross section for an isotropic paramagnet[39], given by

$$\frac{d^2\sigma}{d\Omega \, dE} = \frac{k_f}{k_i} (\gamma \, r_e)^2 \, S_{magn}(\vec{Q},E) \tag{2.5}$$

where k_i and k_f were defined previously, $(\gamma \, r_e)^2$ is a coupling constant that depends on the neutron magnetic moment γ and the classical radius of the electron. S_{magn}, the magnetic scattering function, is the Fourier transform in time and space of the spin-spin correlation function. Since the neutron is applying a small perturbation to the spin system, the

response of the system is proportional to the spectrum of spontaneous fluctuations (fluctuation-dissipation theorem). In other words, the magnetic scattering is just the dissipative part of the $(\vec{Q}, E)$-dependent dynamic susceptibility $\chi''(\vec{Q}, E)$.

$$S_{magn}(\vec{Q}, E) = \frac{1}{\pi}\left[\frac{1}{1 - e^{-E/k_B T}}\right]\chi''(\vec{Q}, E) \tag{2.6}$$

The imaginary and real parts of the dynamic susceptibility are related by the Kramers-Kronig relations, and χ" can be rewritten as

$$\chi''(\vec{Q}, E) = f^2(Q)\ \chi'(Q)\, E\ P(\vec{Q}, E) \tag{2.7}$$

where $f^2(Q)$ is the magnetic form factor, which is the Fourier transform of the magnetization spatial density around the atom, and P(E) is a power spectrum which for paramagnetic scattering and in the case of excitations with a finite life time[38] has a Lorentzian lineshape:

$$P(\vec{Q}, E) = \frac{\Gamma_Q}{2\pi}\left[\frac{1}{\left(E - E_0(\vec{Q})\right)^2 + {\Gamma_Q}^2} + \frac{1}{\left(E + E_0(\vec{Q})\right)^2 + {\Gamma_Q}^2}\right] \tag{2.8}$$

Here, Γ_Q is the linewidth, that is, the half width at half maximum of the peak and E_0 is its centroid. The first term in the bracket corresponds to the creation of the excitation and the second one, called the anti-Stokes term, the annihilation of it.

In section 2.3, we will discuss how to separate the magnetic from the non-magnetic contributions to the neutron scattering in IV compounds.

2.2.a Neutron Scattering Instruments

In neutron scattering experiments it is crucial to have information about the energy as well as the direction of both the incident and scattered beams. Among the different types of instruments used to measure the inelastic response of materials, we will briefly describe time-of-flight and triple-axis spectrometers. The differences in design between these instruments are based on the nature of the neutron sources used.

Neutron beams are produced in nuclear reactors as well as in the so-called spallation sources. In a reactor, a continuous flux of neutrons is the sub-product of the nuclear fission reactions, and by means of repeated collisions with moderators, neutrons are "cooled" to the required thermal wavelengths. At the High Flux Isotope Reactor (HFIR) located at Oak Ridge National Laboratory, the Maxwellian distribution of neutron velocities has a maximum between 60 and 80 meV. On the other hand, at spallation sources, a heavy metal target is bombarded with a regular sequence of sharp pulses of highly energetic protons and pulses of neutrons are created. At ISIS, a spallation neutron facility, located at Rutherford Appleton Laboratory (UK), protons are accelerated to 800 MeV, and the frequency of neutron pulses is 50 Hz. Moderators are also used to decrease the high kinetic energy of the neutrons.

In the triple-axis spectrometer (TAS), used primarily in reactor facilities, a monochromator defines the direction and magnitude of the wave vector for the incident beam. This is achieved by Bragg scattering from monochromator crystals. The direction and energy of the scattered beam is determined by another monochromator crystal called

an analyzer, before entering the neutron detector. This spectrometer is shown schematically in figure 2.2(a). The name triple axis comes from the fact that the sample, monochromator and analyzer can be rotated, allowing the TAS to probe nearly any coordinates in energy and momentum space in a controlled manner. This factor allows both for scans of energy transfer at constant momentum transfer $\vec{Q}$, and for scans varying the components of $\vec{Q} = (2\pi / a_0)(h,k,l)$ at constant value of the energy transfer.

In the time-of-flight technique (TOF), a velocity selector, usually called a chopper, monochromates the incident neutron beam that next interacts with the sample exchanging momentum and energy. A scattered (polychromatic) beam of neutron is then produced and collected in an array of detectors covering a wide angular range. Measuring the time of flight from the chopper to the detectors determines the final energy of the scattered neutrons and the direction of their wave vector $\vec{k}_f$ is determined through position sensitive detectors. TOF spectrometers are able to probe the sample response function over a wide portion of reciprocal space simultaneously. A TOF spectrometer is shown schematically in figure 2.2(b).

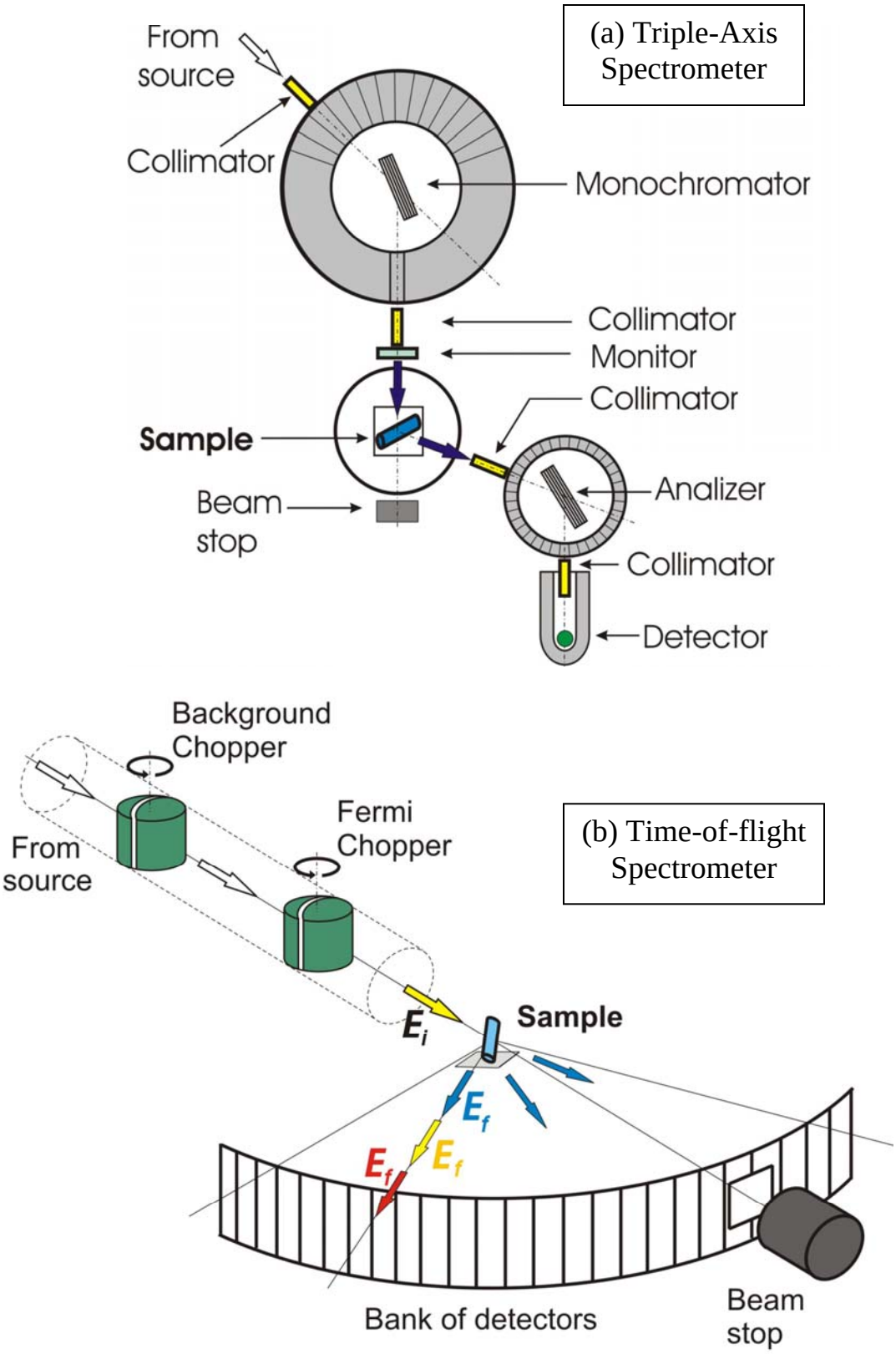

Figure 2.2: Schematic representation of (a) triple-axis spectrometer and (b) time-of-flight spectrometer.

TAS is ideal for experiments where information is needed on specific features well localized in ($\vec{Q}$, E) space. In contrast, TOF is ideal for studies where large portions of ($\vec{Q}$, E) space need to be explored. In TOF spectrometers, energy transfer scans at constant $\vec{Q}$ or reciprocal space surveys at constant E are not possible for a fixed orientation of a single crystal sample. From energy and momentum conservation (equations 2.1), it can be seen that at a fixed incident wave vector $\vec{k}_i$, a variation in $\vec{k}_f$ entails a variation of both the magnitude and direction of momentum transfer $\vec{Q}$ in addition to a variation of the energy transfer. In other words, the three components of $\vec{Q}$ and E are coupled, and only three of these four variables (h, k, l, and E) are independent. However, for a sequence of several sample orientations it would be possible to build the equivalent constant $\vec{Q}$ scans, but with a consequent increment in required beam time[40].

To explore the differences in using both types of spectrometers for the case of the IV compound $CePd_3$, figure 2.3 shows the intensity of the scattered neutrons measured by a triple-axis spectrometer and by a time-of-flight spectrometer for comparable energy-transfer ranges and in similar regions in the reciprocal space for the same single-crystalline sample. Panel (a) in figure 2.3 compares the intensities in units of monitor counts (1 mcu ≈ 1s) for (i) raw data for the $CePd_3$ sample collected after 9 hours on the HB3 TAS at HFIR, (ii) the "background scattering" measured under identical conditions, with the sample removed from the sample container can and (iii) the intensity from the $CePd_3$ sample itself, after subtraction of the sample can contribution. In Panel (b), the same comparison is held after 12 hours of neutron collection on the MAPS TOF spectrometer at ISIS, in a different region of the reciprocal space. Despite the fact that the

TAS may sound more efficient than TOF from the point of view of a brighter neutron flux incident on the sample, the comparison shows that the triple axis has higher background, and lesser statistics when compared to the TOF data. Part of the reason is due to the Maxwell profile of the reactor. In the case of $CePd_3$, the energy transfer range of interest, between 30 and 80 meV, requires incident neutrons energies between 45 and 95 meV, with the consequent loss of flux as soon as we move out from the peak of the velocity distribution, centered around 70 meV for the case of HFIR. In TAS, the amount of aluminum "in the beam" from the monochromator chamber, collimators and other elements is larger than in the case of TOF spectrometers. In particular for the HB3 TAS, another reason for the large background is the recent enlargement of beam tubes to increase the incident flux, when the instrumental shielding has not been upgraded yet.

On the other hand, at MAPS the high flux region extends to higher energies, the detectors and the sample are in the same vacuum space, and consequently the background signal is very low. This is the reason why in the case of the intermediate valence compounds, with its broad features over large energy scales, TOF has shown to be a technique better suited for our purposes.

In terms of monochromatic flux at the sample, today's best choppers (as MAPS) achieve time averaged flux values in the range 10^4-10^5 neutrons cm^{-2} s^{-1} at thermal energies of 50 meV, to be compared with 10^8-10^9 at energies around 35 meV on thermal TAS instrument (IN8) at the Institute Laue-Langevin (ILL), in Grenoble, France[40]. HFIR flux is comparable to the one at ILL, but centered between 60 and 80 meV.

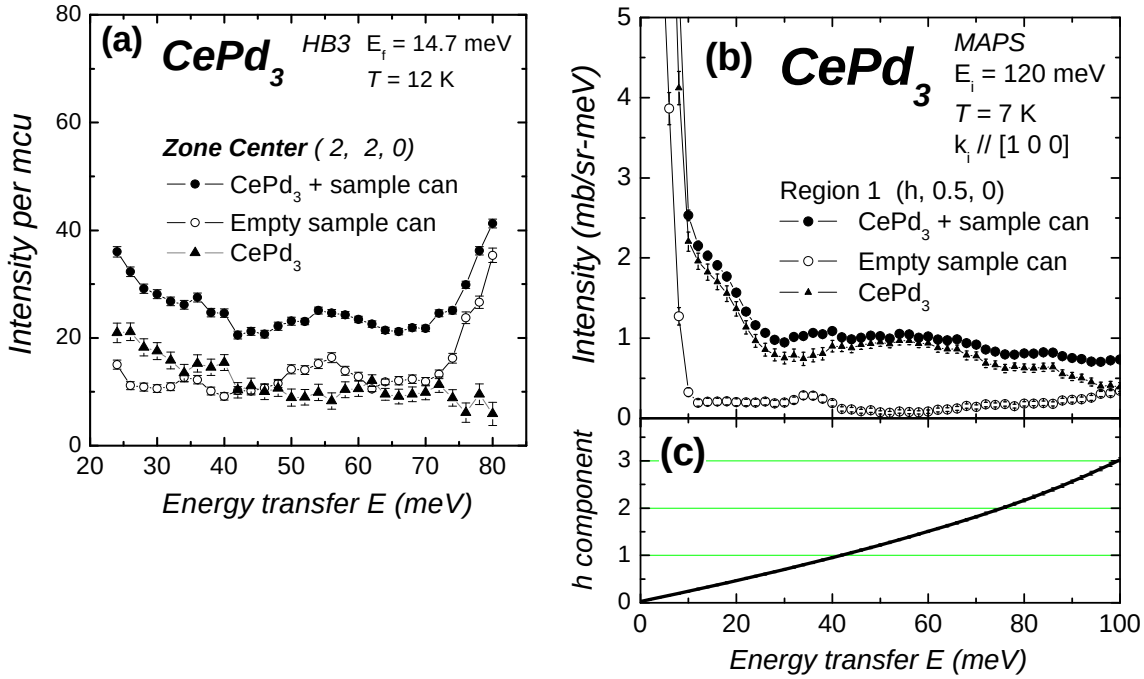

Figure 2.3. Panel (a): TAS raw data for the $CePd_3$ single crystal (close circles), and for the empty sample container (open circles). The $CePd_3$ contribution to the intensity (triangles) is obtained after subtraction of the empty container scattering. These data were measured at 12 K, using neutrons with fixed final energy of 14.7 meV, at constant $\vec{Q}=(2\pi/a_0)(2,2,0)$, with reduced $\vec{q}$ at center in the Brillouin zone. Similarly, panel (b): TOF intensity for $CePd_3$ (close circles), for the empty sample container (open circles), and for the sample (triangles) after subtraction, measured at 7 K, with neutron incident energy of 120 meV at $\vec{Q}=(2\pi/a_0)(h,0.5,0)$, the sample is aligned with its [1, 0, 0] direction parallel with the incoming beam wave vector $\vec{k}_i$. Panel (c): variation of the h-component of $\vec{Q}$ with energy transfer.

2.2.b Experimental Setup

The $CePd_3$ and $LaPd_3$ samples were attached to an aluminum sample holder as shown in figure 2.1, sealed in a thin-walled aluminum can and pumped to prevent oxidation. They were mounted on a closed cycle refrigerator for scans down to 7 K.

Samples were aligned in a TAS. Knowing the sample structure, and several of its Bragg reflections, transverse and longitudinal scans are performed through two or more reflections. Neutron scattering showed that the 18g $CePd_3$ sample was a single crystal, whereas the 10 g $LaPd_3$ sample was in fact a multi-crystal, composed by three main grains aligned within 19 degrees. In the case of $YbAl_3$, four crystals were coaligned with a mosaic of 2.5° to attain a total mass of approximately 5 grams.

TOF experiments were performed on the MAPS spectrometer. The initial energy was fixed at 60 and 120 meV. INS on $CePd_3$ and on $LaPd_3$ was measured at 7 and 300 K, whereas $YbAl_3$ was measured at 6, 100 and 300 K. The scattered intensity was normalized to a vanadium standard, measured under the same conditions, and is given in absolute units: mb sr^{-1} meV^{-1} per "magnetic atom" (b = barn = 10^{-24} cm^2, and sr = stereoradian).

TAS experiments were performed on $CePd_3$ and $LaPd_3$ with fixed final energy of 14.7 meV. Monochromator and analyzer crystals were chosen of pyrolitic graphite PG(002), which have a high reflectivity, giving the best intensity. In the last section of this chapter, some scans performed with Si (111) monochromators were used to correct for the so called $\lambda/2$-reflection contamination. The collimators are used before and after each scattering event, that is, before and after the monochromator and the analyzer. We used

collimators with angular divergence (in minutes of arc) of 48', 60', 60' and 120' respectively. The counting rate is normalized to monitor count units (1 mcu ≈ 1 s).

The intensity scattered from the sample is obtained after the subtraction of the contribution to the scattering from the sample holder and container. These are made from (polycrystalline) aluminum. We performed a direct subtraction between datasets corresponding to two runs under same experimental conditions: same temperature and same energy E_i of the incident neutron beam. One run naturally involved the sample (mounted in the container can) and the other one just an empty sample container.

2.3 Magnetic Scattering versus Non-magnetic Scattering

An important step in interpreting the INS spectra is to separate the non-magnetic contribution correctly. Among the methods to estimate the phononic contribution, most require both low- and high-momentum transfer data [5-7]. We will use a different method based on measuring the scattering intensity of the non-magnetic reference compound.

In an inelastic neutron scattering experiment, on a TOF spectrometer, we collect the scattered intensity from a sample on a bank of position-sensitive detectors. After a time-of-flight data analysis, the scattered intensity is determined on a 4-dimensional configuration space of energy transfer E and the three components of the momentum transfer $\vec{Q} = (2\pi / a_0)(h, k, l)$. Among the different ways to display the data, figure 2.4(a) shows the intensity at 8 K averaged over a relative large region in the reciprocal space $(h, 0.5 < k < 1, -0.5 < l < 0.5)$ as a function of energy transfer, for INS on the IV compound $CePd_3$ and its non-magnetic counterpart $LaPd_3$ measured on the MAPS TOF

spectrometer at ISIS. The energy of the incident neutron beam is 120 meV, with the sample oriented with its [100] direction parallel to the incident beam.

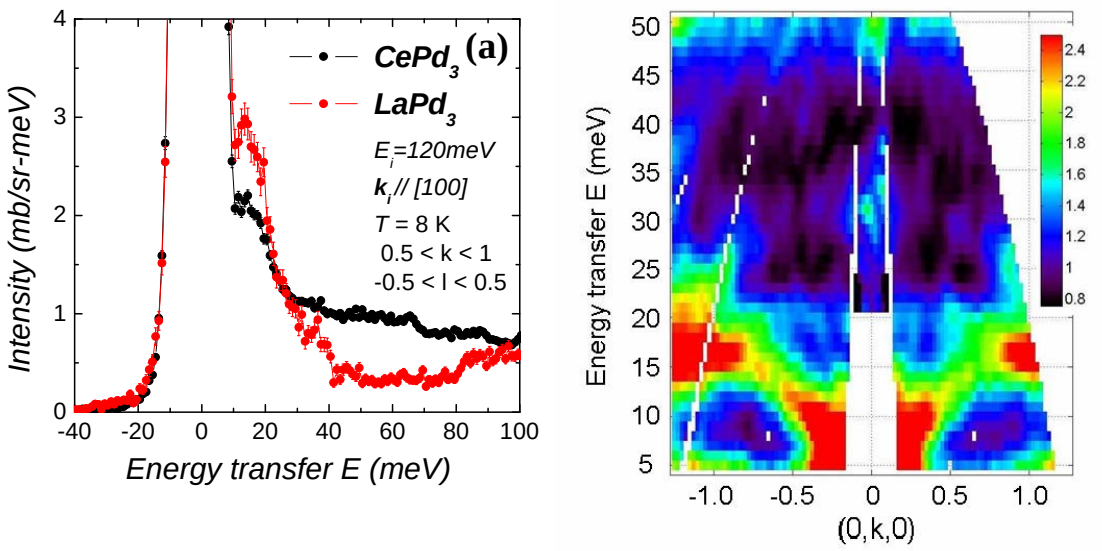

Fig. 2.4: (a) Scattering as a function of energy transfer at 8 K measured on the MAPS spectrometer with 120 meV incident neutrons, from $CePd_3$ (black circles), and from $LaPd_3$ (red circles). This data correspond to a particular region in the reciprocal space: $(h, 0.5 < k < 1, -0.5 < l < 0.5)$. (b) Intensity color plot in the plane (E, k), at 7 K with incident energy of 60 meV, shows the single phonon branches and phonon cut off around 25 meV. The color scale gives the intensity in mb/sr-meV units.

We can identify different contributions to the scattering in this spectrum. Centered around zero-energy transfer is the "elastic peak", which collects the incoherent nuclear scattering. Its full-width at half-height is a measure of the instrumental resolution for the given experimental configuration. In the case of incident neutrons with E_i = 120 meV (Fig. 2.4 (a)), and 60 meV, the resolution is 9.5 meV and 4.7 meV respectively. In the region between 15 and 20 meV, a peak for the single phonon scattering is noticeable for

both compounds. However, between 40 and 80 meV, the scattering of both samples is different. It will be shown that this difference will account for the magnetic scattering of the $CePd_3$ sample.

The single phonon scattering is better resolved with an smaller incident energy, as seen in the color plot of figure 2.4(b), which is taken with an initial energy of 60 meV. This figure displays an intensity plot in the (E, k) plane for $-0.2 < l < 0.2$ at 7 K and it clearly shows acoustic and optic phonon branches at 10 and 20 meV, as well as a phonon cut off around 25 meV. For $E_i = 120$ meV these branches convolute into a single peak.

Another way to show the scattering is through an "energy-slice" over the Q-space. Figure 2.5 shows the distribution of the scattered intensity from $CePd_3$ over the reciprocal space spanned by the detector banks, using the same experimental condition as in the previous figure. The intensity is integrated over an energy transfer range from 60 to 90 meV, and it shows a Q-dependence with variations of 20-25% over the (k, l) plane.

2.3.a Polycrystalline Averaging Approximation

In order to do an initial exploration of the magnetic and non-magnetic contributions to the scattering, independently from the $\vec{Q}$-dependence mentioned in the last paragraph, we will perform a kind of polycrystalline average by integrating the scattered intensity over a large portion of the reciprocal space. In particular we will choose the rectangular region shown in figure 2.5, and explore the $|\vec{Q}|$-dependence only along the [0, k, 0] direction,

and by integrating the intensity over the values of the l component of $\vec{Q}$ between -0.25 and 0.25, the broadest attainable range in the [0 ,0, l] direction..

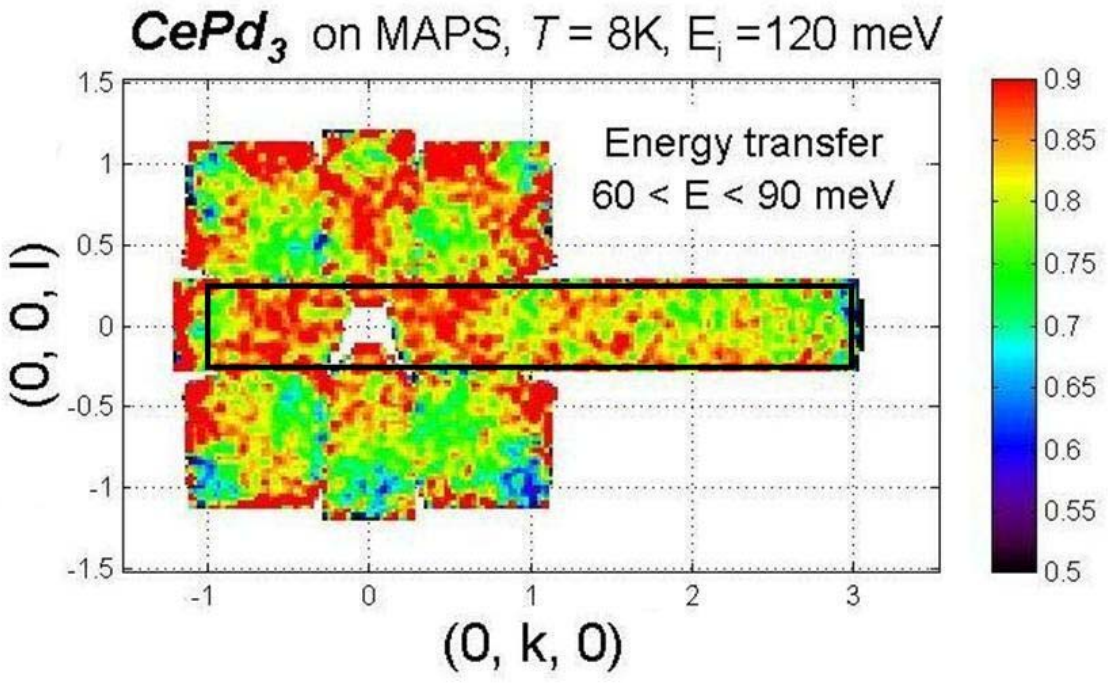

Figure 2.5: Scattering intensity over the (k, l) plane integrated over an energy transfer range from 60 to 90 meV, for neutron scattering data taken on $CePd_3$ at 8 K, measured on MAPS spectrometer with incident neutron energy E_i of 120 meV. The color scale gives the intensity in mb/sr-meV units.

The scattered intensity can be treated as composed by three main contributions:

$$I(Q,\ E) = MS(E) + B(E)\,Q^2 + M(E)\,f^2(Q) \qquad (2.9)$$

where the first two terms correspond to the non-magnetic contribution to the intensity. The multiple and multi-phonon scattering, represented by MS(E) is built up by the addition of the intensity coming from successive single scattering events, like an elastic

scattering followed by a single phonon scattering or two (or more) successive single phonon scattering events (called multi-phonon) . We will assume that MS is Q-independent. This assumption is examined in section 2.4. The term B(E) Q^2 is the single phonon contribution to the scattering with an energy transfer dependent coefficient B(E), and with the only Q-dependence being the Q^2 law coming from the differential cross section for inelastic scattering from single phonons in a cubic single crystal, proportional to the total scattering (coherent plus incoherent) (eqn. 2.4).

The magnetic contribution to the intensity is given by the last term M(E) $f^2(Q)$, where M(E) is the magnetic scattering coefficient, assumed to be Q-independent (section 2.4), and $f^2(Q)$ is the magnetic form factor (introduced with equation 2.7) for the Ce-4f orbital (Ce^{3+})[41]. An acceptable approximation to the Ce^{4f} form factor reported is given by the following equation and plotted in figure 2.6(c).

$$f^2(Q)\Big|_{Ce^{4f}} = e^{\left(-2 \quad 0.03\, Q^{1.7536}\right)} \tag{2.10}$$

An example of the different contributions to the intensity as a function of the momentum transfer is given in the figure 2.6. The intensity (open circles) of the INS of $CePd_3$ at low temperature is plotted as a function of $|\vec{Q}|$, for two energy transfer intervals. In figure 2.6, panel (a), the intensity is mainly of non-magnetic character (MS + B Q^2) in the energy transfer range between 15 to 20 meV, and in panel (b), the magnetic contribution $M\, f^2(Q)$ dominates in the interval 55 to 65 meV.

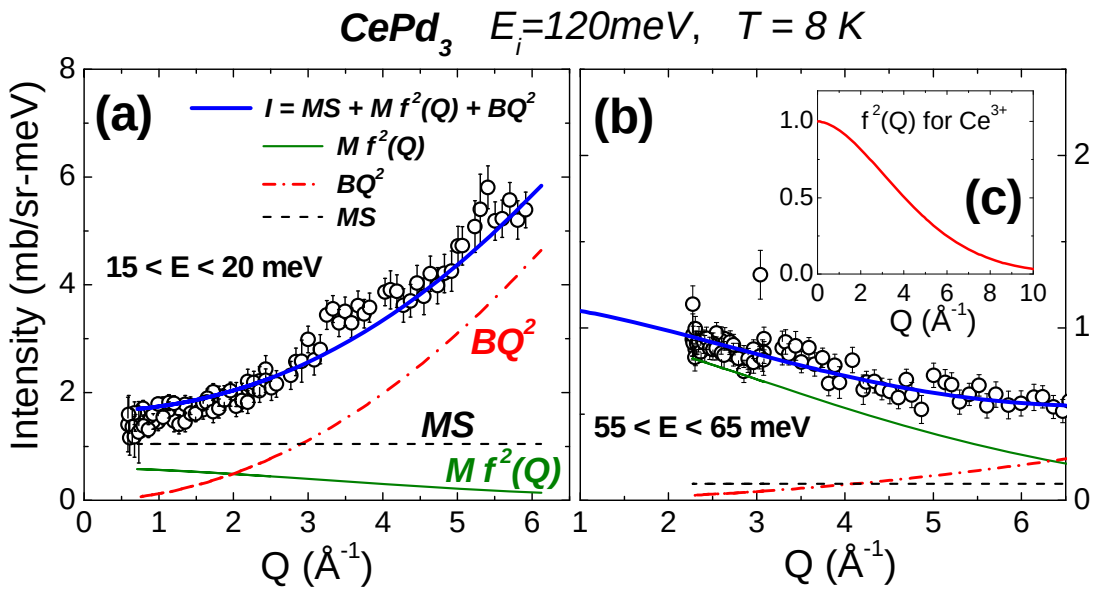

Figure 2.6: Intensity from INS of $CePd_3$ measured on MAPS with E_i=120 meV, at 8 K. In each panel, the data are fitted with the equation 2.9 (blue line). The magnetic (green line), multiple scattering (black line), and single phonon (red line) contributions are also plotted as a function of Q. (a) Energy transfer interval from 15 to 20 meV and (b) 55 to 65 meV. (c) Magnetic form factor for Ce^{4f} as a function of Q.

We assumed in figure 2.6 that the non-magnetic contributions to the scattering for $CePd_3$ can be obtained from the non-magnetic analog compound $LaPd_3$. This is a standard procedure in neutron scattering [42, 43]. A non-magnetic analog was chosen such that it has a lattice structure and lattice dynamics nearly identical to the magnetic compound.

We have proceeded in three steps, as follows. First, we obtained the multiple scattering and single phonon scattering contributions to the scattering from $LaPd_3$ at different values of energy transfer E. Next, we scaled the values of the coefficient B and

MS with a proper factor as discussed further below. Finally, we calculated the magnetic contribution to the scattering by fitting the intensity of $CePd_3$ with all the terms of the equation 2.9. The values for two of the coefficients in equation (2.9) were set equal to the scaled non-magnetic contributions obtained from $LaPd_3$ and the magnetic coefficient M was left as free parameter for the fit.

The low-temperature INS intensity for $LaPd_3$, measured on MAPS with E_i = 120 meV at 7 K, as a function of the modulus of the momentum transfer Q, is shown in figure 2.7, for different energy-transfer ranges. These data were fitted with the multiple scattering and single phonon scattering contributions from equation (2.9), that is: $I = MS + BQ^2$. Only eight of the fifteen energy transfer intervals that were used are displayed in figure 2.7. In each panel, we included the resulting values for the coefficients MS and B.

In this manner, we have obtained MS and B from $LaPd_3$ at different values of energy transfer E. In order to scale the values in a proper manner, we need to consider in which way $CePd_3$ and $LaPd_3$ compounds differ from the point of view of the scattering function. To begin with, these samples have a different number of scattering centers and, from equation 2.3, it is clear that the scattering amplitude for these compounds varies according to the weight given by the scattering length b for each individual atom in the structure factor. Therefore, the scale factor should involve the product of the ratio of the sample masses and the ratio of the different scattering cross sections (proportional to the square of the scattering lengths) for these compounds.

The different sample masses were already taken into account, since the intensity measurement was calibrated with a vanadium standard (section 2.2.b) and it is expressed in absolute units per magnetic atom. With respect to the cross sections, the single phonon

scattering coefficient B and the multiple scattering coefficient MS were assumed to scale as the ratio of the total cross section of $CePd_3$ and $LaPd_3$ respectively. The value for the scale factor is 0.709 (Table 1).

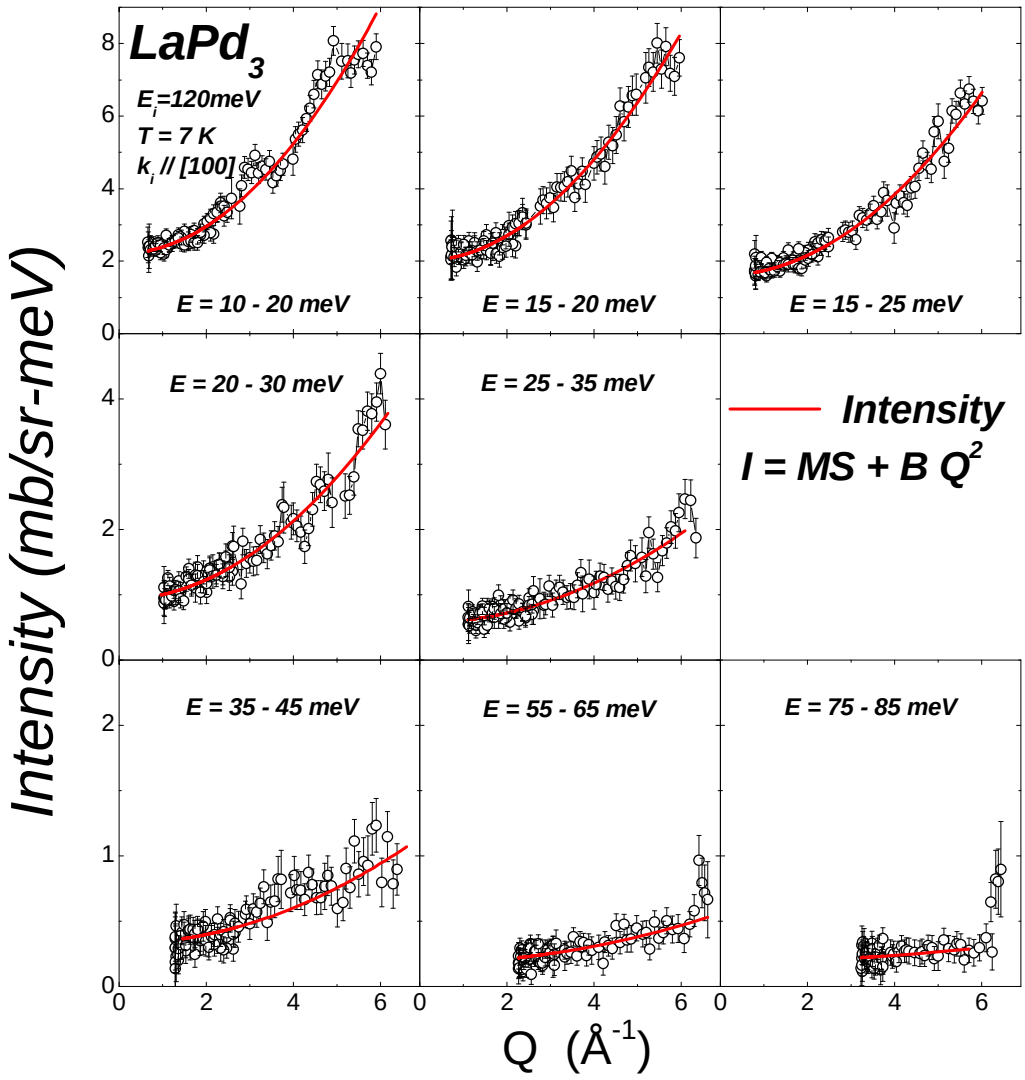

Figure 2.7: INS intensity for $LaPd_3$, measured on MAPS with E_i = 120 meV at 7 K, and fit (using equation 2.9) as a function of the modulus of the momentum transfer Q. Each panel corresponds to a different energy-transfer interval.

Table 1. Neutron scattering cross sections and lengths for La, Ce, Pd, from reference [45], and for the compounds $CePd_3$ and $YbAl_3$.

Cross sections	σ_{coh} (barns)	σ_{inc} (barns)	σ_{scatt}^{total} (barns)	σ_{abs} (barns)	b_{coh} (fm)
La	8.53	1.13	9.66	8.94	8.24
Ce	2.94	0	2.94	0.63	4.84
Pd	4.39	0.093	4.48	6.9	5.91
$LaPd_3$	21.70	1.409	23.10	29.64	25.97
$CePd_3$	16.11	0.279	16.38	21.33	22.57
Ratio ($CePd_3$/$LaPd_3$)	0.742	0.198	0.709	0.720	0.869

In order to obtain the magnetic contribution to the scattering for the $CePd_3$, we have fitted the measured intensity as function of Q with the equation (2.9). The non-magnetic contribution terms were given by fixing the coefficients to the scaled values of MS and B from $LaPd_3$, and the magnetic coefficient M was treated as a free parameter. Figure 2.8 displays the low-temperature INS intensity for $CePd_3$, measured on MAPS with E_i = 120 meV at 8 K, as a function of the modulus of the momentum transfer Q. Each panel shows the data at different energy-transfer ranges and the values for the resulting magnetic scattering coefficient M, as well as the values used for the coefficients MS and B.

From the Q-dependence of the intensity in each energy transfer interval (Fig. 2.8), we can see that the phonon contribution BQ^2 is dominant up to 30 meV, and the magnetic contribution $M(E)f^2(Q)$ is dominant above 45 meV, as expected from the discussion based on figure 2.4(b).

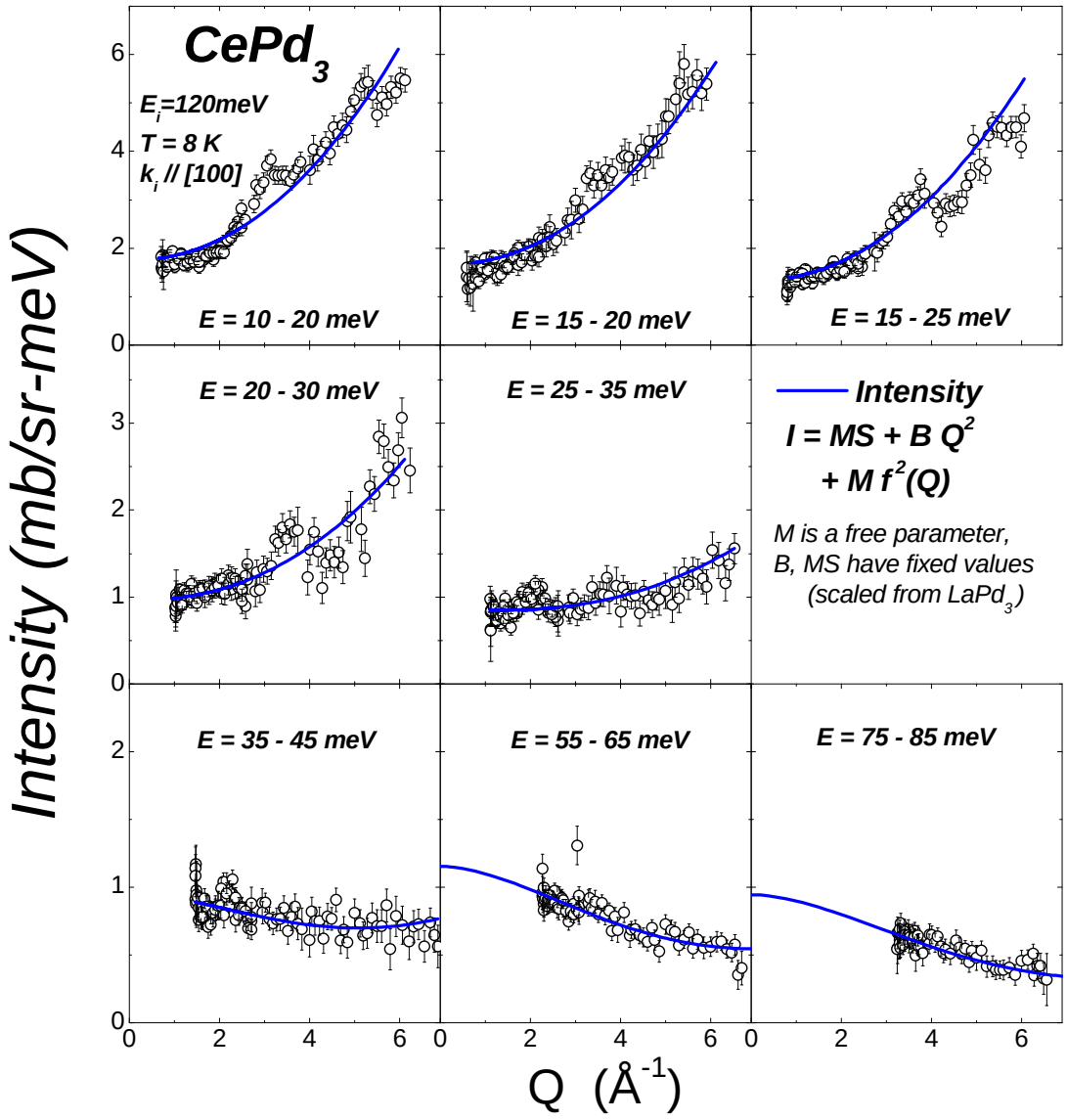

Figure 2.8: INS intensity for $CePd_3$, measured on MAPS with E_i = 120 meV at 8 K, and fit (using equation 2.9) as a function of the modulus of the momentum transfer Q. Each panel corresponds to a different energy-transfer interval.

We have then obtained Q-averaged values for the magnetic and the non-magnetic components of the INS intensity for $CePd_3$. The results for the low-temperature scattering are shown in figure 2.9(a). The magnetic scattering spectrum can be represented by a

Lorentzian lineshape (equation 2.8) with a characteristic energy E_0 of 53 meV, and half width Γ of 27 meV. In addition, we calculated a value for the static magnetic susceptibility χ_{DC} from the amplitude of this magnetic response, as described in reference [44], obtaining a value of 1.3 10^{-3} emu/mol for 8 K.

We have also applied this approximation to the 300 K INS measurements on $CePd_3$ and $LaPd_3$, performed on MAPS with 120 meV incident neutrons. We obtained the Q-averaged magnetic scattering spectrum illustrated in figure 2.9(b). The non-magnetic subtraction below the phonon cut off resulted in a larger uncertainty for the value of the magnetic scattering contribution (note the error bars for energy transfers below 20 meV). The magnetic scattering spectrum has an inelastic Lorentzian lineshape of characteristic energy E_0 of 25 meV, 40% lower than that in the low-temperature regime, and χ_{DC} (1.24 ± 0.09) 10^{-3} emu/mol. If a quasielastic Lorentzian form is used, the calculated value for the static magnetic susceptibility at 300 K would be (1.51 ± 0.09) 10^{-3} emu/mol, closer to the experimental bulk susceptibility value of 1.49 10^{-3} emu/mol (Fig 1.1(d)).

This polycrystalline-averaging method shows that the multiple scattering is in fact a large relative fraction of the non-magnetic scattering, a contribution usually not considered in previous work. We observe an inelastic Kondo-like magnetic scattering with maximum between 50 and 60 meV, the same scale of energy as the Kondo temperature for this compound, around (500 - 600) K [13]. As temperature increases, it evolves towards a quasielastic lorentzian, and the magnetic scattering amplitude is in quantitative agreement with experimental static susceptibility measured in $CePd_3$ (Fig. 1.1).

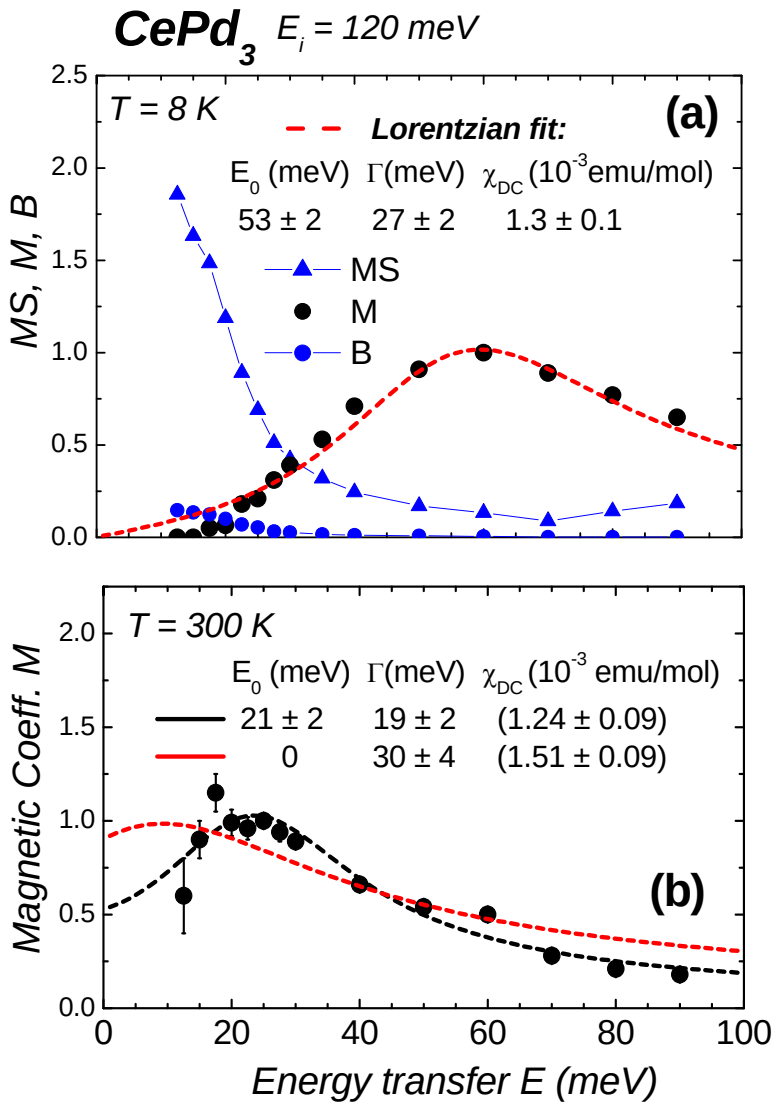

Figure 2.9: Results from the polycrystalline averaging approximation. (a) Results at 8 K for the scaled parameters MS (blue triangles) and B (blue circles) from $LaPd_3$, and the magnetic contribution M obtained for $CePd_3$ (black circles) as function of the energy transfer. A Lorentzian fit is also included. (b) Magnetic contribution coefficient M obtained at 300 K (black circles). Fitting with inelastic (black dashed line) and with quasielastic (red dashed line) Lorentzians are also included.

2.3.b Extending the Non-magnetic Scattering Subtraction Method

The polycrystalline-averaging approximation has proven that the magnetic contribution to the scattering can be obtained in a reliable manner by assuming that the phonon and multiple scattering contributions can be given by the energy spectra of the nonmagnetic counterpart $LaPd_3$ after a proper scaling.

To achieve the purpose of this dissertation, that is, to perform a complete study of the spin dynamics of the intermediate valence compounds as a function of both energy and momentum transfer over the reciprocal space, by neutron scattering experiments, we have applied a similar method when Q is not averaged.

In the analysis of the INS measured on TOF spectrometers to be presented in section 3.1, we will use a single scaling parameter for $LaPd_3$ spectra, with a value of 0.742, which is the ratio of coherent cross sections for $CePd_3$ and $LaPd_3$ (table 1).

For the case of TAS data analysis to be presented in section 3.2, the scaling factor value will come from a combination of the ratio of the sample masses times the ratio of the coherent cross sections, as given by

$$\frac{\text{mass}(CePd_3)}{\text{mass}(LaPd_3)}\frac{\sigma_{\text{coh}}(CePd_3)}{\sigma_{\text{coh}}(LaPd_3)} = \frac{17.72}{10.55}\frac{16.11}{21.70} = 1.247 \qquad (2.11)$$

In contrast to the TOF scattering intensity, in the case of TAS, the intensity is not given in absolute units but it is normalized to monitor counts units, therefore we need to explicitly include the ratio of masses. By inspection we considered that the mass in the neutron beam is the 100% of the sample mass.

To verify the value for the scale factor given in equation (2.11), we compared the areas under the Bragg's peak (2, 0, 0) and (0, 2, 0) for $CePd_3$ and $LaPd_3$, respectively,

measured on HB3 triple-axis spectrometer at 12 K, with fixed final energy of 14.7 meV (Fig. 2.10). The value of the area is proportional both to the mass and the coherent cross section. We calculated the areas by simple integration, obtaining a value of (0.014 ± 0.001) for $CePd_3$ and (0.0077 ± 0.0009) for $LaPd_3$, and a ratio of (1.8 ± 0.1) in the same order of magnitude than the ratio obtained from equation (2.11).

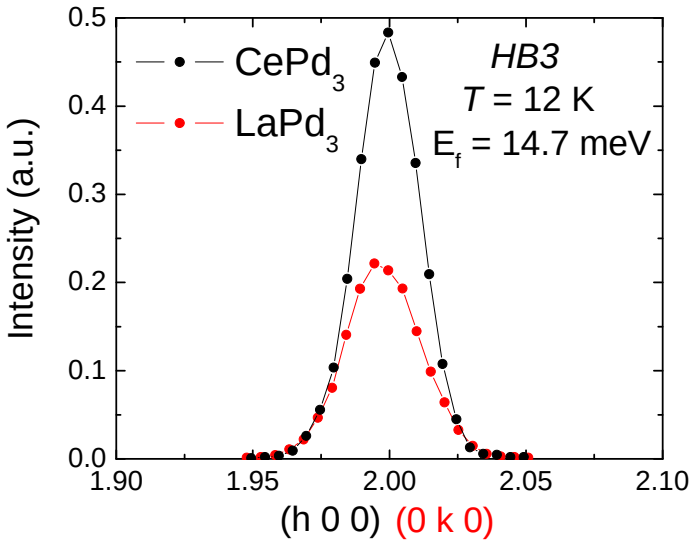

Figure 2.10: Bragg's peaks at (2, 0, 0) and (0, 2, 0) for $CePd_3$ and $LaPd_3$, respectively, measured on HB3 triple-axis spectrometer at 12 K, with fixed final energy of 14.7 meV.

2.4 Verifying the Q-independence of the Multiple Scattering Contribution

In the polycrystalline-averaging approximation (section 2.3.a), the scattered intensity was treated as composed by three main contributions, as seen in equation (2.9). The multiple scattering component (that also includes multi-phonon processes), is assumed to be Q-

independent, that is, it has a magnitude value uniform over different regions in the reciprocal space. This hypothesis is based in the following argument. Let's assume, for instance, a two-scattering event, after the first event, the scattered neutron emerges with a wave vector $\vec{k}'$, whose direction is unknown, then it suffers a second scattering event and is scattered with wave vector $\vec{k}_f$ and collected in a detector of the spectrometer. Since $\vec{k}'$ can have any orientation in 4π, we can say that the transfer momentums for both events ($\vec{Q}_1 = \vec{k}' - \vec{k}_i$ and $\vec{Q}_2 = \vec{k}_f - \vec{k}'$) are averaged over the whole 4π.

We can also verify the Q-independence of MS, by comparing the $LaPd_3$ intensity spectrum over the energy transfer range above the phonon cut-off energy threshold. In figure 2.11, the INS intensity for $LaPd_3$, (scaled by 0.742), is shown for four different regions in Q-space (defined in figure 3.3). For comparison, the spectrum for the $CePd_3$ intensity is also plotted. The difference between the intensity of $CePd_3$ and the scaled intensity of $LaPd_3$, is basically the magnetic scattering from $CePd_3$.

Within error bars, the intensities from $LaPd_3$ are practically equal in the interval from 30 to 100 meV. Region 4 is the only one with higher multiple scattering. Since this difference is small compared with the magnetic component ($CePd_3$ – 0.742 $LaPd_3$), we will neglect this difference, therefore assuming that MS is Q-independent.

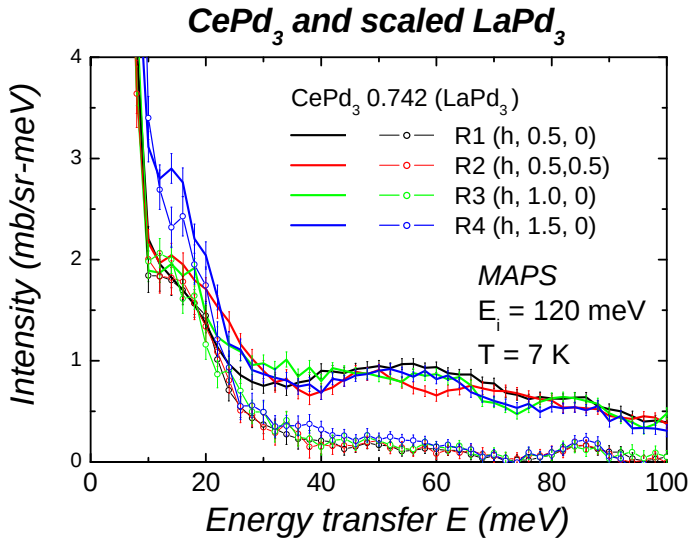

Figure 2.11: INS intensity for $LaPd_3$, (scaled by 0.742), for four different regions in Q-space (defined in figure 3.3) measured on MAPS using E_i = 120 meV, at 7 K. For comparison, the spectrum for the $CePd_3$ intensity is also plotted.

2.5 Spurion Correction

To analyze the scattering from a sample crystal on a TAS, Bragg scattering is used from both the monochromator and the analyzer crystals. High-order wavelength neutrons obeying Bragg's law are also scattered and may result in spurious peaks, called "spurions". The case of neutrons with half the wavelength of those for the n=1 Bragg scattering condition, is called "λ/2 contamination". There are other kinds of spurion processes, including incoherent scattering from the monochromator, or from the analyzer crystal. The spurion contamination is particular for the TAS spectrometer.

Our HB3 experiment was performed with the analyzer at fixed final energy of 14.7 meV condition. When the incident monochromator is set for 58.8 meV (that is, 4 times 14.7 meV), the analyzer will also accept these same 58.8 meV neutrons, which have a wavelength value of λ_f /2 with respect to λ_f. These are incoherent elastically scattered neutrons and they will be incorrectly analyzed as [4(14.7)-14.7] = 44.1 meV inelastically scattered neutrons.

The spurion will not be corrected by subtraction of the scaled $LaPd_3$ spectra that we assumed represents the nonmagnetic contribution to the scattering of $CePd_3$. The reason is that we are using a scaling factor involving the ratio of total scattering cross section of $CePd_3$ and $LaPd_3$ and the ratio of sample masses respectively, whereas the relative spurion contribution to the $CePd_3$ and $LaPd_3$ is related to the ratio of the incoherent cross sections which is more than 3 times greater than the coherent ratio.

In order to identify a potential spurion contribution suspected to appear as an overestimated intensity at 45 meV, we compared the scattering from the non-magnetic counterpart $LaPd_3$ obtained with PG(002) and Si(111) monochromators. With the latter, the intensity is lower, but there is no $\lambda/2$ contamination, and the 45 meV spurion should not be present. Figure 2.12 shows the $LaPd_3$ spectra obtained from constant $\vec{Q}$-scans at $\vec{Q}$ = (2.5, 1.5, 0) and at $\vec{Q}$ = (2, 2, 0) using both monochromators. The data from the Si(111) data has been scaled to match that from PG(002) between 60 and 65 meV. The difference between these spectra is fit with a Gaussian curve. In both scans, the spurion was always centered at 47.5 meV.

Then, the correction of the spurion is made by subtracting from the $LaPd_3$ spectra the Gaussian lineshape obtained in this manner.

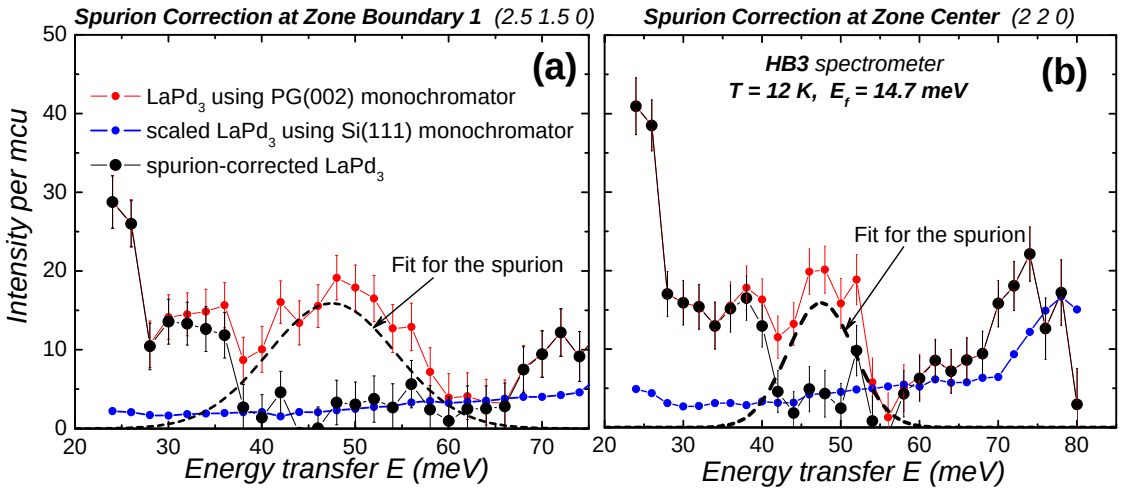

Figure 2.12: $LaPd_3$ spectra obtained from constant $\vec{Q}$-scans measured on HB3 with fixed E_f = 14.7 meV, at 12 K, using a PG(002) monochromator (red symbols) and a Si(111) monochromator (blue symbols). The spectrum measured with the Si(111) monochromator has been scaled to match that from the PG(002) in the interval between 60 and 65 meV. The difference between these spectra is fit with a Gaussian (black dashed line). The spurion-corrected $LaPd_3$ spectra are obtained after subtraction of the Gaussian lineshape. (a) Scans at $\vec{Q}$ = (2.5, 1.5, 0) and (b) scans at $\vec{Q}$ = (2, 2, 0).

Chapter 3

Inelastic Neutron Scattering Studies in $CePd_3$

In this chapter, the results and analysis from a systematic INS study of $CePd_3$ are presented. We will look for the dynamic magnetic response of the system in its different temperature regimes, *i.e.*, in the high temperature local magnetic moment limit and in the low temperature Fermi liquid ground state, emphasizing the Q-dependence of this response.

INS measurement were performed at the pulsed spallation neutron source ISIS of the Rutherford Appleton Laboratory on the time-on-flight chopper spectrometer MAPS and at the High Flux Isotope Reactor at Oak Ridge National Laboratory on the triple-axis spectrometer HB-3. The experiments were done on a single crystalline sample of $CePd_3$ and on a single crystal of the nonmagnetic counterpart $LaPd_3$ under identical conditions.

3.1 Results from the Time-of-flight Spectrometer

Inelastic neutron scattering measurements were performed on the MAPS TOF spectrometer with the experimental setup described in section 2.2.b. The initial energy of the neutrons was fixed at 120 and 60 meV, and the instrumental energy resolution in each case was 4.7 and 9.5 meV respectively.

A significant result from the experiment at MAPS is the distribution of the magnetic contribution to the scattered intensity over momentum transfer space, which is relatively uniform at room temperature, whereas it shows a variation in intensity around 25 and 30% at low temperatures. This Q-dependence at both temperature regimes is illustrated in figure. 3.1, where the intensity maps show the variation of the scattering over the reciprocal space plane spanned by the detector bank. In this figure, the scattered intensity is integrated over the energy transfer range from 50 to 70 meV corresponding to the maximum of the magnetic response of the system observed in the low-temperature regime (Fig. 1.2b). The magnetic and the non-magnetic contributions were not separated from each other on these intensity maps, however, in this energy range, the magnetic response is much larger than the nonmagnetic one as described in section 2.3.a.

In the low-temperature regime (Fig. 3.1a), the intensity has a non-uniform distribution with maxima around the Brillouin zone boundary points $(Q_K, Q_L) = (0, \pm 0.5), (\pm 0.5, 0)$. This is the expected behavior for the Q-dependence of intraband scattering according to the Anderson Lattice model, as explained in section 1.3.b. At 300 K (Fig. 3.1b), a temperature roughly half of the Kondo temperature for $CePd_3$, the intensity is uniformly

distributed over Q. A lack of Q-dependence implies a local character for the spin fluctuation as expected at high temperatures in the limit of uncorrelated local moment behavior.

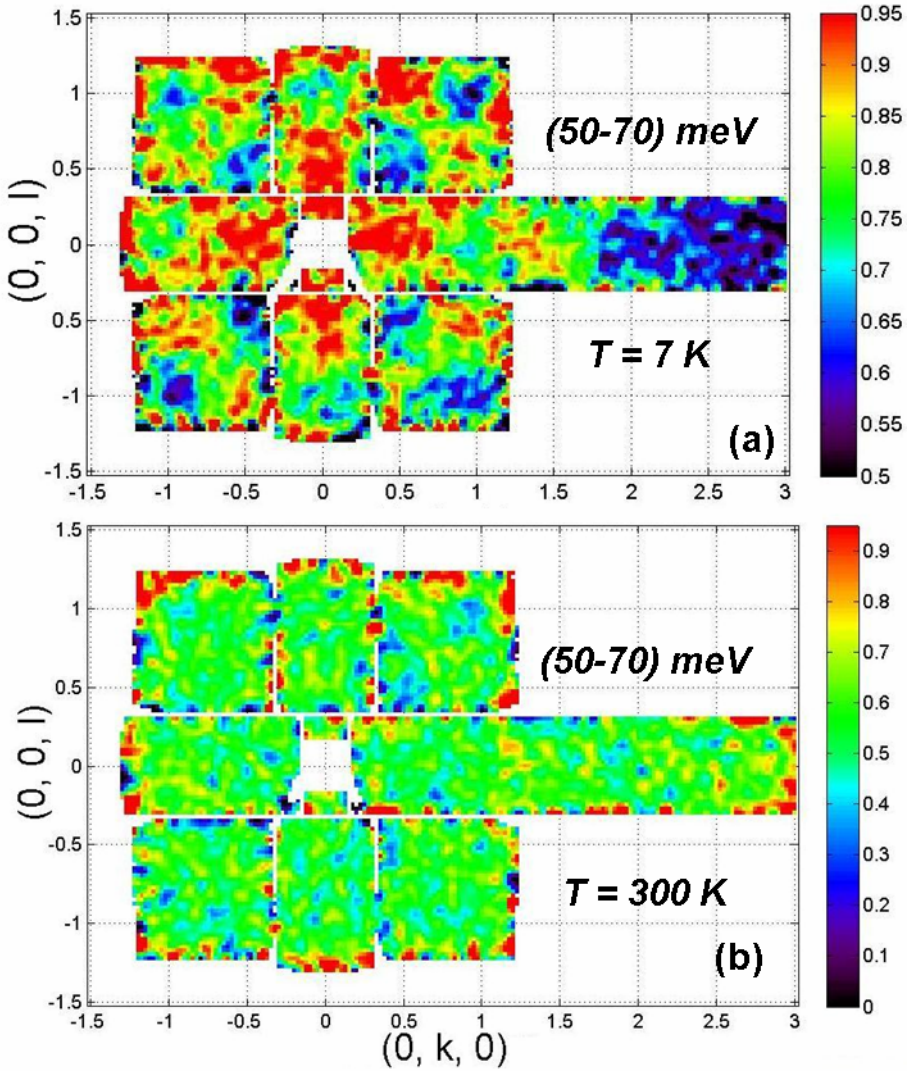

Figure 3.1: Scattering intensity over the (k, l) plane integrated over an energy transfer range of 50 to 70 meV, for neutron scattering data taken on $CePd_3$ at 7 K (a), and at 300 K (b), using MAPS spectrometer with incident neutron energy E_i of 120 meV. The color scale gives the intensity in mb/sr-meV units.

To obtain the magnetic contribution to the scattering, the method explained in section 2.3.a is used. That is, we assume the phonon and multiple scattering contributions in $CePd_3$ are given by the energy spectra of the nonmagnetic counterpart $LaPd_3$ after a proper scaling. In the TOF data analysis, the $LaPd_3$ spectra will be scaled by the factor coming from the ratio of the coherent cross sections as discussed in section 2.3.b. The value for this scaling factor is 0.742 (table 1). Figure 3.2(a) shows how the scaled spectrum from $LaPd_3$ matches the one of $CePd_3$ in the energy transfer range of 10 to 20 meV, over one of the regions in reciprocal space that will be defined below. That the scattering in this energy range corresponds to single-phonon scattering events can be seen from the color plot of figure 2.4(b), which is taken at a smaller incident energy E_i = 60 meV, and hence has better resolution. This figure clearly shows acoustic and optic phonons below 20 meV and the phonon cut off around 25 meV. Given this, the difference between the $CePd_3$ and the scaled $LaPd_3$ scattering should account for the magnetic contribution to the scattering, especially for energy transfer above 25 meV.

The Q-dependence of the magnetic scattering will be studied by comparing four different Q-regions in the plane $(Q_K, Q_L) = (2\pi/a_0)(k, l)$, as illustrated in Figure 3.3. Region 1 (R1), region 2 (R2), region 3 (R3), and region 4 (R4) are centered around (k, l) = (0.5, 0), (0.5, 0.5), (1, 0), and (1.5, 0) respectively. Since the crystal structure of $CePd_3$ is cubic, and under the assumption of isotropic scattering, we will take advantage of the consequent 4-fold symmetry on the plane (Q_K, Q_L) to increase data statistics by adding equivalent regions. This is performed for four equivalent R1 and four equivalent R2 regions. The coordinates in reciprocal space for these Q-regions are given in the table included in figure 3.3.

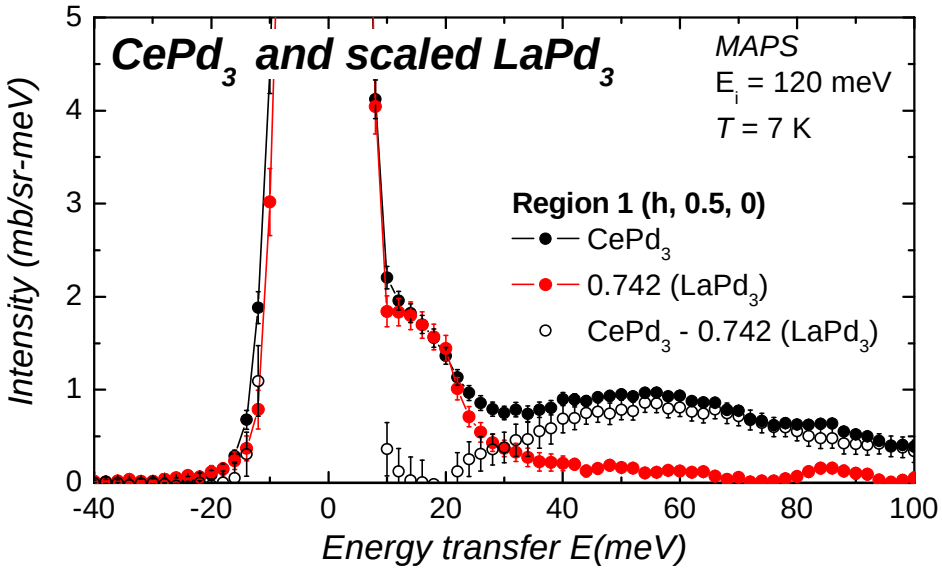

Figure 3.2: Scattering at 7 K with 120 meV incident neutrons from the $CePd_3$ sample (black circles), scaled scattering from $LaPd_3$ (red circles) and the difference (open circles), assumed to represent the magnetic contribution to the scattering. This data correspond to a particular region in the reciprocal space, called Region 1.

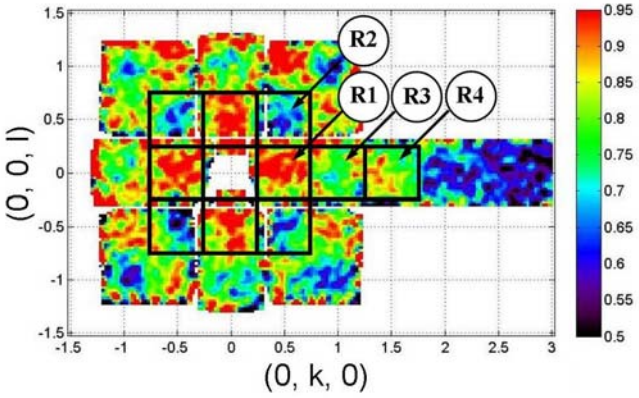

Region	k	l
R1	0.25 to 0.75	-0.25 to 0.25
	-0.25 to 0.25	0.25 to 0.75
	-0.75 to -0.25	-0.25 to 0.25
	-0.25 to 0.25	-0.75 to -0.25
R2	0.25 to 0.75	0.25 to 0.75
	-0.75 to -0.25	0.25 to 0.75
	-0.75 to -0.25	-0.75 to -0.25
	0.25 to 0.75	-0.75 to -0.25
R3	0.75 to 1.25	-0.25 to 0.25
R4	1.25 to 1.75	-0.25 to 0.25

Figure 3.3: Regions on the reciprocal plane (k, l) displayed on an intensity map over a range of 50 to 70 meV, at 7 K with incident neutrons of $E_i = 120$ meV. Boundaries of the regions and their respective equivalent ones are shown in the table.

3.1.a Low-temperature Regime

After the subtraction of the non-magnetic contribution to the scattering, the magnetic contribution $S_{magn}(Q,E)$ over the different regions of the reciprocal plane (Q_K, Q_L) is well represented by a single component with a Lorentzian power spectrum:

$$S_{magn}(Q,E) = \frac{1}{(1-e^{-E/k_B T})} f^2(Q) \frac{E A_L \Gamma}{2\pi} \left(\frac{1}{(E-E_0)^2 + \Gamma^2} + \frac{1}{(E+E_0)^2 + \Gamma^2} \right) \qquad (3.1)$$

where the first factor represents the thermal factor (or detailed balance factor), $f^2(Q)$ is the magnetic form factor, A_L is a constant, Γ is the Lorentzian half-width at half-maximum, and E_0 (the Lorentzian's centroid) is the characteristic energy of the power spectrum. The value of A_L is proportional to the static magnetic susceptibility χ_{DC}. The magnetic contribution of the intensity spectra at the four regions in the reciprocal space is shown in figure 3.4. These results were obtained using the MAPS spectrometer with incident neutrons of 120 meV at 7 K. In TOF measurements, for a fixed sample orientation, momentum transfer and energy transfer are coupled, in other words, only three of the four variables E, h, k, l are independent, as discussed in section 2.2.a. The variation of the h-component of the momentum transfer with energy transfer is also plotted in figure 3.4 for each of the regions in Q-space.

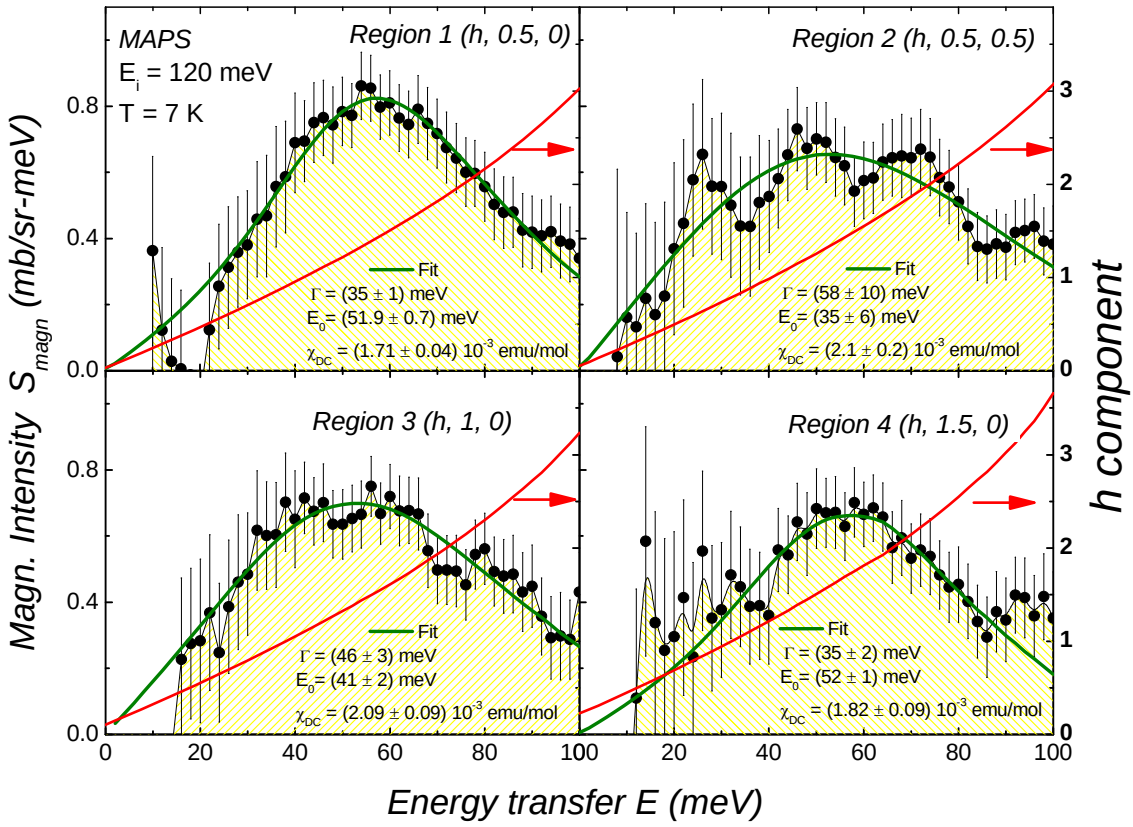

Figure 3.4: Magnetic contribution ($CePd_3$ – 0.742 $LaPd_3$) to the intensity spectra at the four regions in the plane (k, l), from measurements on MAPS at 7 K with incident neutrons of 120 meV. The green lines are fits to an inelastic Lorentzian power spectrum, with parameters shown in the figure and in Table 3.1. The variation of the h component of $\vec{Q}$ with energy transfer (red line) is shown at each region.

The values for the characteristic energy E_0 and the half-width Γ vary over the Q-regions with an average of $E_0 = (45 \pm 2)$ meV and $\Gamma = (43.5 \pm 4)$ meV. After conversion, the average value for the static susceptibility is $\chi_{DC} = (1.93 \pm 0.2)\ 10^{-3}$ emu/mol. The values for these parameters are shown in table 2. Regions 1, 3 and 4 show a reasonable agreement with an inelastic Lorentzian lineshape. However, in regions 2 and 3 (and

probably also in region 4) there is a small but recognizable oscillation of the magnetic component of the intensity mounted on top of the Lorentzian curve, which is of the same nature as the one seen in the intensity color plot of figure 3.1a. In other words, in a spectra at fixed (k, l), the variation of h with energy transfer E can lead to an intensity oscillation with E in a similar way as the color maps at a fixed energy transfer interval ΔE manifest the oscillation in intensity as h or k traverses the reciprocal-space area. In all cases, below energy transfer values of 25-30 meV, the magnetic contribution obtained from the subtraction ($CePd_3$ – 0.742 $LaPd_3$) is less reliable due to the overlap of the magnetic scattering with a strong single phonon contribution.

In figure 3.5(a), the lineshape for the Lorentzians at all regions are overplotted. For the comparison, the magnetic intensity has been normalized by dividing out the magnetic form factor $f^2(Q)$. The highest peaks of the magnetic contribution to the intensity are observed at regions 4 and 1. The values of (h, k, l) at the energy of these peaks, when $\Delta E \approx 60$ meV are (1.8, 1.5, 0) and (1.5, 0.5, 0) respectively. Lower intensity-maxima are observed at regions 2 and 3, with (h, k, l) = (1.5, 0.5, 0.5) and (1.5, 1.0, 0) respectively. The variation of the h component of $\vec{Q}$ is also displayed at all regions in figure 3.5(b).

Summarizing, at low temperatures, the spin dynamics develops a Q-dependence that resembles the threshold interband scattering predicted for the Anderson lattice (section 1.3.b) in the sense that the maximum intensity occurs for momentum transfer Q at zone boundary, connecting regions of large density of states in the hybridized band states of figure 1.6. While the variation of the magnetic contribution is significant enough to be noticeable, it is not at all as drastic as the ALM prediction.

Table 2. Values for the characteristic energy E_0, the half-width Γ, and static susceptibility χ_{DC} for $CePd_3$ over the Q-regions, at 8 K and 300 K, as obtained from the fits shown in figures 3.4 and 3.6(b).

Q–region	T (K)	E_0 (meV)	Γ (meV)	χ_{DC} (10^{-3} emu/mol)
R 1	8	51.9 ± 0.7	35 ± 1	1.71 ± 0.04
R 2		35 ± 6	58 ± 10	2.1 ± 0.2
R 3		41 ± 2	46 ± 3	2.09 ± 0.09
R 4		52 ± 1	35 ± 2	1.82 ± 0.09
Average value		45 ± 2	43.5 ± 4	1.93 ± 0.2
All regions	300	0	26.6 ± 0.7	1.98 ± 0.03

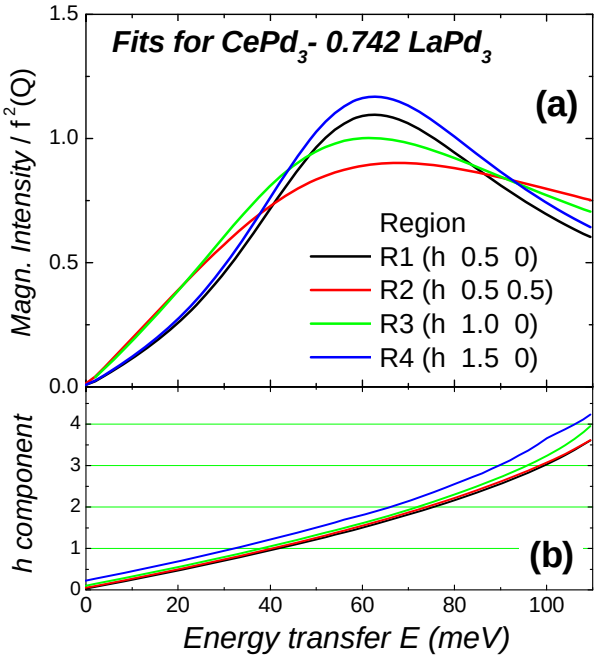

Figure 3.5: (a) Comparison of the magnetic contribution to the scattering at four regions in Q-space, normalized by the magnetic form factor. (b) h-component of momentum transfer $\vec{Q}$ at each region. These results are obtained from measurements on MAPS at 7 K with incident neutrons of 120 meV.

3.1.b High-temperature Regime

The magnetic contribution to the scattering at 300 K is obtained again after subtraction of the non-magnetic contribution assumed to be represented by the $LaPd_3$ intensity scaled by 0.742, as shown in figure 3.6(a). This magnetic response shows a Q-independent quasielastic energy spectrum with the only Q-dependence being in the magnetic form factor $f^2(Q)$. Figure 3.6(b) shows the magnetic part of the intensity normalized by the form factor over the four regions in Q-space, all of which can be fitted simultaneously by a single quasielastic Lorentzian power spectrum whose parameters do not depend on the momentum transfer Q.

In other words, at room temperature, the magnetic response is characteristic of (independent) spatially localized magnetic moments, showing a purely relaxational spin dynamics, as expected from the uncorrelated local magnetic moment limit behavior at high temperatures.

The magnetic contribution is given by:

$$S_{magn}(Q,E) = \frac{1}{(1-e^{-E/k_B T})} f^2(Q) \frac{E A_L}{\pi} \frac{\Gamma}{E^2+\Gamma^2} \qquad (3.2)$$

Therefore, the local moment limit is already achieved at this temperature, roughly 50% of the Kondo temperature, with a Lorentzian half-width Γ of 26.6 meV, or equivalently, 309 K. The value for the static susceptibility χ_{DC} obtained from $S_{magn}(Q,E)$ is 1.98 10^{-3} emu/mol. These values are shown in table 2.

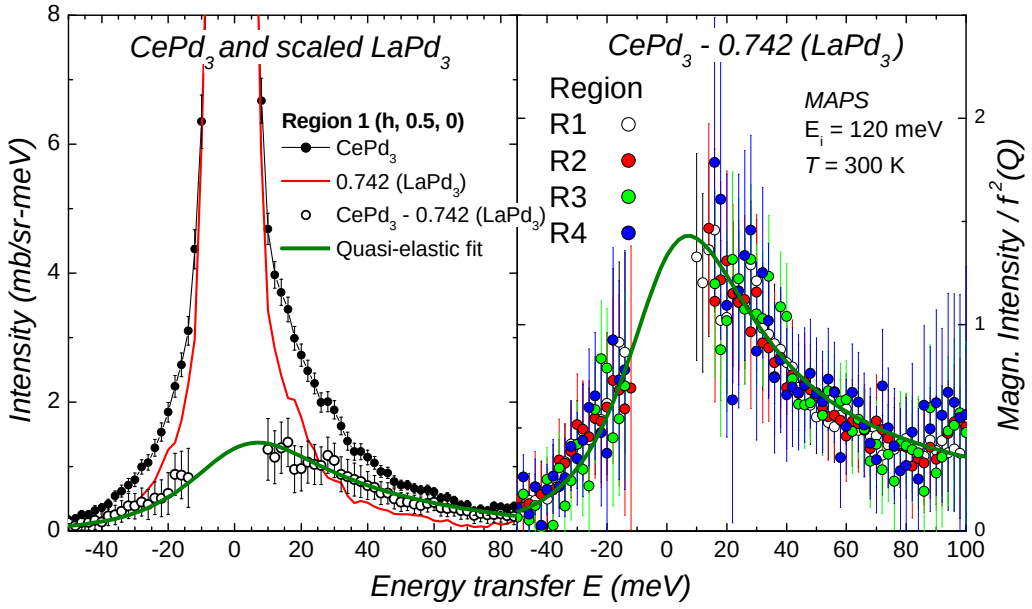

Figure 3.6: (a) Scattering at 300 K, measured on MAPS spectrometer with incident neutrons of 120 meV, from $CePd_3$ (black circles), scaled scattering from $LaPd_3$ (red line) and the difference (open circles), representing the magnetic contribution to the scattering at region 1. The quasielastic Lorentzian fit (green line) is also included. (b) Data for the magnetic contribution normalized by the magnetic form factor at four regions in Q-space and the correspondent quasielastic Lorentzian fit (green line).

3.1.c Static Magnetic Susceptibility

The agreement between the value for the static susceptibility χ_{DC} obtained from $S_{magn}(Q,E)$ and the value obtained from the bulk χ_{DC} measured value is 25%-30% at room temperature. This comparison is shown in figure 3.7, where results from an earlier experiment from Galera *et al.*[46] are also included. In this measurement[46], polarized neutrons were used, a technique that separate magnetic cross sections from all non-magnetic scattering processes. But until recently, the polarization process comes at a

severe loss of flux, with the consequent poor energy- and Q-resolution, and lower statistics. At 7 K, the average value for χ_{DC} obtained from neutrons is (1.93 ± 0.2) 10^{-3} emu/mol. At low temperatures, the contribution to the susceptibility coming from the 4f electrons is of order 1.6 x 10^{-3} emu/mol at T = 0 K. The additional upturn below 50 K arises from a contribution from the 5d electrons, as seen in form factor measurements [47]. In any case, our INS experiments give values for the 4f contribution to the susceptibility of the appropriate magnitude.

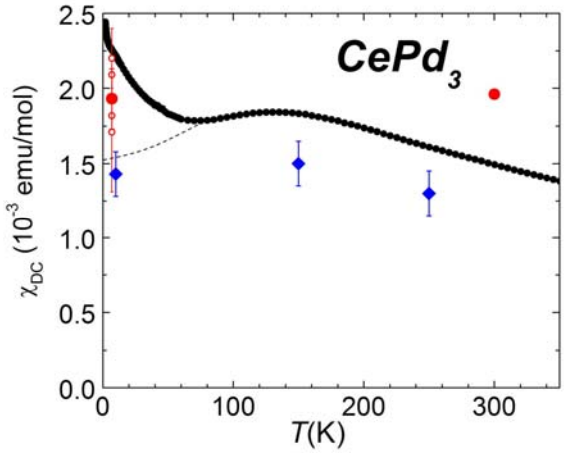

Figure 3.7: Comparison between bulk susceptibility[2] (black circles) and the values deduced from neutron data. Our TOF data are shown as solid red circles; the value at 7 K has been Q-averaged, with the low-temperature values for different regions in Q-space are shown as red open circles; values from Galera *et al*.[46] are shown as blue diamonds. The dashed black line represents the estimate of the 4f contribution to the susceptibility. The additional upturn below 50 K comes from a 5d electronic contribution[47].

3.1.d Alternative Method to Obtain the Non-magnetic Scattering

We have performed INS measurements on $CePd_3$ with an incident energy E_i of 60 meV, at 300 K and 8 K. Since we have not measured $LaPd_3$ at E_i = 60 meV and 300 K, an alternative method to estimate the non-magnetic scattering is by subtracting the quasielastic magnetic Lorentzian obtained from the data taken at room temperature, but using E_i = 120 meV. After performing this subtraction at regions 1 and 2, we obtained three "phonon" peaks near 11, 15 and 21 meV, which showed some dispersion from one Q-region to the other. We fitted these peaks with Gaussian lineshapes as shown in figure 3.8 panels (a) and (b). In this procedure, we assumed that any multiple scattering process present (which in fact, for incident neutrons of 60 meV is lower than that of 120 meV neutrons) is included in this non-magnetic contribution.

To verify the accuracy of this estimation, we scaled down this 3-Gaussian profile from 300 K to 7 K via the temperature dependence of the thermal factor, and compared it with the 0.742-scaled scattering from $LaPd_3$ measured at E_i = 60 meV and 7 K as shown in panels (c) and (d) of figure 3.8. The agreement between these two estimations for the non-magnetic component of the $CePd_3$ scattering spectrum is very good.

We will use this approach in Chapter 4 to determine the non-magnetic scattering for $YbAl_3$, where no nonmagnetic analog scattering was measured.

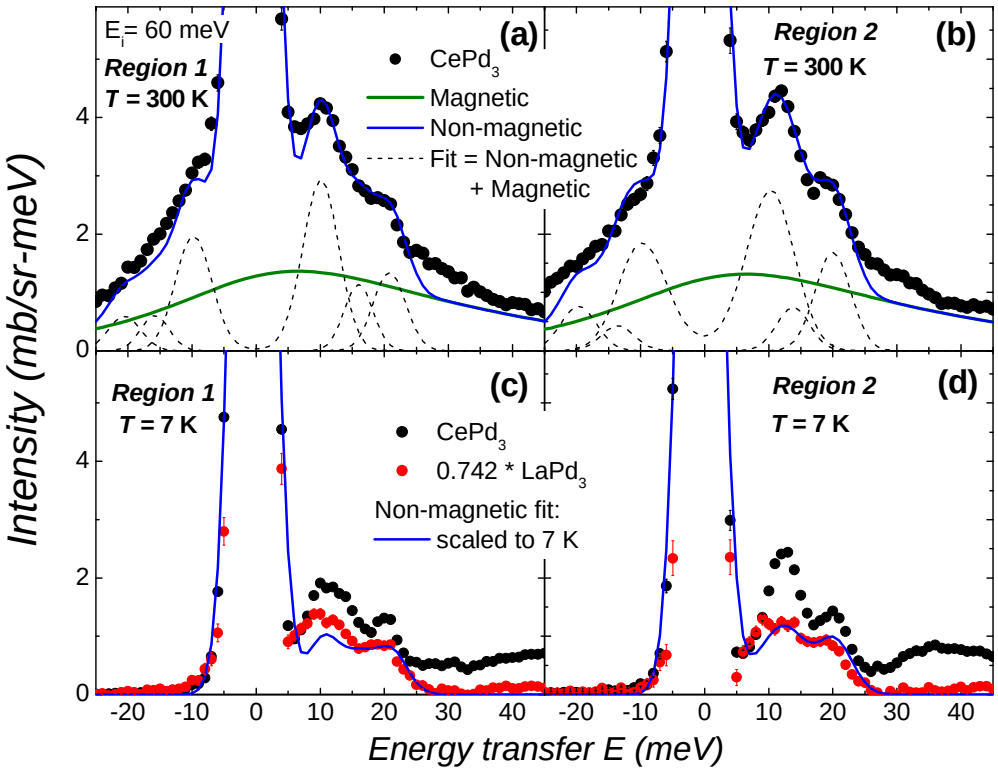

Figure 3.8: Scattering intensity from $CePd_3$ (black circles), measured on MAPS with incident neutrons of 60 meV at 300 K, at region 1 (a) and region 2 (b). The magnetic component is represented by the quasi-elastic Lorentzian (green line) found in section 3.1.b, and the non-magnetic scattering (black dashed lines) is found by fitting (blue line) the total scattering of $CePd_3$. In panels (c) and (d), the non-magnetic scattering found at 300 K is scaled down to 7 K (dashed blue line) to compare with the scaled scattering from $LaPd_3$ (red circles).

3.2 Results from the Triple Axis Spectrometer

We have also measured the spectra at 12 K on the HB3 triple-axis spectrometer, using a fixed final energy E_f of 14.7 meV on both $CePd_3$ and $LaPd_3$ samples. Unlike the case of the TOF spectrometer, triple-axis scans were performed at a fixed momentum transfer $\vec{Q} = (2\pi / a_0)(h, k, l)$. The non-magnetic scattering is assumed to be represented by a fraction of the $LaPd_3$ scattering measured under identical conditions. In section 2.3.b, we found that a proper scale factor to use for TAS data analysis is 1.25 (equation 2.11), a value that takes into account the ratio of sample masses and the ratio of their respective coherent cross sections. In addition, an extra spurion correction was performed on the $LaPd_3$ scattering data. Spurions involve incoherent elastic scattering events of neutrons observed at inelastic energies due to $\lambda/2$ contamination of the final beam. The correction was explained above in section 2.5.

The magnetic contribution to the scattering, obtained after subtraction of the non-magnetic scattering, as well as the intensity from $CePd_3$ and the scaled scattering from $LaPd_3$, are shown in figure 3.9. The intensity is normalized to monitor counts units (1 mcu ≈ 1s). The energy-scans were performed at $\vec{Q} = (2\pi / a_0)(2.5, 1.5, 0)$, that is, at the Brillouin zone boundary and at $\vec{Q} = (2\pi / a_0)(2, 2, 0)$, corresponding to the zone center. While the statistics and background scattering are worse than in the TOF measurement (figure 2.3), the TAS data are in overall good agreement with the TOF data and hence provide confirmation for the basic result. In particular, the magnetic scattering response is 20-25% larger at zone boundary than at zone center, again following the tendency expected from indirect gap transitions in the Anderson Lattice model. Within error bars,

an agreement with the Lorentzian lineshape obtained from the TOF data analysis is achieved between 25 and 65 meV, as shown in figure 3.9. This comparison is not accurate, because the TOF data were not measured at constant Q.

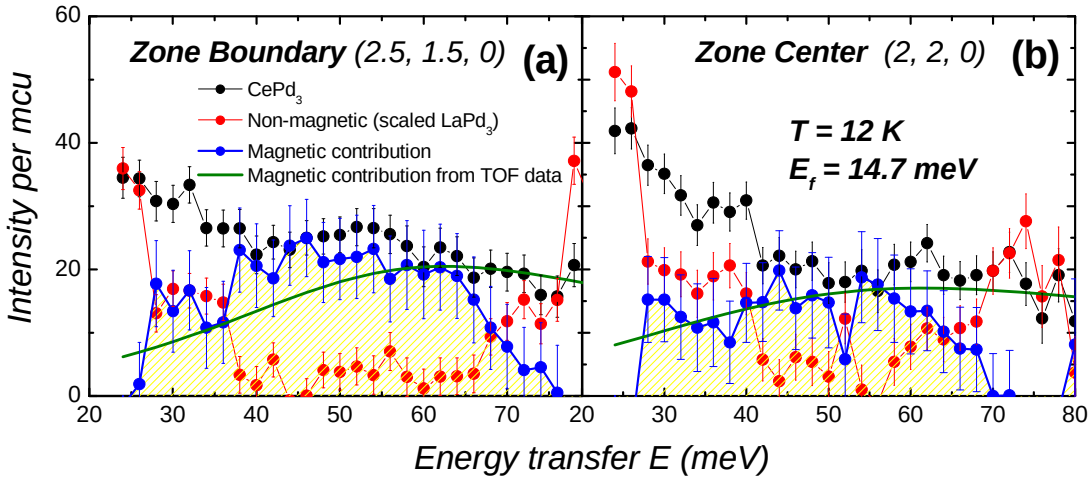

Figure 3.9: Inelastic neutron scattering intensity measured with HB3 triple axis spectrometer at 12 K with fixed final energy of 14.7 meV, for $CePd_3$ (black circles), scaled $LaPd_3$ (red circles), and the difference (blue circles) representing the magnetic contribution to the intensity. The intensity is normalized to monitor counts units (1 mcu ≈ 1s). The magnetic intensity from TOF measurements (green line) is also included for comparison. (a) Energy-scan at the Brillouin zone boundary $\vec{Q}=(2\pi/a_0)(2.5,1.5,0)$, and (b) at the Brillouin zone center $\vec{Q}=(2\pi/a_0)(2,\ 2,0)$.

3.3 Relevance of the Non-magnetic Scattering

Previous measurements on both single- and poly-crystalline samples of $CePd_3$ have also shown a broad, single-ion response centered around $E_0 \approx 55$ meV and $\Gamma \approx 40$ meV [13, 17, 46, 48], at low-temperatures, below 12 K. A controversy exists regarding the details of the $CePd_3$ spin dynamics response. Shapiro *et al.*[14] claimed there were two

components for the magnetic scattering, a quasielastic Lorentzian of width 3 meV and an inelastic one centered at E_0 = 16 meV and with a width of 12 meV at 10 K. In the light of the present measurements where the subtraction of the non-magnetic background has proven to be critical, we think that Shapiro's analysis has certainly ignored this contribution. Since the TAS scan reported by Shapiro was performed close to the Brillouin zone center, at $\vec{Q} = (2\pi / a_0)(0, 0.1, 0.1)$, two facts arise. Firstly, we found that the magnetic contribution at zone center is smaller than at zone boundary and secondly, at 3 meV, an acoustic phonon mode at that value of $\vec{Q}$, is reported by C. K. Loong *et al*. in reference [49]. This probably accounts for the 3 meV narrow quasileastic Lorentzian that was interpreted as one component of the magnetic scattering in reference [14].

A careful determination of the non magnetic scattering helps explaining why Shapiro's results are incorrect. From figures 3.2 and 3.6(a), it is clear that the non-magnetic scattering, assumed to be represented by a scaled fraction of the scattering of $LaPd_3$, constitutes a large fraction of the total scattering, whereas Shapiro *et al*. had assumed a very small and featureless non-magnetic scattering. In figure 3.10, we compare our raw data from $CePd_3$ (black circles), $LaPd_3$ (red triangles) and empty sample holder (open circles) with the constant background (blue dashed line) assumed in the experiment of reference [14]. For the comparison, we used our data from a Brillouin zone center point at 12 K, and the intensity has been scaled to match the $CePd_3$ scattering from both experiments at the energy transfer E = 25 meV. The results from reference [14] have certainly underestimated the non-magnetic contribution to the scattering.

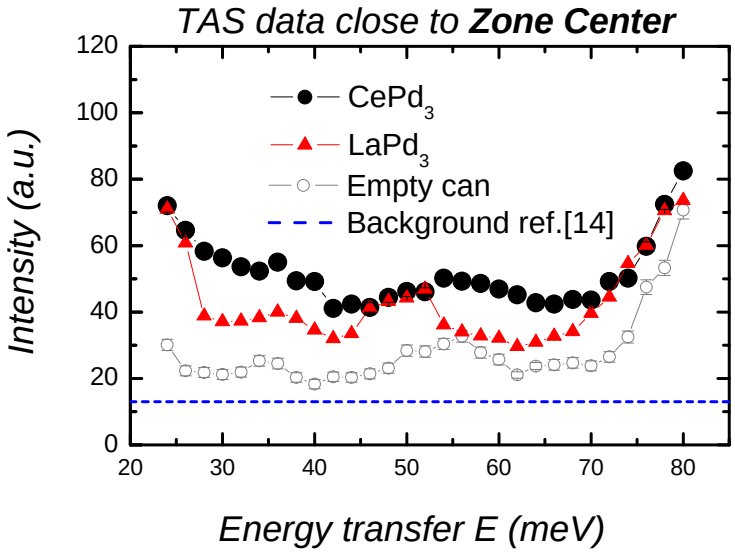

Figure 3.10: Comparison of scattering intensities from our measurements on the TAS HB3, using $E_f = 14.7$ meV, at zone center, and T = 12 K: raw data from $CePd_3$ (black circles), $LaPd_3$ (red triangles) and empty sample holder (open circles). The blue dashed line represents the background scattering assumed in the measurements on $CePd_3$ from reference [14]. The intensity units are arbitrary, chosen such as that at E = 25 meV, the $CePd_3$ intensity from both experiments match.

3.4 Discussion

Our time-of-flight INS experiments on single-crystalline $CePd_3$ have shown essentially a low temperature Kondo-like magnetic response with an inelastic Lorentzian energy spectrum with characteristic energy $E_0 = 45$ meV and a half width of 43.5 meV. The magnetic contribution to the scattering was obtained by considering that the non-magnetic component is represented by a proper scaling of the scattering from the reference compound $LaPd_3$.

In addition the intensity shows a 25-30% variation with momentum transfer, being maximum when $\vec{Q}$ is at the Brillouin zone boundary points (½, ½, 0). This Q-dependence, while consistent with interband scattering across an indirect gap, has not the drastic variation with Q as expected from the Anderson lattice model (section 1.3.b). Measurements on a triple-axis-spectrometer confirm the TOF results, despite the low statistics and the higher background scattering.

At room temperature, the magnetic scattering has a quasielastic Q-independent Lorentzian lineshape, with half width of 26.6 meV, evidencing a spin dynamics of local character. The expected high-temperature local moment regime from the Anderson impurity model, is setting in at a temperature scale of 50% of T_K.

Chapter 4

Inelastic Neutron Scattering studies in $YbAl_3$

In this chapter, the results and analysis for the dynamic magnetic response of $YbAl_3$, obtained from INS experiments are presented. These measurements were performed at 6, 100 and 300 K on MAPS time-of-flight spectrometer at the pulsed spallation neutron source ISIS of the Rutherford Appleton Laboratory, using incident energies of 60 and 120 meV. Four single crystals of total mass approximately of 5 g were coaligned with a mosaic of 2.5°, and oriented with the [1 ,0 ,0] direction parallel to the wave vector $\vec{k}_i$ of the incident beam. In the case of $YbAl_3$, we have not measured a nonmagnetic counterpart compound[1]. In order to separate the magnetic contribution to the scattering we have followed a procedure based on temperature scaling of the nonmagnetic scattering obtained at room temperature. This procedure was shown to give reasonable results for $CePd_3$, as shown in section 3.1.d.

[1] $LuAl_3$, is not a reliable non-magnetic counterpart because of the large absorption cross section of lutetium, associated with a resonance at 140 meV.

4.1 High-temperature Regime

As a first step, we fit the room temperature spectrum taken with $E_i = 60$ meV and for four different regions in the (Q_K,Q_L) plane with a combination of a Lorentzian quasielastic magnetic component and a nonmagnetic part modeled by three Gaussian-like phonon peaks. We have assumed that the multiple scattering is contained in the 3-peaks lineshape and that the empty sample holder contribution is negligible. The result shows a Q-independent quasielastic Lorentzian (as the one in equation 3.2) for the magnetic scattering with half width $\Gamma = (35.3 \pm 1)$ meV and with an amplitude corresponding to $\chi_{DC} = (4.49 \pm 0.04)\ 10^{-3}$ emu/mol, in good agreement with previous results[44]. The only Q-dependence in the magnetic response is given by the magnetic form factor. These results are shown in figure 4.1. The four regions in the reciprocal plane $(Q_K, Q_L) = (2\pi/a_0)(k, l)$, are illustrated in figure 4.2. Region 1 (R1), region 2 (R2), region 3 (R3), and region 4 (R4) are centered around (k, l) = (0.25, 0), (0.5, 0), (0.25, 0.25), and (0.5, 0.5) respectively. Since the crystal structure of $YbAl_3$ is cubic, and under the assumption of isotropic scattering, we will take advantage of the consequent 4-fold symmetry on the plane (k, l) to increase data statistics by adding equivalent regions. The coordinates in reciprocal space for these regions are given in the table in figure 4.2.

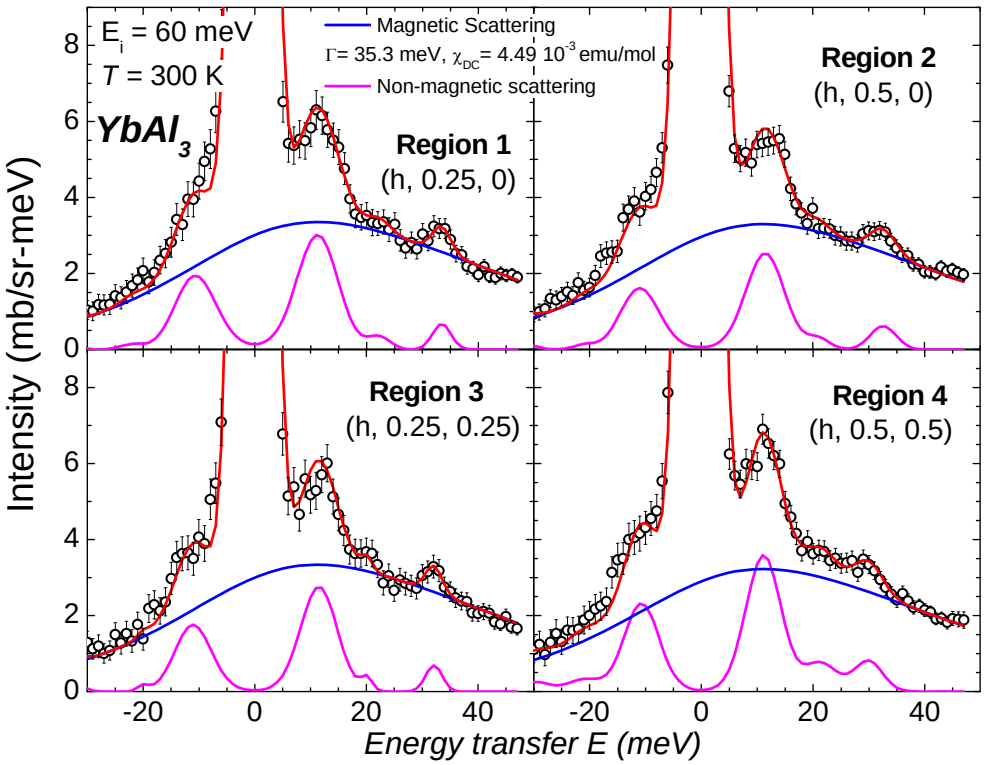

Figure 4.1: INS from $YbAl_3$ (open circles) measured on MAPS with incident energy of 60 meV, at 300 K at the four regions. The non-magnetic scattering is given by three Gaussian-like peaks (magenta line), and the Q-independent magnetic scattering (blue line) by a quasi-elastic Lorentzian of width Γ = 35.3 meV, and amplitude correspondent to a static susceptibility of 4.49 10^{-3} emu/mol. The addition of the magnetic and non-magnetic contributions (red line) matches the experimental data.

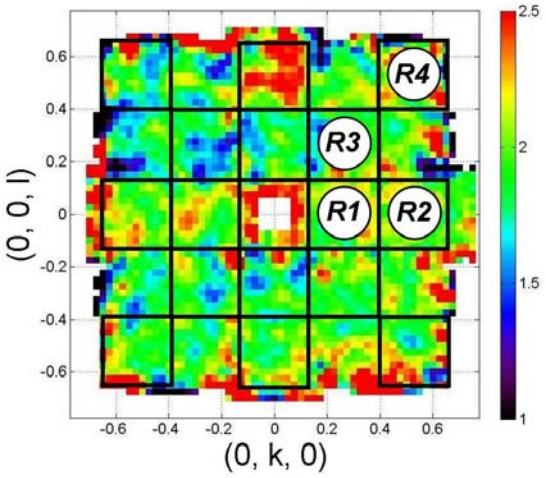

Region	k	l
R1	0.125 to 0.375	-0.125 to 0.125
R2	0.375 to 0.625	-0.125 to 0.125
R3	0.125 to 0.375	0.125 to 0.375
R4	0.375 to 0.625	0.375 to 0.625

Figure 4.2: Regions on the reciprocal plane (k, l), displayed on an intensity map over a range of 40 to 50 meV, at 300 K with incident neutrons of E_i = 60 meV. Boundaries of the regions are shown in the table.

In the second step, we assume that both single-phonon and multiple scattering components vary with temperature as the thermal factor. To obtain the non-magnetic scattering from the data taken at 100 K with $E_i = 60$ meV, we scale down in temperature the values for the Gaussian-like non-magnetic scattering obtained at 300 K. After subtraction of the temperature-scaled non-magnetic contribution, we obtain a single inelastic Lorentzian (as the one in equation 3.1) to represent the magnetic part of the scattering in the four Q-regions, as shown in figure 4.3. The parameters of the Lorentzian are Q-independent: a half width Γ of 32 meV, characteristic energy E_0 of 23 meV and amplitude corresponding to a static magnetic susceptibility χ_{DC} of 5.13 10^{-3} emu/mol.

Next, for the E_i = 120 meV data, we obtain a complete representation of the nonmagnetic scattering at 100 K over a transfer energy range up to 100 meV by subtracting the Lorentzian magnetic response, as determined from the $E_i = 60$ meV data at 100 K, from the $E_i = 120$ meV data. The magnetic form factor is recalculated, because $\vec{Q}$ has different values for a given E when using incident neutrons of 60 or 120 meV. The resulting non-magnetic contribution for the four regions in Q-space is displayed in figure 4.4 (black dashed line). As a consistency check, it is in relative good agreement with the non-magnetic scattering from $E_i = 60$ meV, scaled down from 300 K to 100 K (magenta line).

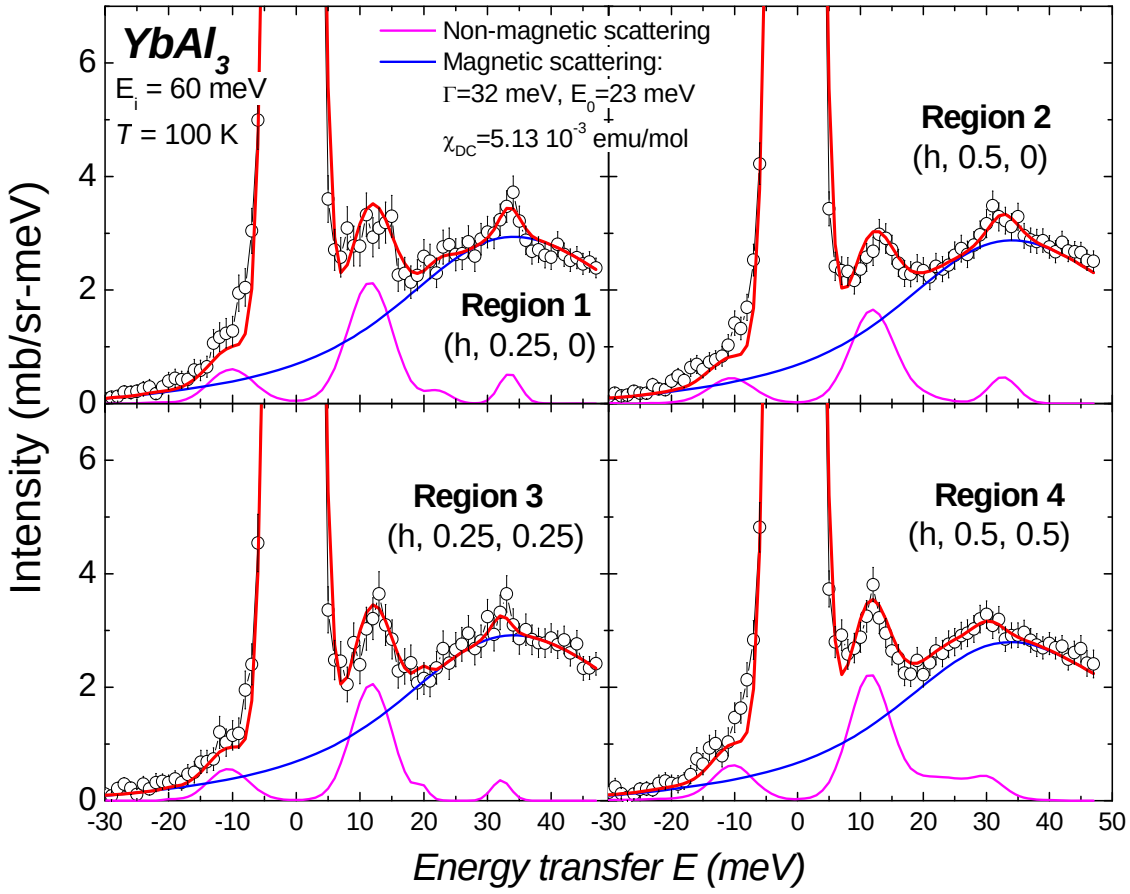

Figure 4.3: INS from $YbAl_3$ (open circles) measured on MAPS with incident energy of 60 meV, at 100 K at the four regions. Using the non-magnetic scattering scaled from 300 K down to 100 K (magenta line), we find a Q-independent inelastic Lorentzian (blue line) with width Γ = 32 meV, characteristic energy E_0 = 23 meV and amplitude correspondent to a static susceptibility of 5.13 10^{-3} emu/mol. The addition of the magnetic and non-magnetic contributions (red line) matches the experimental data.

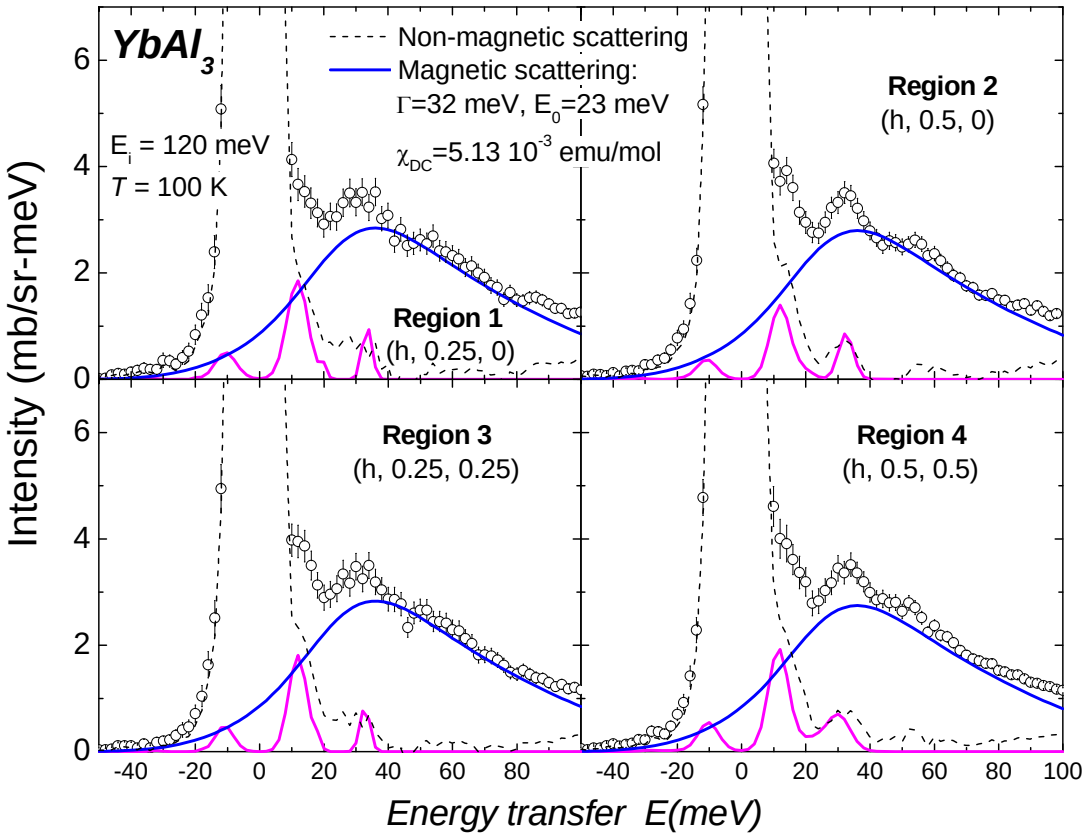

Figure 4.4: INS from $YbAl_3$ (open circles) measured on MAPS with incident energy of 120 meV, at 100 K at the four regions. Subtraction of the inelastic Lorentzian obtained at E_i = 60 meV, 100 K (blue line) from the neutron spectra measured at E_i = 120 meV, 100 K. The difference (black dashed line) should account for the nonmagnetic contribution to the scattering at this temperature. For comparison, the non-magnetic scattering obtained with E_i = 60 meV, scaled from 300 K down to 100 K (magenta line) is also plotted.

4.2 Low-temperature Regime

Finally, we scale the non-magnetic contribution obtained from 100 K down to 6 K by means of the thermal factor and subtract it from the neutron scattering data measured at 6 K, with E_i = 120 meV. As a result, we obtain the magnetic component of the scattering in the low-temperature regime. We have performed this subtraction with 6K-spectra at both

E_i = 60 and 120 meV, with good consistency between the results for the low-temperature magnetic response. This component of the scattering has two inelastic Lorentzian-like components, in agreement with earlier results reported for polycrystalline $YbAl_3$ [44, 50], and in our earlier results on these single crystals[11]. One of them is a narrow peak centered around E_0 = (33.2 ± 0.3) meV in all Q-regions, with an average half width Γ of (6.4 ± 0.6) meV as obtained from the 120 meV data (with energy resolution 9.5 meV), as illustrated in figure 4.5 and E_0 and Γ values of (32.9 ± 0.3) and (4.4 ± 0.3) meV from the 60 meV data (resolution 4.7 meV), as shown in figure 4.6. This peak may be resolution limited, and hence inherently narrower than 4.3 meV. The second magnetic component, a broad peak centered around 50 meV, has characteristic energy E_0 and half width Γ varying over the Q-regions with average values of E_0 = (44.0 ± 0.5) meV and Γ = (32 ± 1) meV respectively. The values for the parameters of the magnetic response of $YbAl_3$ are shown in table 3.

Table 3. Parameters for the magnetic scattering component of $YbAl_3$. Characteristic energy E_0, half-width Γ, and static susceptibility χ_{DC} over the Q regions, at 6 K, 100 K and 300 K. Low-temperature results given for E_i = 120 meV and (*) for E_i = 60 meV.

Q–region	T (K)	Magnetic component #1		Magnetic component #2		χ_{DC} (10^{-3} emu/mol)
		E_0 (meV)	Γ (meV)	E_0 (meV)	Γ (meV)	
R1	6	43.5	31.6	33.0	5.9	4.72
R2		44.2	34.2	33.0	7.1	4.79
R3		43.8	32.5	33.4	5.9	4.74
R4		44.7	30.9	33.5	6.8	4.84
Average value		44.0 ± 0.5	32 ± 1	33.2 ± 0.3 32.9 ± 0.3*	6.4 ± 0.6 4.4 ± 0.3*	4.77 ± 0.05
All regions	100	23	32 ± 1			5.13 ± 0.05
All regions	300	0	35 ± 1			4.49 ± 0.04

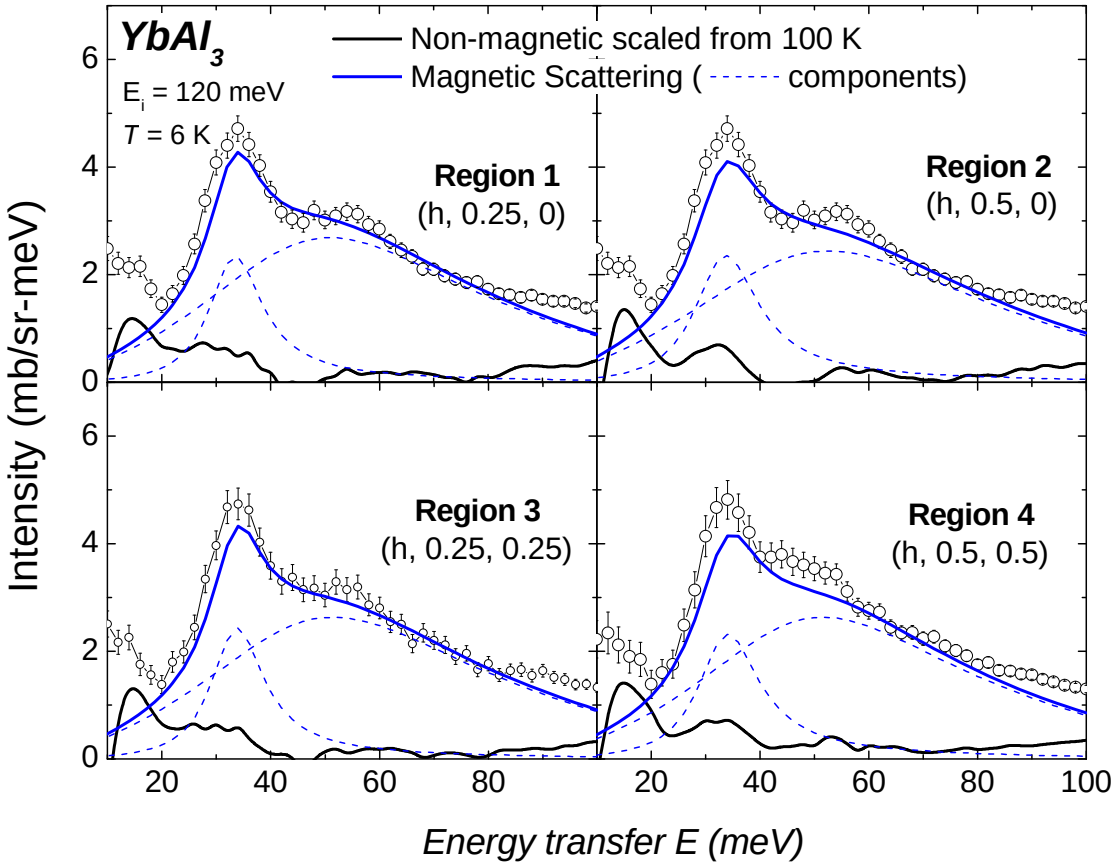

Figure 4.5: INS from $YbAl_3$ (open circles) measured on MAPS with incident energy of 120 meV, at 6 K at the four regions. Using the non-magnetic scattering scaled from 100 K down to 6 K (black line), we find a magnetic scattering (blue line) composed by two inelastic Lorentzian components (dashed blue lines), with characteristic energy E_0 of 33 and 44 meV and half width Γ of 6.4 and 32 meV respectively.

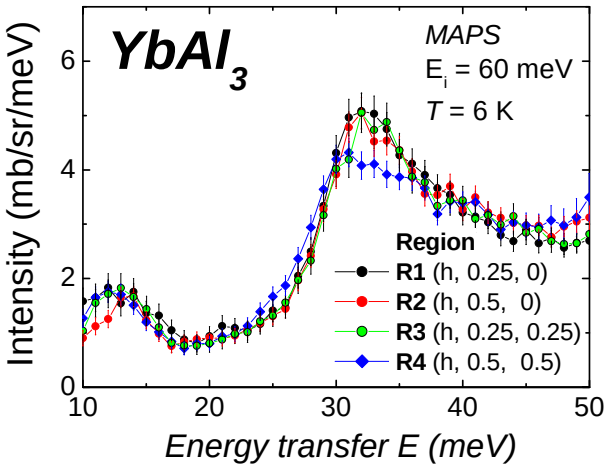

Figure 4.6: INS from $YbAl_3$ (MAPS, incident energy of 60 meV), at 6 K at the four regions. The magnetic excitation has a characteristic energy E_0 of 32.9 meV and a half width Γ of 4.4 meV. The width is basically equal to the instrumental resolution.

To illustrate the Q-dependence of this magnetic response, figure 4.7(a) displays an intensity color plot in the E versus k plane for $-0.2 < l < 0.2$ at $T = 6$ K. In the energy transfer range between 28 and 38 meV, the scattering component centered around 33 meV is essentially independent of $\vec{Q}$. On the other hand, the component centered around 44 meV, shows a Q-dependence, being maximum at the zone boundary where k = 0.5, as seen from the color variation in the range between 40 to 55 meV. Figure 4.7(b) shows the magnetic scattering spectra normalized by the magnetic form factor at 6 K for the different regions in Q-space. All the regions have basically the same 33 meV peak, whereas the 44 meV peak has the largest intensity at region R3, the one closest to a zone boundary point. A new region, R5, centered around (k, l) = (1, 0) thus being the closest to the Brillouin zone center, is also included and shows a lower magnetic response around 45 meV. The intensity maps of figures 4.7(c) and 4.7(d) correspond to intervals of energy transfer of (32.5 ± 2.5) meV and (50 ± 5) meV, respectively and show, in a similar

manner, both the relative uniform intensity of the narrow magnetic component as well as the enhancement of the intensity of the broad magnetic component at (0.5, 0.5) points.

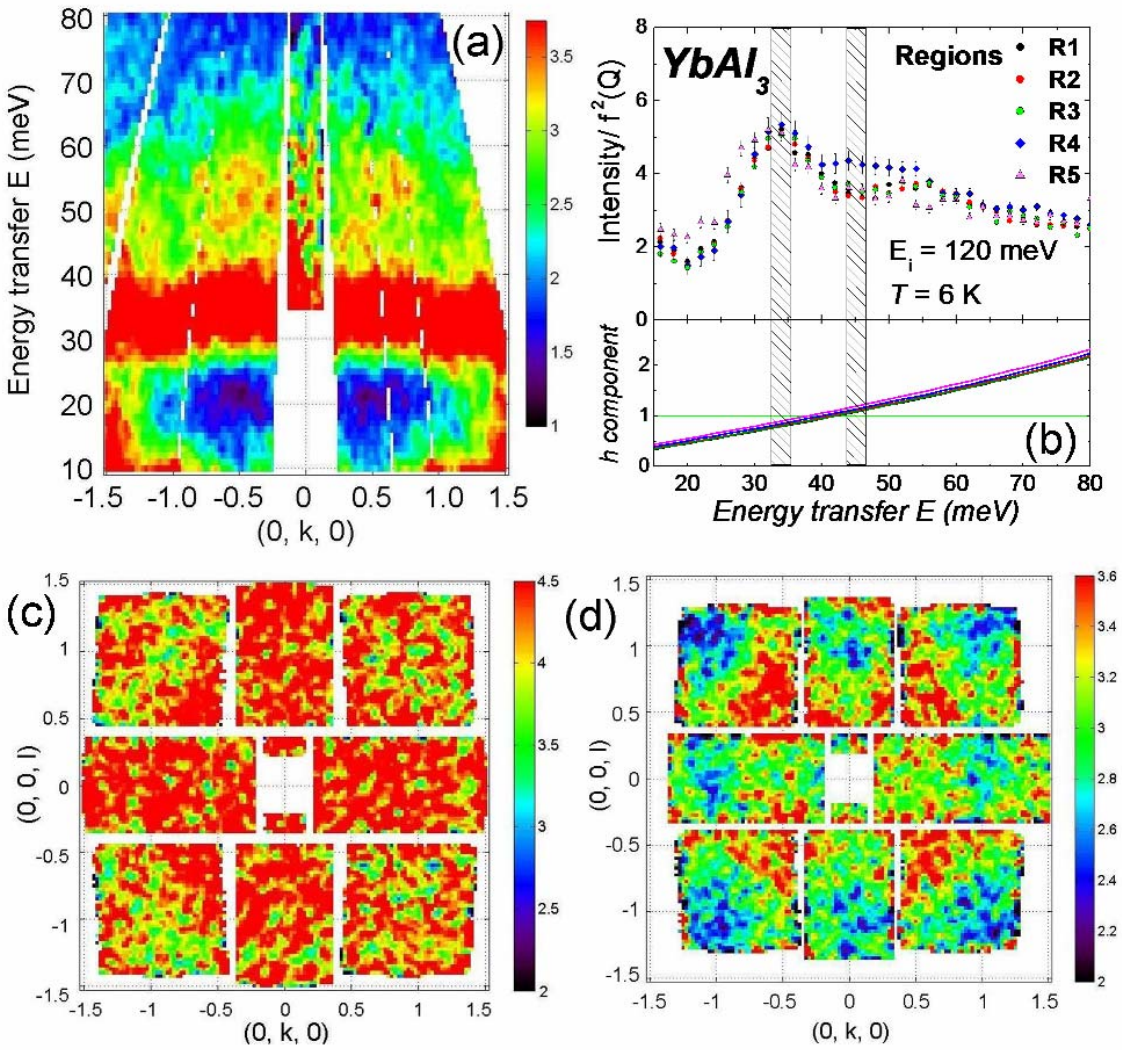

Figure 4.7: INS on $YbAl_3$ measured on MAPS with E_i =120 meV at T = 6 K. (a) Intensity color plot in the E versus k plane for -0.2 < l < 0.2. (b) Magnetic component of the scattering spectra normalized by the magnetic form factor for the different regions in Q-space. The position in energy transfer of the two magnetic components is indicated by the grey shadings. The coordinates (k, l) for regions 1 to 4 are given in figure 4.2, and the region R5 has (k, l) = (1, 0). The h component for these regions is plotted in the lower panel, in units of $(2\pi/a_0)$ versus energy transfer. Intensity maps versus (k, l) for energy transfer in the range (c) 30 to 35 meV and (d) 45 to 55 meV.

There is an excellent agreement between the value for the static susceptibility χ_{DC} obtained from $S_{magn}(Q,E)$ and the value obtained from the bulk χ_{DC}[1], as shown in figure 4.8, where we compare our results with the bulk experimental measurements and with the NCA calculations from reference [1]. The estimated values for the static susceptibility χ_{DC} are shown in table 3.

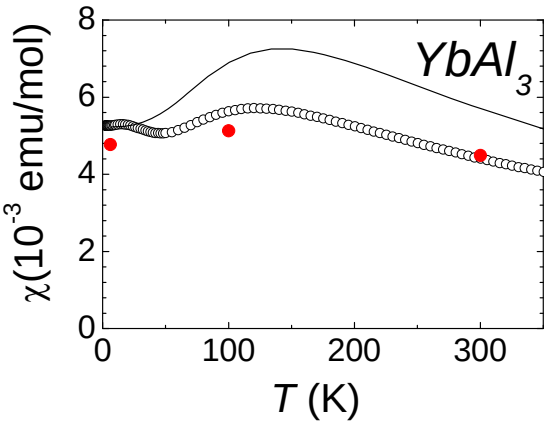

Figure 4.8: Comparison between bulk susceptibility[1] (open circles) and the values deduced from neutron data for $YbAl_3$ (solid red circles). The results of the NCA calculation (black line) from reference [1] are also included.

4.3 Discussion

Our INS experiments on single-crystalline $YbAl_3$ have shown that a broad magnetic scattering with a half width of the order of 32 meV, evolves from a quasielastic Q-independent Lorentzian lineshape at 300 K, characteristic of a high-temperature local moment regime towards an inelastic Lorentzian form as the temperature decreases. At 100 K, the magnetic scattering has an inelastic power spectrum, centered at 23 meV and

with a width of 32 meV. This spectrum is Q-independent. At 6 K, the characteristic energy of this response has a value of 44 meV, in correspondence to the Kondo energy scale of this compound. The variation with $\vec{Q}$, while consistent with interband scattering across an indirect gap, is similar to that found for $CePd_3$, in the sense that there is not a drastic variation with Q as expected in the Anderson lattice model (section 1.3.b), but only a 20% enhancement at the Brillouin zone boundary.

In addition, in this low-temperature regime, an additional narrow peak occurs in the INS at (33.0 ± 0.5) meV, the same energy as the minimum in the optical conductivity (figure 1.8). In other words, it occurs on the same scale as the hybrization gap. This feature is independent of $\vec{Q}$ over a large fraction of the Brillouin zone, and seems to give evidence of a spatially-localized excitation laying inside the hybridization gap. This excitation cannot arise from intraband Fermi surface scattering due to its Q-independence and its large energy scale. The origin of this excitation remains as an open question.

Chapter 5

Conclusions

The low-temperature magnetic scattering of these intermediate valence compounds, $CePd_3$ and $YbAl_3$, evidence a spin dynamics with the basic behavior expected from the AIM, that is, a broad Kondo-like Lorentzian peak, centered at an energy value around T_K. In addition, the dynamic susceptibility develops a Q-dependence that resembles threshold interband scattering in one sense, namely that the maximum intensity occurs for momentum transfer Q at the zone boundary, connecting regions of large density of states in the two hybridized band scheme. As discussed further below, however, the variation of the intensity lineshape of the magnetic contribution with transfer momentum, is not at all as drastic as the ALM predictions shown in figure 1.9. The 60 meV excitation in $CePd_3$ at low temperatures is similar to the 50 meV one in $YbAl_3$: most intense at zone boundary, but no large shift of spectral shape with Q, as shown in figures 5.1(a) and 3.4 for $CePd_3$ and in figures 5.1(b), and 4.5 for $YbAl_3$.

In the case of $YbAl_3$, an additional magnetic excitation is found at low temperatures. A sharp peak is observed at 33 meV, a value close to the energy of the minimum in the optical conductivity (Fig.1.7 a), with little variation of intensity over (k, l) as shown in

figure 4.7, panels (a) and (b). The lack of Q-dependence suggests a localized excitation; the fact that it occurs at the energy of the minimum in the optical conductivity suggests the excitation is in the middle of the hybridization gap.

The characteristic energies E_0 from the neutron data are in good agreement with the Fermi-liquid relations [13, 51] linking γ and $\chi(T=0)$ with T_K: $\gamma = \pi^2 k_B^2 \langle n^f \rangle / (3T_K)$ and $\chi(0) = \mu^2 \langle n^f \rangle / (3T_K)$ where $\mu^2 = g_J^2 J(J+1) \mu_B^2$. Assuming values $\langle n^f \rangle$ = 0.77 and 0.75 from $CePd_3$ and $YbAl_3$ respectively (Fig. 1.1), obtained from L_{III} absorption measurements [1,3] and using for T_K the values of E_0 (45 ± 8) and (44.0 ± 0.5) meV, and for J and g_J, the values 5/2, 6/7 and 7/2, 8/7, in the order given, we predict γ = (41 ± 7) and (42.9 ± 0.5) mJ $mol^{-1}K^{-2}$ and $\chi(0)$ = (1.2 ± 0.2) and (3.78 ± 0.05) 10^{-3} emu/mol, for $CePd_3$ and $YbAl_3$ respectively, in acceptable agreement with the experimental values as shown in figure 1.1 panels (a, c, d, and f).

At room temperature, which is an appreciable fraction of the Kondo temperature T_K of these compounds, the magnetic scattering for both $CePd_3$ and $YbAl_3$ shows a Q-independent quasi-elastic Lorentzian lineshape characteristic of a local moment, evidencing a purely relaxational spin dynamics with Γ= 26.3 meV for the case of $CePd_3$ and 35.3 meV for the case of $YbAl_3$. This is in agreement with the high-temperature regime predicted by both the Anderson Impurity and Periodic Anderson models, as stated in section 1.3.

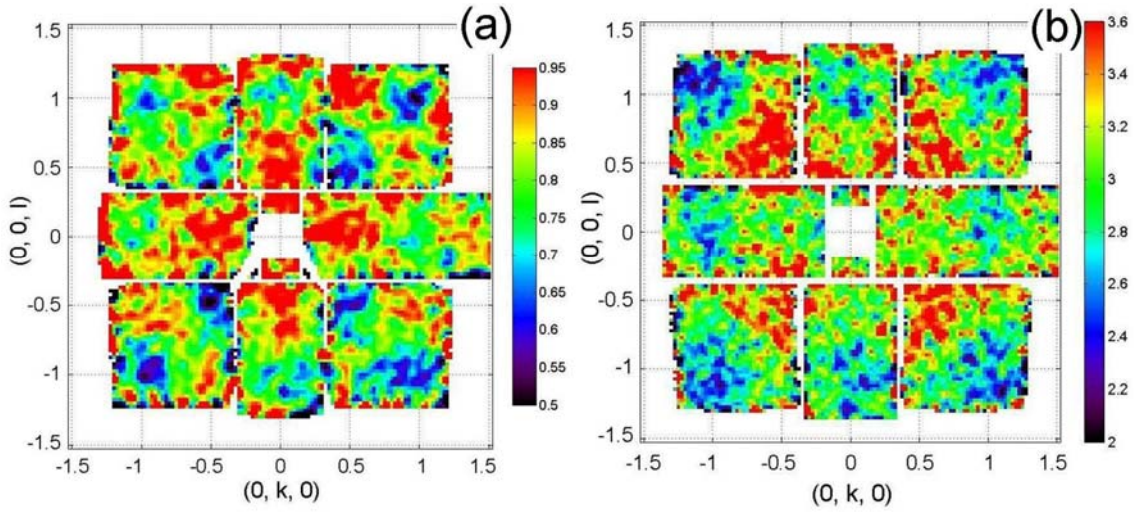

Figure 5.1 Scattering intensity distribution over the (k, l) plane. Intensity maxima are observed at zone boundary points. (a) Intensity of $CePd_3$ at 7 K, integrated over an energy transfer range: 50 < E < 70 meV. (b) Intensity of $YbAl_3$ at 6 K, integrated over an energy transfer range: 45 < E < 55 meV.

With respect to the broad inelastic peaks around 60 meV and 50 meV for $CePd_3$ and $YbAl_3$, respectively, the evolution of their lineshape with temperature is very similar to that predicted by calculations based upon the AIM [52]. At low temperatures, the magnetic contribution to the scattering has the inelastic Lorentzian energy spectrum given by equation (3.1), while at room temperature the magnetic response has the quasielastic Lorentzian spectral lineshape given by equation (3.2). In addition, this quasielastic Lorentzian is Q-independent already at 300 K, denoting the spatially-local character of the magnetic moments in this regime. The scattering evolves between these two lineshapes as temperature increases.

Our results for the magnetic response in $CePd_3$ (and also in $YbAl_3$) are in excellent agreement with calculations from Cox *et al*.[52,53] for the temperature dependence of the

dynamic susceptibility of valence-fluctuating Ce compounds, based on the Anderson impurity model by means of a 1/N expansion. Figure 5.2(a) displays the imaginary part of the dynamic susceptibility $\chi''(E,T)$ scaled by its peak value, versus energy scaled by the peak position of χ''. In the mentioned calculations, the energy scale is T_0, the position of the Kondo resonance peak in the 4f density of states, which is proportional to the Kondo temperature. For $T > T_0$, the expected power spectrum has a quasielastic Lorentzian form (black line). At 300 K, corresponding to $T/T_0 \approx 0.5$ and 0.6 for $CePd_3$ and $YbAl_3$, the fits of our results for the magnetic scattering (red and blue open circles), already overlap this T_0-lineshape. At 6 K and 7 K ($T/T_0 \approx 0.013$ for $CePd_3$ and $YbAl_3$) our results (blue and red closed circles) approach the calculated curve for $T/T_0 = 0.014$ (dashed black line). Experimental results for INS on $CePd_3$ performed by Galera *et al.*[48] at 5 K (black circles) are also included in figure 5.2(a), for comparison reasons. In addition, the temperature evolution of E_{max}, the energy of the peak of $\chi''(E,T)$, for $CePd_3$ and $YbAl_3$ is in reasonable accord with the predictions of Cox *et al.*[52, 53], as illustrated on figure 5.2(b). The values for T_0 for $YbAl_3$ and $CePd_3$ are obtained by matching the low-temperature value of Cox's calculated lineshape with our data.

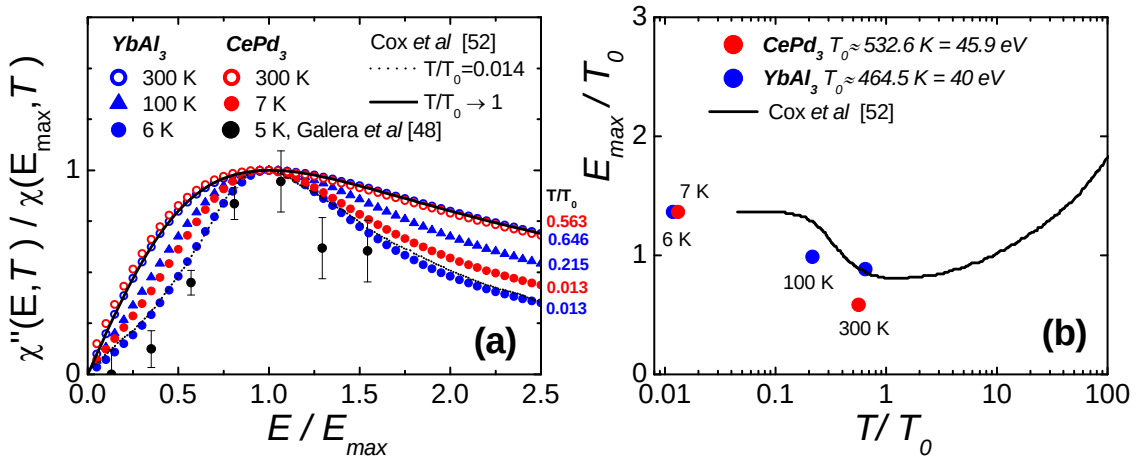

Fig. 5.2.(a) Imaginary component of the dynamic susceptibility scaled by its peak value vs. energy scaled by the peak position of χ" for several temperatures. Fits from measurements on MAPS spectrometer for $YbAl_3$ (blue symbols) and $CePd_3$ (red symbols) and experimental results for $CePd_3$ at 5 K from reference [48] are shown for comparison. AIM calculations at low temperatures T/T_0 =0.014 (dashed line) and the standard quasielastic behavior at $T=T_0$ (black line) are from reference [52]. (b) Temperature evolution of the energy of the peak of the dynamic susceptibility normalized by T_0. Calculation based on the AIM [52] (black line) and values obtained from INS on $CePd_3$ (red symbols) and $YbAl_3$ (blue symbols).

The Anderson impurity model thus works fairly well in describing the spin dynamics response measured by INS on $CePd_3$ and $YbAl_3$ and its temperature dependence (Fig. 5.2). Nevertheless, the observed 15-20% variations of intensity with Q are *much* smaller than those predicted by the Anderson Lattice model, as shown by the calculations of Aligia and Alascio[31] and of Brandow[30] on figure 1.9.

The weak dependence on momentum transfer relative to the Anderson lattice model is also observed in other compounds. A number of valence fluctuation systems, spanning a wide range of characteristic energies, show a similar Kondo-like spectral response: an inelastic Lorentzian with very weak Q-dependence relative to the predictions of the

ALM. This is the case of the compounds $YbInCu_4$[12], and $CeInSn_2$ [10] that show a variation of around 15-20% of the magnetic contribution to the intensity, being stronger at zone boundary, just as in the case of $CePd_3$ and $YbAl_3$.

A particular contradiction found is that the Lorentzian fits seem to indicate no gap in the scattering, a feature which, based on figure 1.9, should be more noticeable for the Q = 0 transitions. The magnetic contribution to the scattering $CePd_3$, measured on HB3 TAS over a constant-Q scan at zone center (Fig. 3.9(b)) does not seem to show a gap, at least above the phonon cut off. One explanation for not seeing the gap is a possible overlap of intra and inter-band transitions over the energy transfer range.

There are several possible reasons for the significant failure of the applicability of the Anderson lattice model to the spin dynamics of the IV compounds. One is that the band structure is more complex than just two hybridized bands. There may be significant regions of momentum transfer Q where the 4f bands above and below the Fermi level are very flat, leading to the same excitation energy being observed over a broad range of Q. However, these bands remain to be calculated. Furthermore, there are four examples where measurements on single crystals show this weak Q-dependence and this Kondo impurity-like behavior: $YbAl_3$, $CePd_3$, and $YbInCu_4$ and $CeInSn_2$, and it is improbable that they all have the same band structure.

Among the Anderson Lattice calculations, the slave boson approximation is a mean field (MF) calculation, Brandow[30] applies a variational version, and the calculation of Aligia and Alascio[31] is a version of effective MF. These do not necessarily get the excitations correctly. As is true for uncorrelated band theory, we might expect the mean

field treatment to be correct close to the Fermi energy but to poorly estimate excitation energies away from the Fermi level.

In addition, there is a finite lifetime effect that leads to the broadening of the otherwise sharp features. Excitations taking place around the Fermi level, with almost zero energy differences, have infinite lifetime. In contrast, in the case of interband excitations, away from Fermi level, the lifetime is certainly finite, and this could be the reason for a smearing of the otherwise sharp threshold for the interband excitations.

Other possible reasons include phonon assisted transitions; these destroy the unique relation between energy transfer E and momentum transfer Q. Finally, there may be significant overlap of the intraband Fermi Liquid excitations with the interband transitions. We are uncertain about the energy scales of the former, which may extend above 10 meV.

The similarity to AIM predictions suggests that the excitations are much like localized Kondo fluctuations. The 33 meV excitation in $YbAl_3$ is a clear warning that there can be highly local excitations in the renormalized band ground state. In his calculation, Brandow[30] included a localized "moment-unbinding" excitation, not derived from the Anderson Periodic Hamiltonian, but in an *ad hoc* manner. It involves an onsite valence fluctuation from the hybridized state (screened local moment) into the non-hybridized $4f^1$ (magnetic) state. In this manner, a two-peak structure of the susceptibility and specific heat should be observed, similar to the low temperature anomalies reported by Cornelius, *et al*. [1]. Whether or not this approach is correct, it appears that the excitations in the Anderson lattice may be much more like those of an Anderson impurity than has been previously recognized.

Bibliography

[1] A. L. Cornelius, J. M. Lawrence, T. Ebihara, P. S. Riseborough, C. H. Booth, M. F. Hundley, P. G. Pagliuso, J. L. Sarrao, J. D. Thompson, M. H. Jung, A. H. Lacerda, and G. H. Kwei, Phys. Rev. Lett. **88**, 117201 (2002).

[2] E.D. Bauer, unpublished.

[3] C. H. Booth, unpublished.

[4] V. R. Fanelli, unpublished.

[5] C. M. Varma, Rev. Mod. Phys. **48**, 219 (1976).

[6] J. Lawrence, Mod. Phys. Lett. B **22**, 1273 (2008).

[7] H. Okamura, T. Michizawa, T. Namba, and T. Ebihara, J. Phys. Soc. Jpn. **73**, 2045 (2004).

[8] T. Ebihara, Y. Inada, M. Murakawa, S. Uji, C. Terakura, T. Terashima, E. Shamamoto, Y. Haga, T.Ōnuki and H. Harima, J. Phys. Soc. Jpn. **69**, 895 (2000).

[9] C. H. Booth, private communication.

[10] A. P. Murani, A. Severing, M. Enderle, P. Steffens and D. Richard, Phys. Rev. Lett. **101**, 206405 (2008).

[11] A. D. Christianson, V. R. Fanelli, J. M. Lawrence, E. A. Goremychkin, R. Osborn, E. D. Bauer, J. L. Sarrao, J. D. Thompson, C. D. Frost, and J. L. Zarestky, Phys. Rev. Lett. **96**, 117206 (2006).

[12] J. M. Lawrence, S. M. Shapiro, J. L. Sarrao, and Z. Fisk, Phys. Rev. B **55**, 14467 (1997).

[13] A. P. Murani, A. Severing, and W. G. Marshall, Phys. Rev. B **53**, 2641 (1996).

[14] S. M. Shapiro, C. Stassis, and G. Aeppli, Phys. Rev. Lett. **62**, 94 (1989).

[15] E. Holland-Moritz and G. H. Lander, in Handbook on the Physics and Chemistry of the rare Earths, vol. 19, eds. K. A. Gschneidner Jr. et al. (Elsevier Science B.V., Amsterdam, 1994), p.1.

[16] J. M. Lawrence, P. S. Riseborough, C. H. Booth, J. L. Sarrao, J. D. Thompson and R. Osborn, Phys. Rev. B **63**, 054427 (2001).

[17] A. P. Murani, R. Raphel, Z. A. Bowden, and R. S. Eccleston, Phys. Rev. B **53**, 8188 (1996).

[18] J. M. Lawrence, V. R. Fanelli, E. A. Goremychkin, R. Osborn, E. D. Bauer, K. J. McClellan, A. D. Christianson, Physica B, **403**, 783 (2008).

[19] A. C. Hewson, *The Kondo Problem to Heavy Fermions* (Cambridge University Press, Cambridge, UK, 1993).

[20] H. Okamura, T. Watanabe, M. Matsunami, T. Nishihara, N. Tsujii, T. Ebihara, H. Sugawara, H. Sato, Y. Onuki, Y. Isikawa, T. Takabatake, and T. Nanba, J. Phy. Soc. Jpn. **76**, 023703 (2007).

[21] T. Ebihara, E. D. Bauer, A.L. Cornelius, J.M. Lawrence, N. Harrison, J.D. Thompson, J. L. Sarrao, M. F. Hundley, and S. Uji, Phys. Rev. Lett. **90**, 166404 (2003).

[22] D. M. Newns, A. C. Hewson, J. Phys. F **10**, 2429 (1980).

[23] P. W. Anderson, Phys. Rev. **124**, 41 (1961).

[24] J. R. Schrieffer and P. A. Wolff, Phys. Rev. **149**, 491 (1966).

[25] T.M. Rice and K. Ueda, Phys. Rev. Lett. **55**, 995 (1985).

[26] A.J. Millis and P.A. Lee, Phys. Rev. B **35**, 3394 (1987).

[27] A. Auerbach and K. Levin, Phys. Rev. Lett. **57**, 877 (1986).

[28] P. Coleman, Phys. Rev. B **35**, 5072 (1987).

[29] S. Burdin, A. Georges, and D.R. Grempel, Phys. Rev. Lett. **85**, 1048 (2000).

[30] B. H. Brandow, Phys. Rev.B **37**, 250 (1988).

[31] A.A. Aligia, and B. Alascio, J. Mag. Mag. Mat. **46**, 321 (1985).

[32] X. Feng, M. Qiu, J.Mu, W. Gao, and A. Shi, Phys. Rev. B, 63, 085101 (2001).

[33] A.N. Tahvildar-Zadeh, M. Jarrell, and J.K. Freericks, Phys. Rev. B **55**, R3332 (1997).

[34] P. Fazekas, "*Lectures Notes on Electron Correlation and Magnetism*", Series in Modern Condensed Matter Physics, Vol. 5, (World Scientific Publishing, Singapore, 2003).

[35] A. Hübsch and K.W. Becker, Phys. Rew. B, **71**, 155116 (2005).

[36] A. J. Fedro, and S. K. Sinha, Valence Fluctuations in Solids, eds. L. M. Falicov, W. Hanke and M. B. Maple, 135 (North-Holland, Amsterdam, 1981).

[37] P. C. Canfield, Z. Fisk, Phil. Mag B **65**:6, 1117 (1992).

[38] J. T. G. Shirane, S.M.Shapiro, J.M.Tranquada, *Neutron Scattering with a Triple-Axis Spectrometer*. Cambridge, Cambridge University Press, 2002.

[39] W. Marshall, and R.D. Lowde, Rep. Prog. Phys. **31**, 705 (1968).

[40] R. Currat, *Three Axis Inelastic Neutrons Scattering*, *Neutron and X-ray Spectroscopy*, p. 383, F. Hippert et al. (eds.), Springer, Netherlands, 2006.

[41] A.J. Freeman, and J.P. Desclaux, J. Magn. Magn. Mater.. 12, 11, (1979).

[42] E. Holland-Moritz, D. Wohlleben, and M. Loewenhaupt, Phys. Rev. B **25**, 7482 (1982).

[43] A. P. Murani, R. Raphel, Z. A. Bowden, and R. S. Eccleston, Phys. Rev. B **53**, 8188 (1996).

[44] R. Osborn, E. A. Goremychkin, I. L. Sashin, A. P. Murani, J.Appl.Phys **85**, 5344 (1999).

[45] H. Rauch, and W. Waschkowski, "*Neutron Scattering Lenghts*" in Neutron Data Booklet, ch. 1.1, A.J. Dianoux,and G. Lander (Old City Publishing, Philadelphia, 2003).

[46] R. M. Galera, A. P. Murani, J. Pierre, and K.R.A. Ziebeck, J. Magn. Magn. Mat. **63-64**, 594 (1987).

[47] C. Stassis, C. K. Loong, J. Zarestky, O. D. McMasters, R. M. Moon, and J. R. Thompson, J. Appl. Phys. **53**, 7890 (1982).

[48] R. M. Galera, D. Givord, A. P. Murani, J. Pierre, C. Vettier and K.R.A. Ziebeck, J. Magn. Magn. Mat. **47-48**, 139 (1985).

[49] C. K. Loong, J. Zarestky, C. Stassis, O. D. McMasters, and R.M. Nicklow, Phys. Rev. B **38**, 7365, (1988).

[50] A. P. Murani, Phys. Rev. B **50**, 9882 (1994).

[51] N. E. Bickers, Rev. Mod. Phys. **59**, 845 (1987).

[52] D. L. Cox, N. E. Bickers and J. W. Wilkins, J. Magn. Magn. Mat. **54-57**, 333 (1986).

[53] D. L. Cox, N. E. Bickers and J. W. Wilkins, J. Appl. Phys.**57**, 1 (1985).